Alma Mater Studiorum – Università di Bologna

DOTTORATO DI RICERCA IN

CHIMICA

Ciclo XXX

Settore Concorsuale di afferenza: CHIM/03

Settore Scientifico disciplinare: 03/B1

MAPPING pH IN SELF-ASSEMBLED INORGANIC STRUCTURES BY FLUORESCENCE MICROSCOPY

Presentata da:

Jeannette Manzi

Coordinatore Dottorato: **Relatore:**

Prof. Aldo Roda **Prof. Marco Montalti**

Esame finale anno 2018

Table of contents

1 Introduction

1.1 Biomorphs

The variety and structural complexity of forms displayed by mineralized inorganic matter in nature have always been intriguing for a lot of scientists from every field. Biominerals often exhibit extraordinary properties that exceed the performance of their manmade counterparts: this fact has led to attempts to mimic them as close as possible *in vitro*, with the aim to generate materials with advanced features for distinct applications. “Biomimetic” materials chemistry and bioinorganic morphosynthesis have received much attention over the past decades, and many studies were performed in order to create novel materials with special morphologies and structures.[1],[2],[3],[4],[5]

In this field, an important role is played by silica because of its abundance in natural settings both as a mineral and as in the dissolved state. Moreover, with the nowadays importance of crystal growth in gels,[6] there has been increasing interest in the use of silica matrices as media for the preparation of single crystals. The most surprising discovery in this context was that alkaline earth metal carbonates can choose peculiar shapes when crystallized from such silica-rich environments,[7],[8],[9],[10] very close to nature ones. For this reason, crystals formed with these biomimetic architectures were named “silica biomorphs”. This specific kind of precipitates, in fact, are characterized by similarity to biogenic structures in term of texture and composition of the precipitates, the hierarchical ordering of the building units and the intergrowth of the components (silica and carbonate) over multiple length scales. However, even if their shapes share many of the characteristics generally associated with biomineral materials, their assembly and organization during the growth proceed through self-assembly and self-organization processes driven by simple inorganic chemical interactions, in which no complex biomolecule or organic compound are present.[11] These facts led biomorphs to be used as a proof that morphology and/or chemical composition, by themselves, are not a sufficient basis for claims of detection of ancient primitive life.[12],[13]

The circumstances reported above make silica biomorphs an exceptional model for advanced inorganic-inorganic hybrid materials and for developing bottom-up strategies to design functional materials through concerted self-assembly, where silica takes over the structure-directing role usually performed by organic species in both biological and biomimetic mineralization.

Although the first record of “life-like” shapes in inorganic silica-carbonate environments dates back to the work of Herrera in 1912,[7] silica biomorphs in the narrow sense were actually discovered by García-Ruiz et al. in the early 1980s,[8],[9],[10] and from this point on a lot of work has been made.

About biomorphs formation, initially it was thought to require a silica gel body at a pH of about 10-10.5, in which carbonate crystallization was induced either by counterdiffusion of the reactants (usually barium chloride and sodium carbonate) in a U-shaped cassette or by covering a gel containing a certain amount of predissolved carbon dioxide with a concentrated solution of $BaCl_2$, followed by unidirectional diffusion.[14] In both cases, gradual precipitation produced biomorphic shapes throughout the gel matrix, whose detailed morphology, size, and number depend on the location into the gel-solution relative to the distance from the interface. It was also found that identical shapes could be obtained also by directly mixing metal salts with dilute silica sol and exposing the mix to the atmosphere in order to absorb CO_2, which is essential for the biomorphs formation.[13],[15],[16],[17],[18]

Recently, it was found that there is a range of suitable pH values in which biomorphs can grow: in gels it is pH = 9.3-9.8[11] and in solution pH = 10.2-11.1.[19] Within this range, the most frequently morphologies of silica biomorphs can be divided into three distinct types, namely helicoidal filaments, thicker worm-like braids, and extended flat sheets (a, b and c of figure 1.1, respectively).

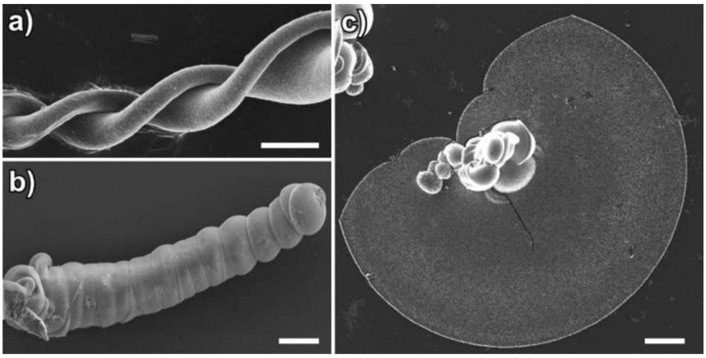

Figure 1.1 Principal morphologies obtained from a typical synthesis of silica biomorphs. Scale bars: 20 µm.[20]

Other experimental variables were found to affect the resulting structures such as temperature[17],[21] and species concentrations.[22],[23]
Further studies shew that organic additives, such as ethanol as co-solvent,[18] or cationic surfactants and polymers[24], amino acids[22] and proteins involved in biomineralization.[17] have an influence on the final structure of the aggregates, even if the reason why these general effects happen remain largely obscure. However, it is evident that additives that easily interact with silica in solution tune biomorphs morphology.[24]

From images of fractured aggregates, it could be affirmed that generally biomorphs are composed of carbonate and silica, with a textured inner core surrounded by a silica outer skin with a different consistency:

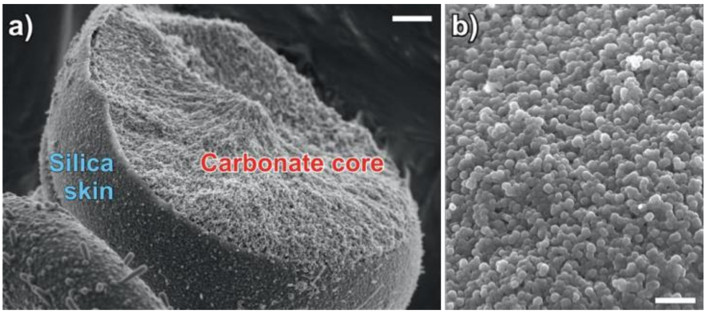

Figure 1.2 (a) FESEM image of a fractured worm-like aggregate, revealing the presence of an outer silica skin sheathing a textured inner core. Scale bar: 2 µm. (b) Zoom onto the surface of the external membrane, showing densely packed siliceous nanospheres. Scale bar: 1 µm.[20]

X-ray diffraction confirms the presence of orthorhombic witherite in the core part,[12],[17],[25] while the outer layer is made of almost pure amorphous silica, as shown by EDX spectroscopy and the lack of reflections for crystalline silicates in the XRD patterns. [11],[26],[27],[28],[29] Moreover, silica envelope of the crystal assembly is composed of agglomerated spherical nanoparticles (figure 1.2 b), typically between 50 and 150 nm in diameter, which form a colloidal membrane.[12],[16],[27] Zooming at the nanoscale, it can be seen that silica biomorphs are polycrystalline aggregates, more in detail, a multitude of elongated crystallites quite uniform in size and shape (figure 1.3).

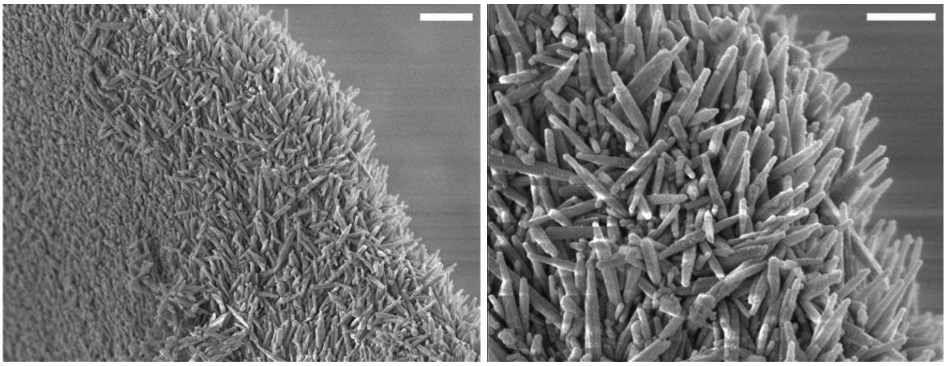

Figure 1.3 Close-up views of the edge of a sheet-like biomorph. Scale bars: 1 μm (left), 500 nm (right).[20]

TEM studies[27] on individual crystallites have shown that the building units are witherite nanorods exhibiting a pseudohexagonal columnar habit (figure 1.1.4 a-c), exposing prismatic {110} side faces that are closed by pinacoidal {001} planes or tapered by {102} and {021} bipyramidal faces. This is common for aragonite-type carbonates and results from cyclic twinning on the {110} planes.[30] Typical dimensions of the nanorods constituting biomorphs range from 200 to 400 nm in length and from 5 to 100 nm (usually around 50 nm) in width.[13],[16],[17],[24],[27],[31] Each nanocrystal appears to contain a quite small fraction of silica (up to 5%), determined by elemental analyses of the particles (figure 1.4 d).

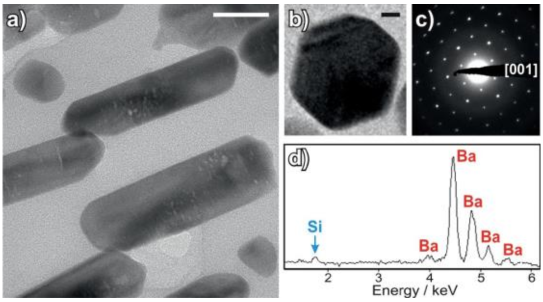

Figure 1.4 (a) TEM micrograph of the silica biomorphs nanocrystals. Scale bar: 50 nm. (b) Cross-section of a nanorod. Scale bar: 10 nm. (c) Electron diffraction pattern of the [001] zone axis of the witherite lattice. (d) EDX spectrum of a nanorod. Panels (a) and (d) reproduced with alterations and with permission from ref. [20],[27]

The orientation of the nanorods follows a distinct long-range order throughout the aggregates:[12],[13],[16] adjacent rods are arranged almost parallel to one another with respect to their crystallographic *c* axis (which is the long axis of the rods), but they maintain a slight mutual misalignment (figure 1.5 d). This incremental twist (or tilt) between individual crystallites is kept approximately constant, that makes the building units describe an oriented field with a gradually varying vector, as it is proved by light crossed polarizers microscope[16] and by X-ray diffraction:

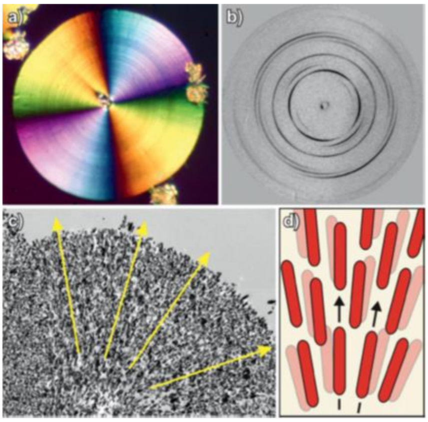

Figure 1.5 (a) Polarized optical micrograph of a circular sheet. (b) Microfocus X-ray diffraction pattern collected from a distinct part of a sheet. (c) TEM image of a sample prepared by thin-sectioning of as-grown biomorphs. Arrows indicate the preferred orientation of the crystallites. (d) Sketch depicting the typical local arrangement of building blocks in silica biomorphs.[20]

1.1.1 Calcium and barium biomorphs in gel

Witherite biomorphs grow indistinctively in silica solutions and gels. The sol-gel route leads to the formation of porous silica gels, but their pore size cannot be accurately controlled. However, it is possible to get ordered mesoporous silica, as it was shown, in the presence of surfactants such as cethyltrimethylammonium chloride.[32]

Biomorphs that grow in silica gels can be made by both barium and calcium solution. Calcium carbonate crystals are produced by the counterdiffusion method in an alkaline silica gel.[11],[33],[34] The experiments are usually performed in glass cassettes made by two flat glasses separated by a rubber ribbon.
In order to create this type of crystals, the preparation of a stable and homogeneous silica hydrogel is crucial, because outcome of silica-controlled carbonate crystallization in both gels and solutions depend on it. Silica gels are most obtained by lowering the pH of a sol, which will induce enhanced protonation of siliceous species

$$\equiv\text{Si-O}^- + \text{H+} \rightarrow \text{H+} \rightarrow \equiv\text{Si-OH}$$

and trigger condensation reactions

$$\equiv\text{Si-OH} + \text{HO-Si}\equiv \rightarrow \equiv\text{Si-O-Si}\equiv + \text{H}_2\text{O}.$$ [35]

This acidification increases the $[SiO_2]/[NaOH]$ ratio making it less soluble in the solution. As a result, the condensation reaction induces the polymerization and finally the gelling of the silica solution.[36] After more or less five days the gelling process is finished, a barium or calcium chloride solution of a certain concentration is poured on top.

If $BaCl_2$ is considered, its cations diffuse through the gel, and the precipitation of barium carbonate crystals and carbonate ions, dissolved from atmospheric carbon dioxide in the gel and in the solution, occurs. The diffusion of the barium solution and the following precipitation of carbonate contribute to create a time-dependent gradient of pH along the diffusion direction in the gel that will affect the growth of silica biomorphs. By measuring the gradient along the gel at different times, the morphologies of biomorphs in the gel and their evolution could be correlated with pH:[11]

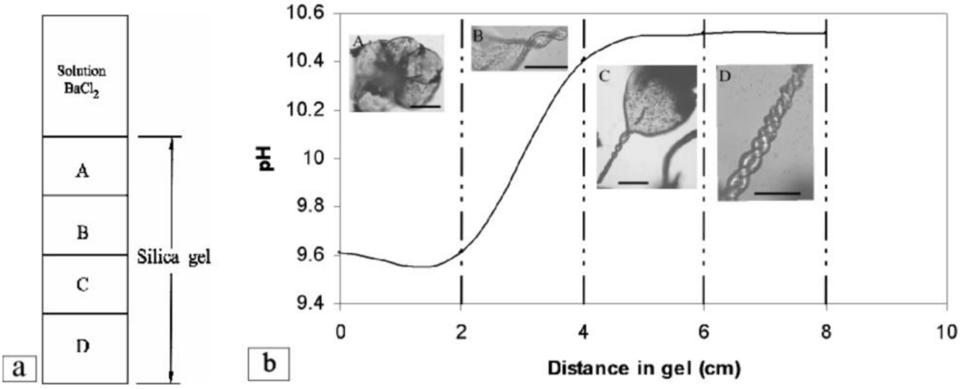

Figure 1.6 (a) Representation of the reaction cell in which the gel is divided into four different sections. (b) Diagram of the change of pH and observed morphology with distance from the gel interface.[17]

However, there are some problems in measuring the pH of silica gels. First of all, common glass electrodes cannot be used since most of them rely on the formation of a very thin wetted silica gel around the glass bulb for ion transport when they are brought into contact with the solution. Because of this, alkaline silica gels interact strongly with the glass bulbs sensibly decreasing their reliability after a few measurements. Secondly, the pH of the interstitial solution of the gel rises during the gelling process in an amount that cannot be easily predicted, as it depends on the solubility equilibrium conditions of the gel. Finally, measuring pH in a gel is an invasive way that lead to deteriorate the gel because the gel needs to be mechanically manipulated to put it in good contact with the probe.

For these reasons, pH of the different gels was measured with commercial pH microprobes and pH-meters. These microprobes use solid-state technology for the sensor and are unaffected by the chemistry of silica, being therefore very suitable to measure pH in silica gels. The collected results are shown below:

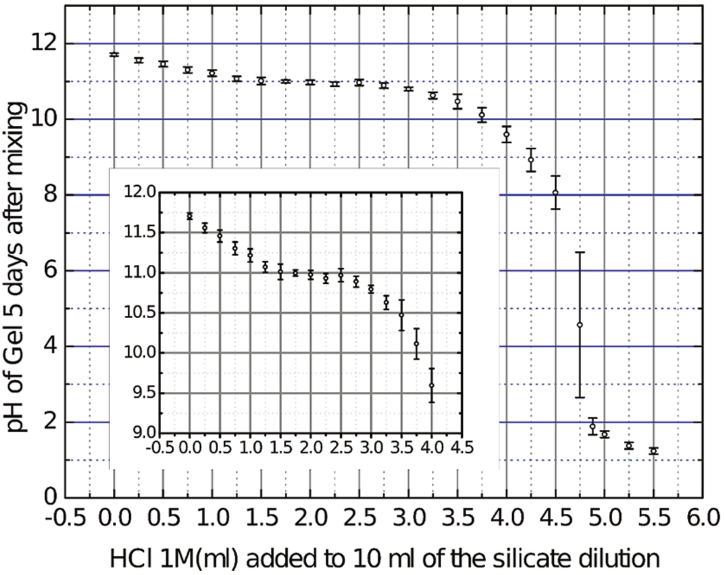

HCl	N
0	24
0.25	28
0.5	36
0.75	28
1	36
1.25	28
1.5	36
1.75	27
2	40
2.25	36
2.5	72
2.75	68
3	80
3.25	76
3.5	80
3.75	80
4	84
4.25	80
4.5	76
4.75	72
4.88	52
5	56
5.25	20
5.5	24

Figure 1.7 pH of gels obtained by acidification of sodium metasilicate solution with 1M HCl, after 5 days.[11]

In order to obtain these values, the cassette was opened and the upper solution was poured away taking care that it did not cover nor it was spilled over the gel. The gel was divided into slices and each slice was pushed inside a small eppendorf tube where the pH microprobe was inserted to measure the pH, associating then the obtained values to the coordinates of the distance from the interface.

From figure 1.8 it can be seen that the initial pH is 10.4 and that after the addition of the $BaCl_2$ solution there is a variation of pH gradient, rising to the initial pH at the end of the cell. The influence of the diffusion of the barium solution in the pH gradient is clearly seen in the differences between the curves at 7 h, 1 days, and 2 days, from which pH at a fixed distance from the interface decreases from the initial value of 10.4. For sure, the acidification, due to carbonate precipitation, contributes to this decrease in these areas. The curve at 7 h misbehaves at large distances from the interface due to some experimental problems. However, the relevant measurements of these cells are only those corresponding to less than 1 cm where aggregates are present at this early stage.

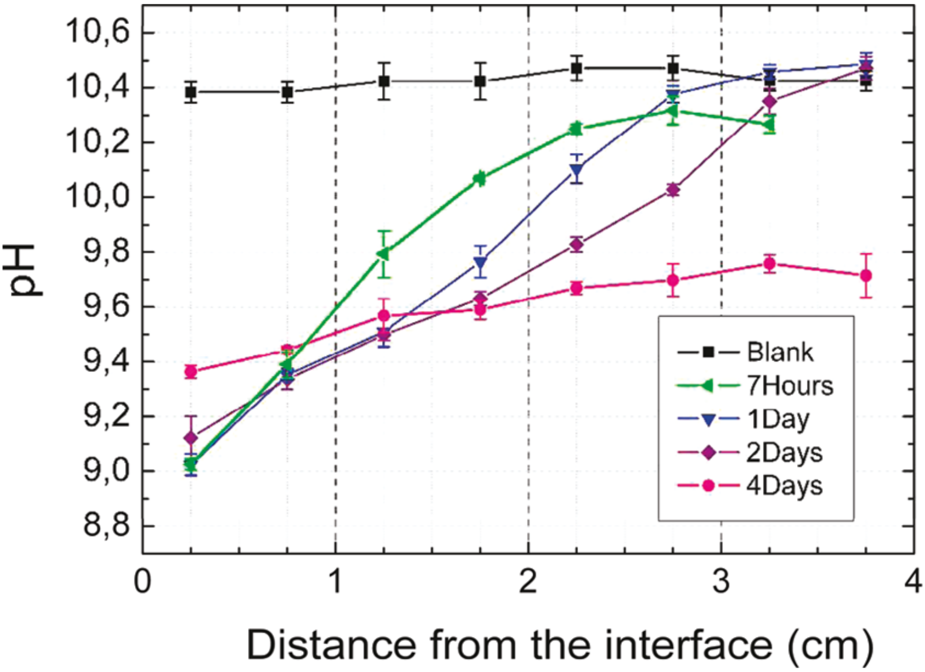

Figure 1.8 Time development of the pH values versus distance to the interface.[11]

The growth process of gel-grown aggregates appears from optical microscopic observations to proceed in two stages, as it can be seen in figure 1.9. The first precipitates, that form closest to the site of salt introduction and consequently grow at the lower pH range (8.5 < pH < 9.5), are often fractal-like dendritic forms with an approximately radial symmetry showing continuous non-crystallographic branching whose diameter is at the scale of mm. The resulting cauliflower-like morphologies are made of a radiating array of barium carbonate crystals, which successively branch at small, non-crystallographic angles, forming a 3-D space-filling structure. The building blocks of these structures are micron-size crystals.[12] In particular, many aggregates near the interface appear at very early stages, showing a globular shape and laminae on some of them, that characterize growth under the second stage of the formation mechanism.[11],[12],[17] On the contrary, aggregates far from the interface, and especially at the end of the cells, are larger and show the characteristic curvilinear morphologies like large sheets and helicoids. In general, they display more developed and differentiated morphologies with increasing growth time.

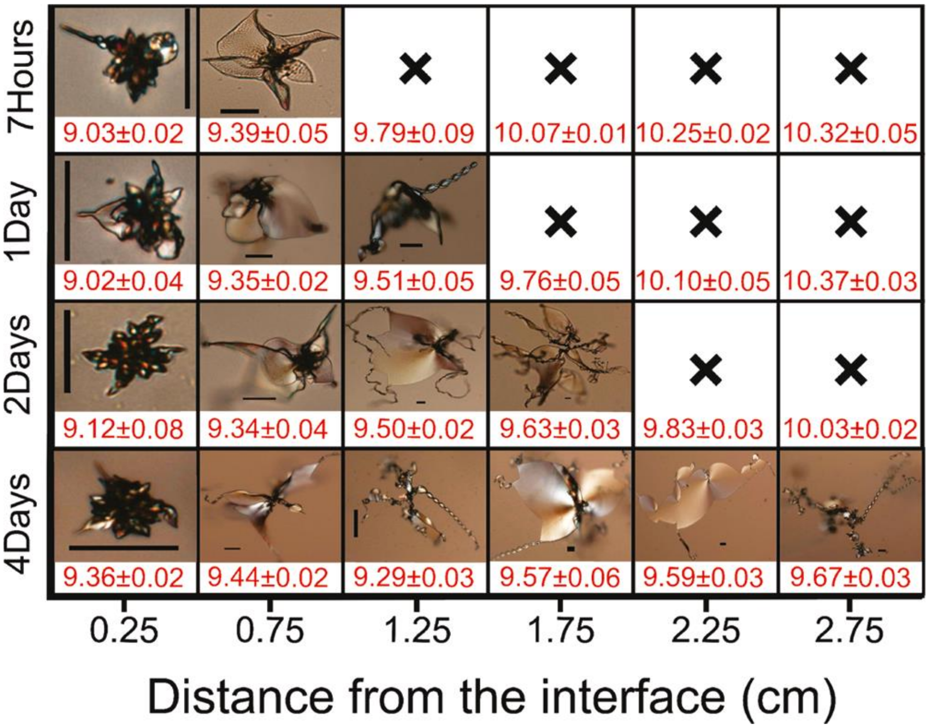

Figure 1.9 Spatial and temporal images of representative aggregates as a function of pH at different distance from the interface. Scale bar: 50 μm.[11]

It can be concluded that the spatial and temporal development of the pattern of precipitates is related to the diffusion of the barium ions through the gel. However, the gradient of pH that is formed inside the gel is not only influenced by the diffusion of the slightly acid barium solution, but it is also affected by the precipitation of barium carbonate. Therefore, pH inside the silica gel is a parameter that cannot be easily predicted and it needs to be measured directly in real time.[11]

If biomorphs grown from calcium solution are now considered, it has to be said that calcite, the hexagonal phase of calcium carbonate, is be reluctant to undergo biomorphic behavior, because it preserves its crystallographic symmetry.[37],[38],[39] However, biomorphs can appear.

The same cassette used to create barium gel-grown biomorphs is used for this type of growth. Diffusion of the calcium chloride into the carbonate-rich alkaline gel starts as soon as the solution is poured on top of the gel, provoking a chemical gradient that evolves in time and space. This chemical gradient produces temporal and spatial variation of Ca/CO_3 ratios and its supersaturation values, hence yielding to calcium carbonate precipitation with different crystalline phases and morphologies at corresponding locations along the crystallization cell:

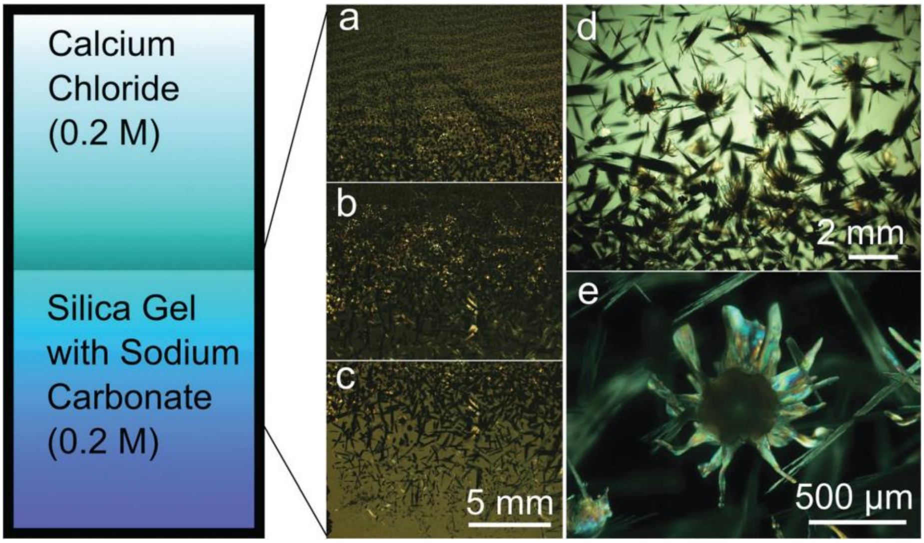

Figure 1.10 Schematic crystallization cassette (left) and the optical micrographs of the various crystal formation mechanisms after three weeks of crystallization (right). (a) Liesegang patterns of rhombohedral calcite; (b) concomitant crystallization of flower-like silica aragonite biomorphs and elongated calcite; (c) elongated calcite; (d and e) close-up view of flower-like silica aragonite biomorphs and elongated calcite.[40]

The critical supersaturation was reached near the gel-solution interface and the first precipitate, named rhombohedral calcite (figures 1.10 a and 1.11 a), formed inside the gel. The precipitation front advanced across the gel with time, and the size of the rhombohedra increases as a function of time and distance from the interface (figures 1.10 b and c). This precipitation occurs in most cases as precipitation bands that follow the Jablczinsky law characteristic of Liesegang patterns (figure 1.10 a).[41],[42]

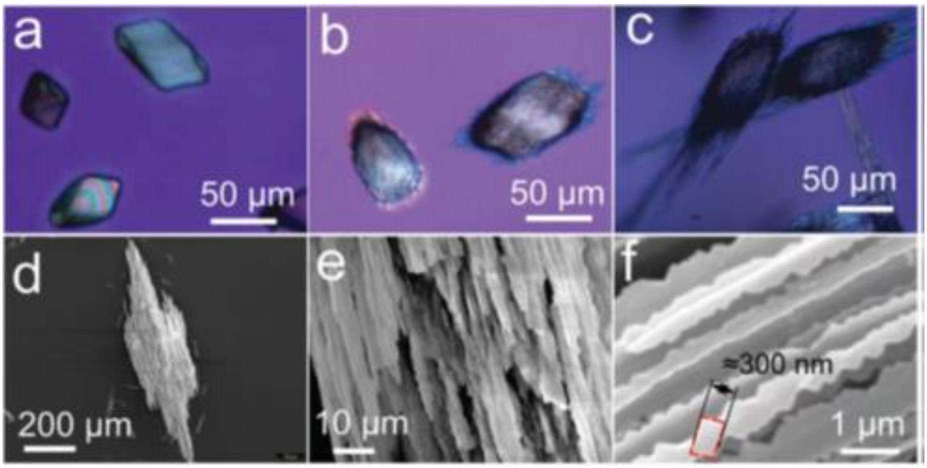

Figure 1.11 (a) Optical micrograph of rhombohedra calcite crystallized near the gel-liquid interface; (b and c) optical micrograph of elongated fibrous calcite crystallized at 5 days and 10 days; (d) FESEM image of a full view of elongated fibrous calcite; (e and f) close-up view of elongated fibrous calcite.[40]

During the second week of crystallization, the precipitation front appears at one centimeter from the gel-solution interface, and the elongated calcite crystals developed into fibrous dendritic aggregates (figures 1.11 b and c).[37],[38] Precipitates with complex biomorphic shapes appeared between elongated fibrous calcite (figures 1.11 d, e and f) between 1 cm and 2.5 cm from the gel-sol interface, while the precipitation zone of elongated fibrous calcite advanced further in the gel during the third week from calcium injection (figures 1.10 d and e). These biomorphic shape crystals were identified as aragonite. and it was also discovered that temperature affected their morphology: they are smaller dumbbell-shaped cores at low temperatures, whereas longer and larger petal-like curling sheets with more twisted and longer structures at higher ones.

In figure 1.12, that shows some frames of a movie of growing crystals inside the gel, it can be observed that there is a concomitant growth of the two different mineral phases: calcite and aragonite. It can be said that there is a strong difference in morphology between the two polymorphic calcium carbonate phases, and that there is the simultaneous growth of both polymorphs under the same chemical conditions. It is obviously a case of polymorphism, where pH can not explain how these crystals can choose which kind of polymorph can become.

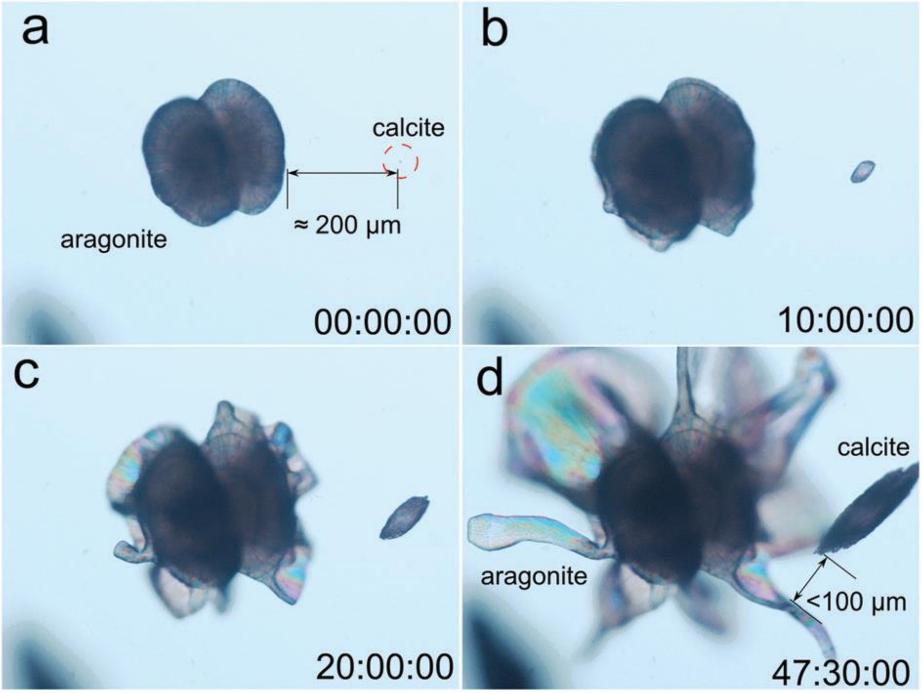

Figure 1.12 Selected frames of the image sequence from the time-lapse video of the growth of flower-like silica aragonite biomorphs and elongated calcite.[40]

Initially there seems to be the nucleation of aragonite crystallites that decreases the pH and induces the precipitation of silicate species that poison the crystal surfaces and prevent further growth. The increase of the pH due to silica precipitation provokes the nucleation of aragonite, which in turn provokes the fall in pH, that again leads to precipitation of silica that inhibits their growth, and so on. In this way, the fractal growth goes toward fibrillation, namely the complete inhibition of the growth of the aragonite dendrite and subsequent nucleation of new and independent aragonite crystallites that grow only to hundreds of nanometers in size because of silica poisoning.

The difference between the two polymorphs is not related to their crystal structure but to the texture at the nanoscale, since biomorphic aragonite particles consist of nanorods while fibrous elongated calcite particles consist of rhombohedral crystallites. The calcite dentate fibre-like subunits grow continuously remaining consistent with the growth vectors. On the other hand, aragonite nanorods, that form due to the cessation of growth at the nano scale, are isolated, which allows gradual change of the growth vectors, leading to curling phenomenon.[40]

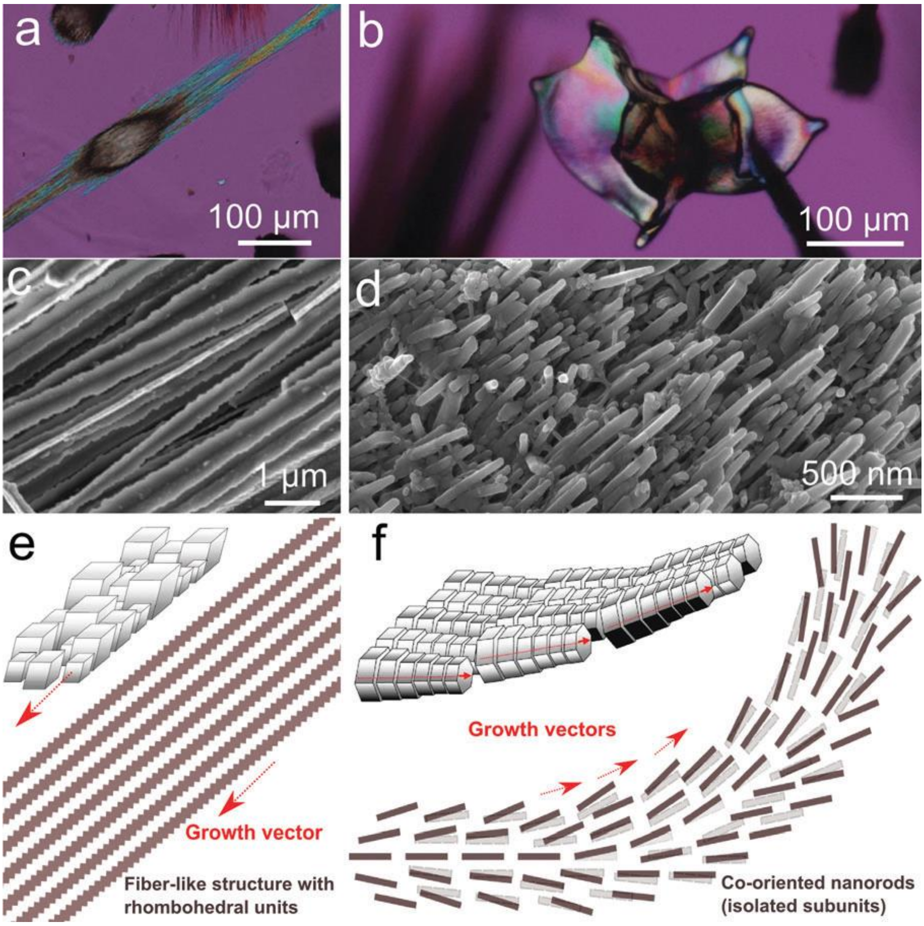

Figure 1.13 (a) Non-biomorphic calcite and (b) biomorphic aragonite as seen by optical microscopy with crossed polarisers; (c) FESEM pictures of co-oriented fibres of non-biomorphic calcite and (d) nanorods forming biomorphic aragonite; (e) scheme of the textural model for non-biomorphic calcite and (f) biomorphic aragonite. Fibrillation of biomorphic aragonite allows bending and curling of the composite material and then complex morphogenesis.[40]

1.2 Silica gardens

Silica gardens are self-assembled hollow structures resulting from a precipitation reaction involving a metallic salt (all metal salts can serve as seeds except for group 1A compounds)[43] and an aqueous alkaline solution, namely silicate. There has been interest in the search of the origin of life since silica gardens adopt biomimetic morphologies,[44],[45],[46] and thus they may have driven the origin of metabolism on the early Earth. They are interesting structures also for other branches of science, such as chemistry, physics, nonlinear dynamics, and materials science. They exhibit rich chemical, magnetic, and electrical properties due to pH and electrochemical gradients across their walls during their growth process.[47] Moreover, they share common properties with nanoscale tubes in cement,[48] corrosion filaments,[49] larger-scale brinicles,[50] chemical motors such as fuel cells, and as Brønsted catalysts[51],[52] (also in microfluidics), because they are similar to compartmentalized and layered self-organized materials.[43],[53],[54],[55],[56],[57],[58],[59] Silica gardens are also intriguing structures because of their supposed role in prebiotic chemistry: under-sea vents contain, in fact, magnetite, brucite ($Mg(OH)_2$) and serpentine, which is a hydroxylated magnesium-iron silicate, that lead to a system with a pH contrast inverse to the classical acid interior/alkaline exterior garden.[60],[61] The wall structures are exposed to tremendous concentration, pH and temperature gradients. These gradients in conjunction with catalytic surfaces seem to sustain complex chemical reactions such as the ones that happen inside a chemical garden.[53],[62],[63] Different ways to produce these hollow tubes have been studied: in the classic method, a solid salt particle is put inside a sodium silicate solution in a vertical box.[64] However, there is also an approach that consists of injecting the metal salt solution inside that box full of silicate with a constant flow rate[65],[66] or at constant driving pressures, [56],[57],[58],[67],[68],[69],[70],[71],[72] where the advantages are that only single tubes are formed, the overall reproducibility is improved, and the concentration, viscosity, and density of the two reactant solutions are initially known.[73] More recently also the spatially confined system has been investigated, where the metal salt solution is injected between a quasi-2D cell, similar to an Hele-Shaw one, leading to a horizontal growth of the gardens.[74]

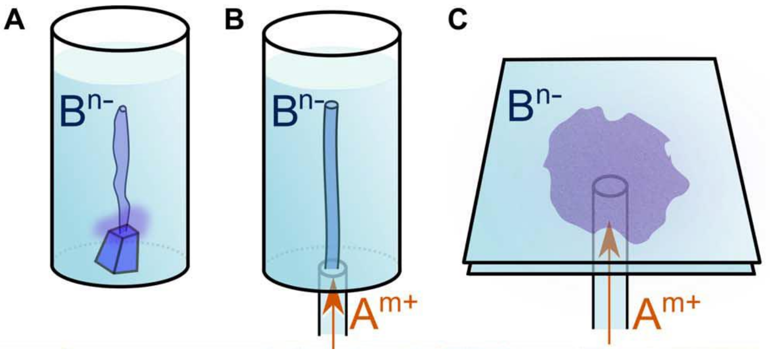

Figure 1.14 Schematics of silica garden experiments using (A) a seed crystal, (B) solution injection, and (C) a spatially confined system.[73]

In the case of seed crystals, the growth starts with the dissolution of metal salt which leads to the formation of a colloidal metal (hydr)oxide membrane around the dissolving seed particle. Then, the dissolution of this membrane is caused by the osmotically driven flow of water that pulls to go inside the membrane. From this breach site, buoyant salt water rises up as a jet and reacts at the interface with the alkaline silicate solution, forming a new precipitate, namely the hollow tube, that is totally separated and in which there is a totally different pH from the outer solution.[73]

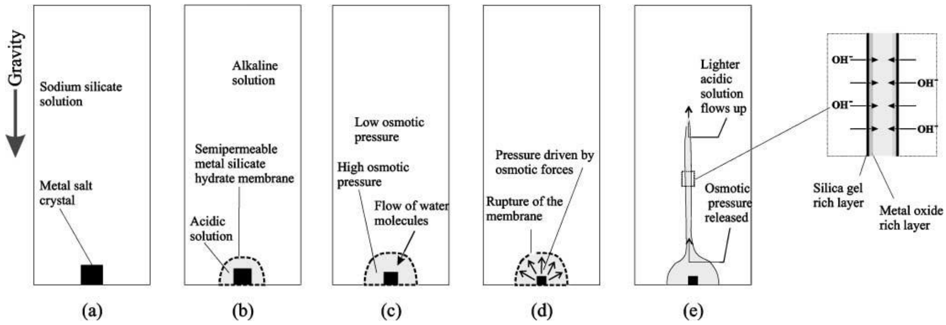

Figure 1.15 Chemical-garden growth: (a) setup at start of the reaction, (b) membrane formation between acidic and basic solutions, (c) osmotic pressure is higher within membrane than outside it, so it expands, (d) under osmotic forces the membrane ruptures, and (e) a tube forms.[12]

The morphological growth of a silica garden tube has generally two stages. First of all, fine opaque tubes, usually with a small bubble of gas at the tip, occasionally appear soon after seeding and grow rapidly, reaching the surface of the solution in a matter of seconds. The next generation growths form much more slowly and are in general thicker than the first ones, but not of uniform diameter. Gas bubbles are rarely attached to their tips, although many tiny bubbles are evolving from the membrane. After some time, a thin crust is formed on the surface of the solution. When the precipitate can no longer grow upwards, the growths spread out across the surface of the solution until the salt crystals are completely dissolved.[75]

Hydroxide ions that enter through the osmotic membrane react with the metal ions and precipitate on the inner surface of the tubes as metal hydroxides. The morphology of these silicate gardens depends on the evolution of the combination of forced convection driven by osmotic pressure through the semipermeable membrane and free convection due to buoyancy forces.[12]

It was found that lower concentrations produce clusters of narrow tubes, while higher concentrations produce single and wider tubes. Moreover, the growth behavior is strictly dependent on the decrease of the solubility of the salts: the more the metal salt is soluble the lower induction time and higher linear growth rate appear, growing wider tubes with flexible thin walls. On the other hand, the slower the growth rate the more robust tubes with thicker walls grow.[76],[77]

Furthermore, as the solution is more diluted, the membrane becomes more ‘‘elastic’’, allowing the formation of clusters of narrow tubes by repeated rupture and rehealing of the colloidal envelope. With salts characterized by the same metal cation but different non-precipitating anionic species, the 3D pattern obtained is rather similar in each case; some differences are reported just only in the growth rate.[78]

It is worth to stress that using pressed metal salt pellets, rather than irregular crystals, affects morphogenesis. On one hand, the rate of salt dissolution is lower for pellets than for random microcrystals, so that the kinetics of membrane precipitation changes. On the other hand, commercially available crystals often contain significant amounts of air enclosed in voids, which become released upon dissolution and may form a gas bubble that sometimes guides tube formation. This effect can be excluded in experiments with pressed pellets, especially if the tablets have been further degassed in vacuum prior to use. Considering this, salts with the highest possible amount of hydration water are better in order to minimize uncontrolled uptake of the partially strongly hygroscopic substances during grinding.[71],[76],[47],[79],[80]

About the evolution of chemical gradients in silica gardens deriving from metal salt pellet, it can be divided into four general stages. In the first 10 hours, what happens can be summarized into stage 1: when compartmentalization and dissolution of the metal salt pellet are completed, no more fresh metal ions (M^{2+}) are released, and metal hydroxide precipitation on the inner surface of the wall decreases their concentration. On the outer surface, silica precipitates due to the acidic pH inside the hollow tubes. Diffusion of the anions of the dissolved metal salt into the outer water glass reservoir happens simultaneously with the counter-diffusion of Na^+ ions. All these processes reduce the concentration and pH gradients across the membrane. Then, during stage 2, that happens between the 10th hour and the 25th, when all metal ions have been consumed by precipitation, the interior pH value is approximately neutral and low enough to prevent the passage of soluble silicate species through the membrane; silica which keeps on precipitating on the external surface. However, diffusion of OH^- ions into the inner solution is now possible and subsequently its pH is increased. During stage 3 ($25\ h<t<50\ h$), pH differences between the two reservoirs is strongly reduced by the diffusion of OH^-: the solubility of silica inside the tube increases and diffusion of silicate ions inside the tube occurs. On stage 4, after 50 hours from the beginning when all diffusion processes have finished, the pH values and the concentrations of all the species are the same on both sides of the membrane, and hence thermodynamic equilibrium is reached.

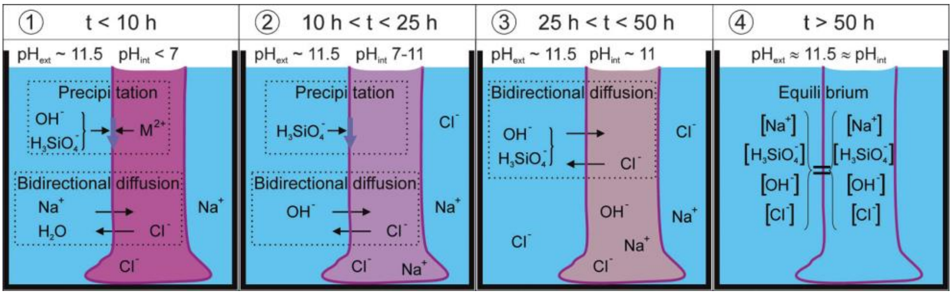

Figure 1.16 Scheme of the general stages proposed to describe the evolution of chemical gradients in a $CoCl_2$ silica garden after completed tube formation and metal salt dissolution. Note that, for simplicity, $H_3SiO_4^-$ represents all soluble silicate species present in the system.[47]

In order to study phase diagrams in reproducible experimental conditions, recently silica gardens have been studied using a horizontal Hell-Shaw cell, in this way having the control of the concentrations of the reagents and of the flow rate.[43],[81] Moreover, this setup allows the switch from dominant reaction-diffusion processes to flow-driven ones. Furthermore, the quasi-2D nature of the precipitates permits an easier characterization of the patterns using tools of classical 2D pattern selection analysis.[74],[82]
The Hele–Shaw cell consists of two transparent acrylate plates separated by a small gap filled by a solution of sodium silicate. The solution of the metal salt is then injected radially from the center of the lower plate at a fixed flow rate. When the two solutions are in contact, precipitation occurs. Different dynamics and patterns are observed when the concentrations of sodium silicate and metal salt change. In general, if one reagent is much more concentrated than the other one, it appears a circular precipitation pattern. If sodium silicate is the most concentrated reagent in the mix, the precipitate is concentrated at the outer rim as dark petals of flowers, out of which viscous fingers grow. Moreover, at the beginning of the injection, precipitation occurs inside the viscous fingers, whereas at longer times the precipitate lags behind them.
On the other hand, if the metal salt is much more concentrated than the sodium silicate solution, a compact circular precipitate grows radially. Above a critical radius, a destabilization of the circle rim toward small-scale hairs growing radially with a characteristic wavelength is observed.

When the concentration of both reactants is more or less equal, thin filaments growing with complex turnarounds grow, like worm spirals growing upon successive break-ups of precipitate walls. At later time, terrace-like precipitate layers grow along the first structure.

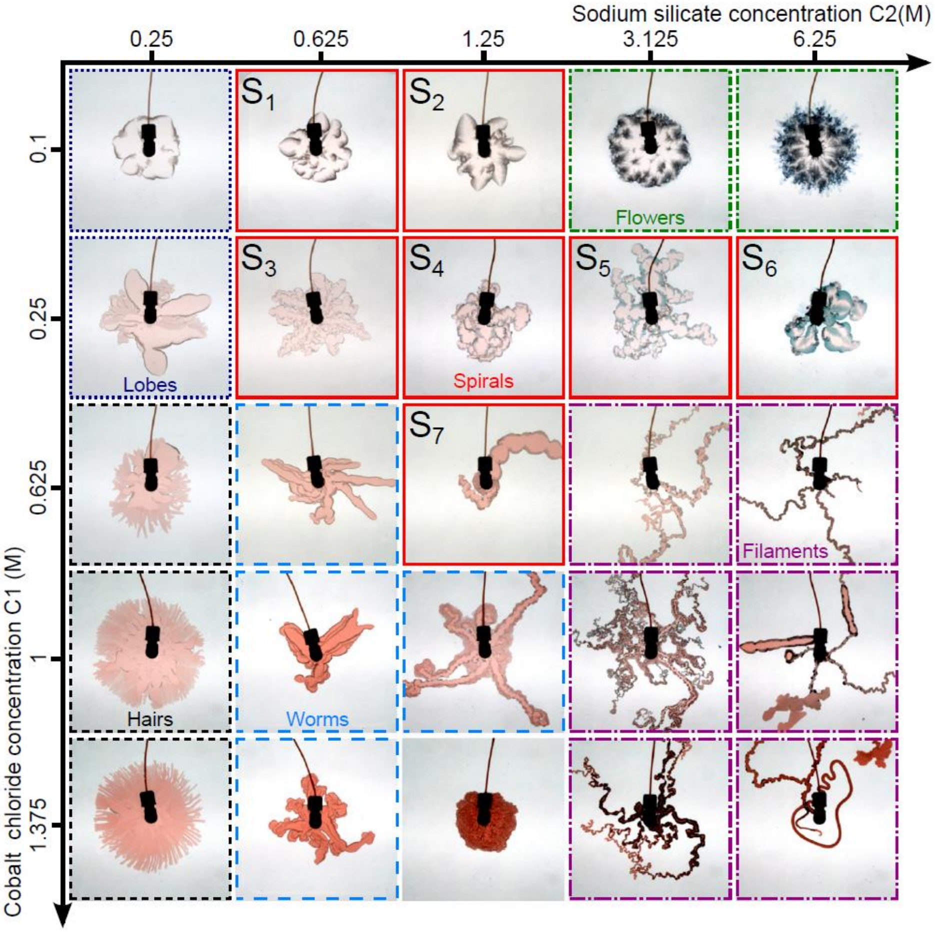

Figure 1.17 Experimental patterns of confined $CoCl_2$ chemical gardens, as a function of the concentration of the injected aqueous solution of cobalt chloride and the concentration of aqueous solution of sodium silicate. The diagram is divided into different colored frames referring to the various classes of patterns observed: lobes (dotted dark blue), spirals (solid red), hairs (dashed black), flowers (dashed-dotted green), filaments (long dashed-dotted purple), and worms (long dashed blue). Injection rate is Q=0.11 mL/s. Field of view: 15 cm × 15 cm.[74]

In other studies, it was found out that neither the nature of the cation of the metallic salt solution or its pH, nor the type of the anion of the alkaline solution influence significantly the precipitation patterns, which can be schematically sum up in the following scheme:

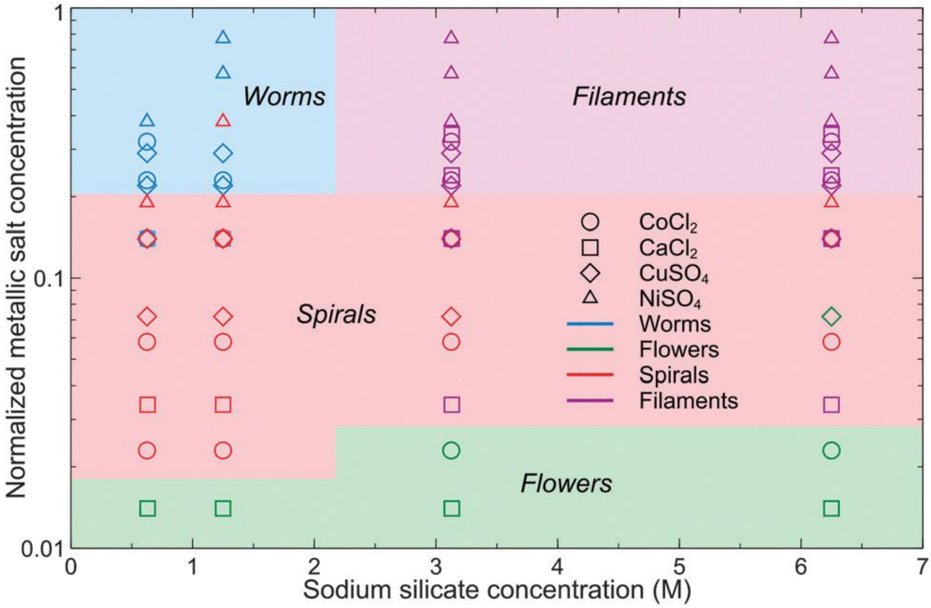

Figure 1.18 Phase diagram showing the distribution of the observed patterns for four different metallic salts ($CoCl_2$, $CaCl_2$, $CuSO_4$, $NiSO_4$) injected with the same flow rate into sodium silicate. The vertical axis is the normalized concentration of the metallic salt in a logarithmic scale and the horizontal axis is the concentration of the alkaline solution.[78]

These results agree with other studies in which it was found that, when buoyancy differences between the interior and exterior solutions are small, the rate of tube growth is constant and independent from the flow rate of metal salt solution. The growth rate is thus determined by chemical diffusion and chemical reactions rates. This growth rate determines also its radius: when the metal salt concentration is low and buoyancy effects are then more important, the growth rate increases and so the tube radius decreases.[72],[83] Moreover, in the first microgravity study on silica gardens, it was established unambiguously that precipitation tubes do not require gravitational convection.[84],[85]

1.3 Why measuring pH in biomorphs and silica gardens

At the beginning, it was thought that the presence of an external silica skin of biomorphs acted as a preformed template that determined the outer shape of the aggregates and the orientation of the crystallites inside.[9],[16],[24],[26] More recently, it was shown that the outer skin grows from secondary precipitation of silica on already fully developed crystal aggregates, as a consequence of the gradual decrease of bulk pH during the growth process, which reduces its solubility.[27]

In the past few years a more efficient model was proposed to explain this process.[11],[19],[27],[86],[87],[88] The formation of silica biomorphs starts with nucleation and growth of a single prismatic micron-sized crystal of witherite that is elongated along its *c* axis. This pseudohexagonal rod represents the core of all the observed morphologies and at the beginning suffers from crystal growth poisoning by oligomeric and/or polymeric silicate species.[15],[19],[89],[86],[90] The crystal core splits at its ends and develops tilted projections, emanating at noncrystallographic angles from the parent rod (figure 1.19). Splitting proceeds through the basal {001} planes or the {102} and {021} bipyramidal faces of the core crystal and is driven by the action of silica as an impurity that cannot be adsorbed under the prevailing conditions. Consequently, it is pushed ahead by the growing crystal front and generates 2D islands that are misoriented relative to the original lattice.[91],[92] This produces the branched first-generation projections that experience further poisoning and undergo continued splitting. This leads to a fractal branching motif, along which the crystal becomes increasingly bifurcated. Then, dumbbell-shaped structures are generated and with time evolve into space-filling cauliflower-like forms or closed spherulitic architectures.[20]

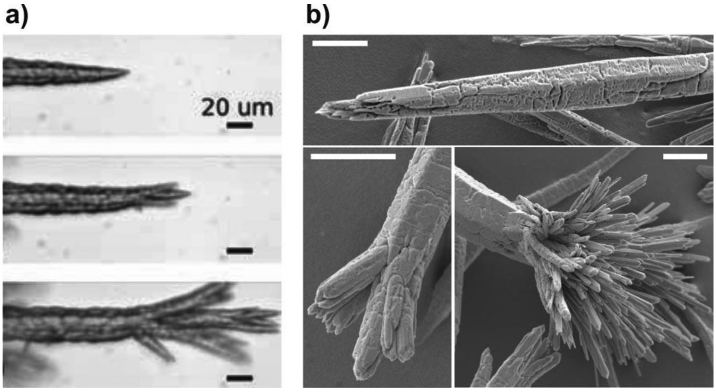

Figure 1.19 (a) Optical and (b) SEM micrographs of the splitting of a rod-like barium carbonate crystal at its tips in the presence of impurities. Scale bars: 5 μm.[20]

Over the range of pH values at which the formation of biomorphs typically occurs, both carbonate and hydrogen carbonate ions exist in significant amounts in the system. However, this implies that any carbonate particle growing in these alkaline media affect the hydrogen carbonate-carbonate equilibrium in its surroundings, as it consumes CO_3^{2-} ions:[93]

$$HCO_3^- \rightleftarrows CO_3^{2-} + H^+ \xrightarrow{Ba^{2+}} \downarrow BaCO_3.$$

Thus, hydrogen carbonate ions dissociate near the evolving carbonate surface, seeking to restore the locally perturbed solution equilibrium. This leads to a net release of protons close to the particles, which should lower the local pH. Thus, silica solubility decreases drastically as pH values around 9 or below are approached.[36]

The protons generated by dissociation of HCO_3^- ions are used to form free silanol groups (Si-OH), which participate to condensation processes that induce silica polymerization:

$$HCO_3^- + H_2O \leftrightarrows H_3O^+ + CO_3^{2-}$$

$$\text{-Si-O-} + H^+ \rightleftarrows \text{-Si-OH} + \text{HO-Si-} \xrightarrow{-H_2O} \text{-Si-O-Si-} \rightarrow\rightarrow \downarrow SiO_2.$$

Consequently, spontaneous precipitation of silica all over their surface occurs, and crystals are cemented in a layer of silica, which prevents them from growing larger than a few hundreds of nanometers.[86],[87],[88] In contrast, as polymerization of silica happens near the coated particles, the local pH is gradually re-elevated, because acidic silanol groups effectively vanish over ongoing condensation:

$$2\text{Si-OH} \rightarrow \text{Si-O-Si} + H_2O.$$

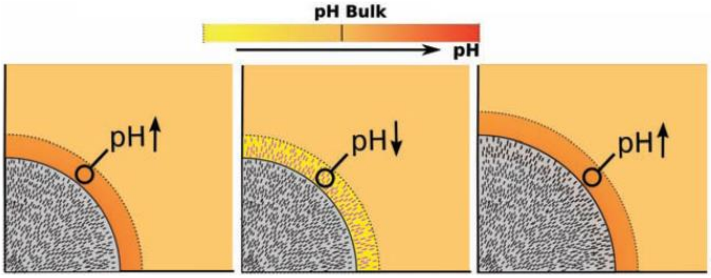

Figure 1.20 The growing of the fibrillated front due to the local oscillations of pH driven by the coupled precipitation of silica and carbonate.[86]

In this way, any increase in pH is associated to a shift in the equilibrium towards the side of CO_3^{2-}, increasing its local concentration:

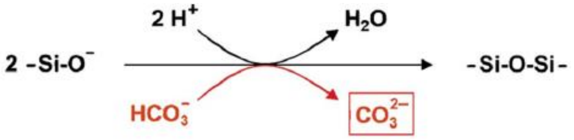

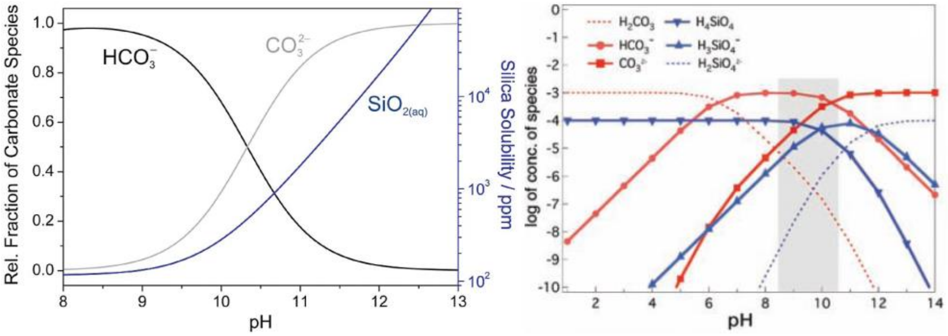

Figure 1.21 Left: Ideal distribution of carbonate species (black: hydrogen carbonate, gray: carbonate) in solution as a function of pH, compared to the pH-dependent solubility of silica (blue).[20] Right: The concentration of the chemical species as a function of pH and the pH region (gray) at which biomorphs form.[86]

This in turn makes silica polymerization raises the supersaturation of silicic acid close to growing carbonate crystals, thus provoking the adsorption and precipitation of silica on their positively charged surfaces, poisoning crystal growth and causing bifurcation of the crystals.[94] This chemical coupling ensures continuous splitting at non-crystallographic angles, leading to the formation of sheaf-of-wheat structures and, on further growth, to space-filling cauliflower like structures:[95],[96]

$$Si(OH)_4 \leftrightarrows SiO(OH)_3^- + H_3O^+ \text{ at pH} = 9$$

$$SiO(OH)_3^- \leftrightarrows SiO_2(OH)_2^{2-} + H_3O^+ \text{ at pH} = 10.7.$$

The newly formed crystallites then coat themselves by silica, stopping active growth, thus stimulating another round of carbonate nucleation.[86],[87],[88]

This autocatalytic chemical coupling generates the supersaturation needed to trigger mineralization of the carbonate phase and ensures also a continuous supply of polymeric silica “impurities” required to extend morphogenesis beyond the fractal pathway towards the continuous production and self-orientation of nanocrystals.

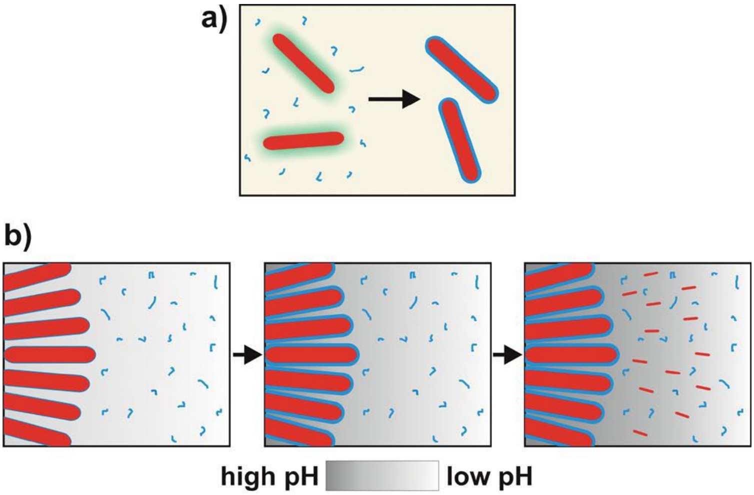

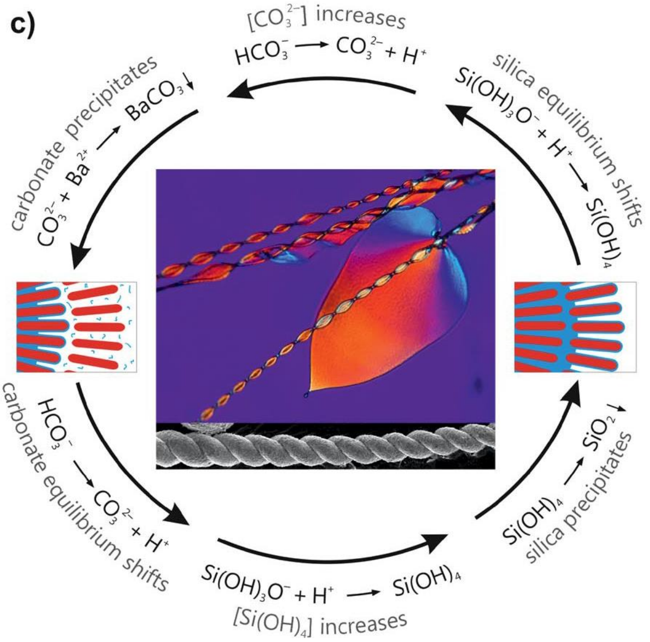

Figure 1.22 The chemical coupling. (a) Rod-like carbonate nanocrystals (red) become enveloped in silica (blue), as dissociation of hydrogen carbonate ions provokes a local decrease in pH (corresponding gradient in green). (b) Silica condensation reincreases the pH at the growing front, thus raising the supersaturation of barium carbonate in the local vicinity and causing a novel event of nucleation. (c) The loop process that these two processes provoke.[20]

It has to be stressed that such oscillations should be confined to regions where active growth takes place, and hence, they are not reflected in the bulk pH of the mother solutions. Therefore, supersaturation of the components is expected to be higher at the front of growth than elsewhere in the solution.[20]

At elevated pH values, where biomorphs are used to grow, silica solubility is more sensitive to change its pH value.[86] Therefore, the amount of silica coating the nanocrystals is large enough to provoke the stop of carbonate crystal growth. In turn, the precipitation of silica increases the local pH by converting the acidic -OH groups into siloxane bonds. This pH increasing promotes the formation of additional carbonate ions, increasing barium carbonate supersaturation and leading to a further round of carbonate nucleation in the form of 3D nuclei. This process causes the single-crystal growth front to fragment, creating a polycrystalline front of nanocrystals co-oriented with the single crystal, namely fibrillation. Subsequent silica precipitation prevents these nuclei from growing larger than the size of a few tens to hundreds of nanometers before they become almost fully coated with silica.

About the importance of measuring the pH of growing silica gardens, it can be said that understanding pH behavior inside the hollow tubes and on outer membrane on the front of their growth and in the bulk solution is important in order to comprehend the behavior of the diffusion forces that operates in the formation and growing of the structures.
In general, the pH of the exterior water glass reservoir (pH ~ 11.2) was not found to noticeably change, neither during growth nor after several days of maturation, due to the high excess and buffering ability of silica. On the other hand, the pH inside the tubes starts from acidic values for all cations, and subsequently increases in two distinct stages (examples reported in figure 1.23): first, a rather slow and continuous rise towards more or less neutral values is observed over a time that depends on the kind of metal salt used. Then, pH increases more steeply and eventually, after another 2–5 h, reaches levels close to that of the outer reservoir, indicating that the initially generated pH gradients across the membrane has vanished.[47]

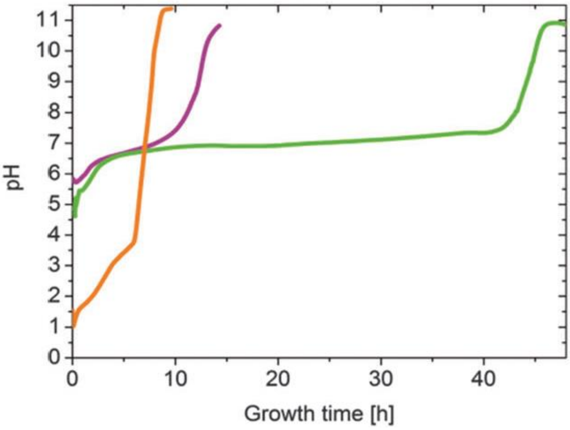

Figure 1.23 Temporal evolution of the pH inside silica garden tubes prepared with $CoCl_2$ (purple), $FeCl_2$ (green) and $FeCl_3$ (orange).[97]

It was also found that there is a correlation between these pH profiles and the temporal progression of the inner metal ion concentrations: the pH remains acidic as long as significant amounts of dissolved metal ions are present inside the tube. These results support previous studies in which it was observed that the incorporation of metal ions into the inner surface of the forming membranes occurs mainly through precipitation as amorphous hydroxides.[98],[75]

When arrived on the inner surface of the membrane, OH^- ions precipitate as soluble metal hydroxides during the first stage when the inner solution is still rich in metal cations. This leads to a continuous decrease in the metal ion concentration and, simultaneously, to a little increasing of the pH. When all metal ions are consumed, hydroxides ions diffusion becomes unhindered and provokes a higher rise of the pH until it is the same on both sides of the membrane.

As already mentioned, there are significant differences using different metal salts. The initial pH of the interior solution is much more acidic as the metal salt is stronger diprotic acid. The time required for the inner pH to ultimately become equal to that in the outer reservoir is also different considering different metal salts: larger pore sizes allow faster transport through the membrane, both during the earlier stages where precipitation is still ongoing and later when the point of equivalence has been reached.[97]

1.4 Objectives of the thesis

The aim of this thesis is to develop an experimental method to investigate the local pH changes at the microscopic level in the environment surrounding the crystal structures described in the previous sections during their growth in real time. On the basis of the observation that bulk pH influences the growth regime and the final shape of these systems, Garcia-Ruiz and coworkers postulated, in fact, a mechanism of growth that involves local pH alterations.[86],[47] However, this mechanism has never been experimentally demonstrated. My approach was based on the idea that local pH changes can be visualized using an accurately selected pH sensitive fluorophore (namely a pH chemosensor) that allows to map the pH variations responding to them with huge changes in its own fluorescence.

The intermediate objectives of my work have been the following workpackages:

1. Identification of a suitable pH fluorescent chemosensor for each system observed with different kind of microscopes. The choice was based on consideration upon the chemical and photophysical principles that regulate the response of fluorescent chemosensors. The aim was to find commercial or easily available indicators with appropriate pK_a suited on the different kind of systems I studied, with a fluorescence response to pH that allowed to visualize with high contrast the small expected local pH variations in real time during the crystals growth.

2. To develop a setup that allowed the acquisition of real time pH dependent fluorescence images. The purpose was to design a system where biomorphs or silica gardens formation and growth occurred in conditions suitable for the different kind of fluorescence microscopes used, having optical and geometrical features that allowed to optimize the contrast in the detection of the fluorescence changes due to the response of the indicator to the local pH variations in real time.

3. To develop a simple and direct method for the semi-quantitative elaboration of the data. Fluorescence recorded movies were expected to be directly interpretable from the qualitative point of view. Nevertheless, in order to actually evaluate the relative variation of the pH in proximity of the front of growth, electronic elaboration of the data was needed. Elaborating all the collected data, it would be possible to give fundamental information for understanding the mechanism of crystals growth.

1 References

[1] *Biomimetic Materials Chemistry*, Wiley-VCH, **1997**.

[2] F. C. Meldrum, H. Cölfen, *Chemical Reviews* **2008**, *108*, 4332-4432.

[3] A.-W. Xu, Y. Ma, H. Cölfen, *Journal of Materials Chemistry* **2007**, *17*, 415-449.

[4] R.-Q. Song, H. Cölfen, *CrystEngComm* **2011**, *13*, 1249-1276.

[5] U. Tritschler, A. E. S. Van Driessche, A. Kempter, M. Kellermeier, H. Cölfen, *Angewandte Chemie International Edition* **2015**, *54*, 4083-4086.

[6] J. W. McCauley, R. Roy, *American Mineralogist* **1974**, *59*, 947-963.

[7] A. L. Herrera, *Mémoires Société Scientifique “Antonio Alzate”, Vol. 32*, **1912**.

[8] J. M. Garcia Ruiz, J. L. Amoros, *Journal of Crystal Growth* **1981**, *55*, 379-383.

[9] J. M. Garcia Ruiz, J. L. Amoros, *Bull. Mineral.* **1981**, *104*, 107-113.

[10] J. M. Garcia Ruiz, *Cryst. Growth* **1985**, *73*, 251-262.

[11] E. Melero-Garcia, R. Santisteban-Bailon, J. M. Garcia-Ruiz, *Cryst Growth Des* **2009**, *9*, 4730-4734.

[12] J. H. E. Cartwright, J. M. García-Ruiz, M. L. Novella, F. Otálora, *Journal of Colloid and Interface Science* **2002**, *256*, 351-359.

[13] J. M. Garcia-Ruiz, S. T. Hyde, A. M. Carnerup, A. G. Christy, M. J. Van Kranendonk, N. J. Welham, *Science* **2003**, *302*, 1194-1197.

[14] D. Genovese, M. Montalti, F. Otálora, J. Gómez-Morales, M. Sancho-Tomás, G. Falini, J. M. García-Ruiz, *Cryst Growth Des* **2016**, *16*, 4173-4177.

[15] J. M. Garcia-Ruiz, *Geology* **1998**, *26*, 843-846.

[16] S. T. Hyde, A. M. Carnerup, A. K. Larsson, A. G. Christy, J. M. Garcia-Ruiz, *Physica A* **2004**, *339*, 24-33.

[17] E. Bittarello, D. Aquilano, *Eur J Mineral* **2007**, *19*, 345-351.

[18] A. E. Voinescu, M. Kellermeier, A. M. Carnerup, A. K. Larsson, D. Touraud, S. T. Hyde, W. Kunz, *J Cryst Growth* **2007**, *306*, 152-158.

[19] J. Eiblmeier, M. Kellermeier, D. Rengstl, J. M. Garcia-Ruiz, W. Kunz, *Crystengcomm* **2013**, *15*, 43-53.

[20] M. Kellermeier, H. Cölfen, J. M. Garcia-Ruiz, *Eur J Inorg Chem* **2012**, 5123-5144.

[21] J. M. Garcia Ruiz, A. Moreno, *Anales de Quimica Int. Ed.* **1997**, *93*, 1-2.

[22] J. P. Reyes-Grajeda, D. Jáuregui-Zúñiga, N. Batina, M. Salmón-Salazar, A. Moreno, *J Cryst Growth* **2002**, *234*, 227-236.

[23] L. Addadi, S. Weiner, *Angewandte Chemie International Edition in English* **1992**, *31*, 153-169.

[24] M. Kellermeier, F. Glaab, A. M. Carnerup, M. Drechsler, B. Gossler, S. T. Hyde, W. Kunz, *J Cryst Growth* **2009**, *311*, 2530-2541.

[25] E. Bittarello, F. R. Massaro, D. Aquilano, *J Cryst Growth* **2010**, *312*, 402-412.

[26] A. E. Voinescu, M. Kellermeier, B. Bartel, A. M. Carnerup, A. K. Larsson, D. Touraud, W. Kunz, L. Kienle, A. Pfitzner, S. T. Hyde, *Cryst Growth Des* **2008**, *8*, 1515-1521.

[27] M. Kellermeier, E. Melero-García, F. Glaab, J. Eiblmeier, L. Kienle, R. Rachel, W. Kunz, J. M. García-Ruiz, *Chemistry – A European Journal* **2012**, *18*, 2272-2282.

[28] T. Baird, P. S. Braterman, P. Chen, J. M. García-Ruíz, R. D. Peacock, A. Reid, *Materials Research Bulletin* **1992**, *27*, 1031-1040.

[29] T. Terada, S. Yamabi, H. Imai, *J Cryst Growth* **2003**, *253*, 435-444.

[30] J. A. Speer, *Rev. Mineral.* **1983**, *11*, 145-190.

[31] S. T. Hyde, J. M. Garcia-Ruiz, *Actual Chimique* **2004**, 4-6.

[32] C. T. Kresge, M. E. Leonowicz, W. J. Roth, J. C. Vartuli, *Nature* **1992**, *359*, 710-712.

[33] G. Zhang, J. M. Delgado-Lopez, D. Choquesillo-Lazarte, J. M. Garcia-Ruiz, *Crystengcomm* **2013**, *15*, 6526-6532.

[34] G. Zhang, J. M. Delgado-Lopez, D. Choquesillo-Lazarte, J. M. Garcia-Ruiz, *Cryst Growth Des* **2015**, *15*, 564-572.

[35] M. Kellermeier, F. Glaab, E. Melero-García, J. M. García-Ruiz, in *Methods in Enzymology, Vol. 532* (Ed.: J. J. D. Yoreo), Elsevier Inc., **2013**, pp. 225-256.

[36] R. K. Iler, **1979**.

[37] S. Dominguez Bella, J. M. Garcia-Ruiz, *J Cryst Growth* **1986**, *79*, 236-240.

[38] S. Dominguez Bella, J. M. Garcia-Ruiz, *J Mater Sci* **1987**, *22*, 3095-3102.

[39] H. Imai, T. Terada, S. Yamabi, *Chemical Communications* **2003**, 484-485.

[40] G. Zhang, J. Morales, J. M. Garcia-Ruiz, *Journal of Materials Chemistry B* **2017**, *5*, 1658-1663.

[41] E. Schönherr, *Advanced Materials* **1989**, *1*, 91-92.

[42] K. Jabłczyński, S. Kobryner, *La formation rythmique des précipités: les anneaux de Liesegang*, Bureaux de la Société, **1926**.

[43] R. Makki, L. Roszol, J. J. Pagano, O. Steinbock, *Philos T R Soc A* **2012**, *370*, 2848-2865.

[44] S. Leduc, *The Mechanism of Life*, William Heinemann, **1911**.

[45] A. L. Herrera, *Boletín de la Dirección de estudios biológicos, Vol. 1-2*, Mexico, **1916-1917**.

[46] M. Zeleny, J. Klir, K. D. Hufford, (Ed.: C. Langton), Addison-Wesley, Reading, MA, **1988**.

[47] F. Glaab, M. Kellermeier, W. Kunz, E. Morallon, J. M. Garcia-Ruiz, *Angew Chem Int Edit* **2012**, *51*, 4317-4321.

[48] D. D. Double, A. Hellawell, *Nat Chem* **1976**, *261*, 486-488.

[49] G. Butler, H. C. K. Ison, *Nature* **1958**, *182*, 1229-1230.

[50] J. H. E. Cartwright, B. Escribano, D. L. Gonzalez, C. I. Sainz-Diaz, I. Tuval, *Langmuir* **2013**, *29*, 7655-7660.

[51] C. Collins, G. Mann, E. Hoppe, T. Duggal, T. L. Barr, J. Klinowski, *Phys Chem Chem Phys* **1999**, *1*, 3685-3687.

[52] C. Collins, R. Mokaya, J. Klinowski, *Phys Chem Chem Phys* **1999**, *1*, 4669-4672.

[53] M. J. Russell, A. J. Hall, *Journal of the Geological Society* **1997**, *154*, 377-402.

[54] L. M. Barge, I. J. Doloboff, L. M. White, G. D. Stucky, M. J. Russell, I. Kanik, *Langmuir* **2012**, *28*, 3714-3721.

[55] G. J. T. Cooper, A. G. Boulay, P. J. Kitson, C. Ritchie, C. J. Richmond, J. Thiel, D. Gabb, R. Eadie, D. L. Long, L. Cronin, *J Am Chem Soc* **2011**, *133*, 5947-5954.

[56] S. Thouvenel-Romans, O. Steinbock, *J Am Chem Soc* **2003**, *125*, 4338-4341.

[57] J. L. Pagano, T. Bansagi, O. Steinbock, *Angew Chem Int Edit* **2008**, *47*, 9900-9903.

[58] R. Makki, O. Steinbock, *J Am Chem Soc* **2012**, *134*, 15519-15527.

[59] L. Roszol, R. Makki, O. Steinbock, *Chem Commun* **2013**, *49*, 5736-5738.

[60] M. J. Russell, A. J. Hall, D. Turner, *Terra Nova* **1989**, *1*, 238-241.

[61] K. A. Ludwig, C.-C. Shen, D. S. Kelley, H. Cheng, R. L. Edwards, *Geochimica et Cosmochimica Acta* **2011**, *75*, 1869-1888.

[62] J. B. Corliss, J. Dymond, L. I. Gordon, J. M. Edmond, R. P. von Herzen, R. D. Ballard, K. Green, D. Williams, A. Bainbridge, K. Crane, T. H. van Andel, *Science* **1979**, *203*, 1073-1083.

[63] M. J. Russell, A. J. Hall, A. G. Cairns-Smith, P. S. Braterman, *Nature* **1988**, *336*, 117-117.

[64] T. H. Hazlehurst, *Journal of Chemical Education* **1941**, *18*, 286.

[65] W. Pfeffer, *Osmotic investigations: Studies on cell mechanics*, Van Nostrand Reinhold, **1985**.

[66] M. Copisarow, *Journa of the Chemical Society* **1927**, 222-234.

[67] R. Makki, O. Steinbock, *J Phys Chem C* **2011**, *115*, 17046-17053.

[68] B. C. Batista, P. Cruz, O. Steinbock, *Langmuir* **2014**, *30*, 9123-9129.

[69] M. R. Bentley, B. C. Batista, O. Steinbock, *J Phys Chem A* **2016**, *120*, 4294-4301.

[70] J. Pantaleone, A. Toth, D. Horvath, L. RoseFigura, W. Morgan, J. Maselko, *Phys Rev E* **2009**, *79*.

[71] A. Baker, A. Toth, D. Horvath, J. Walkush, A. S. Ali, W. Morgan, A. Kukovecz, J. J. Pantaleone, J. Maselko, *J Phys Chem A* **2009**, *113*, 8243-8248.

[72] V. Kaminker, J. Maselko, J. Pantaleone, *J Chem Phys* **2014**, *140*.

[73] E. Nakouzi, O. Steinbock, *Sci Adv* **2016**, *2*.

[74] F. Haudin, J. H. E. Cartwright, F. Brau, A. De Wit, *Proceedings of the National Academy of Sciences* **2014**, *111*, 17363-17367.

[75] C. Collins, W. Z. Zhou, A. L. Mackay, J. Klinowski, *Chem Phys Lett* **1998**, *286*, 88-92.

[76] J. H. E. Cartwright, B. Escribano, C. I. Sainz-Díaz, *Langmuir* **2011**, *27*, 3286-3293.

[77] D. R. Lide, *CRC Handbook of Chemistry and Physics*, CRC Press, Boston, **1991**.

[78] F. Haudin, V. Brasiliense, J. H. E. Cartwright, F. Brau, A. De Wit, *Phys Chem Chem Phys* **2015**, *17*, 12804-12811.

[79] J. Maselko, A. Geldenhuys, J. Miller, D. Atwood, *Chem Phys Lett* **2003**, *373*, 563-567.

[80] J. Maselko, P. Strizhak, *The Journal of Physical Chemistry B* **2004**, *108*, 4937-4939.

[81] Á. Tóth, D. Horváth, R. Smith, J. R. McMahan, J. Maselko, *The Journal of Physical Chemistry C* **2007**, *111*, 14762-14767.

[82] M. Cross, H. Greenside, *Pattern Formation and Dynamics in Nonequilibrium Systems*, Cambridge Univ Press, Cambridge (United Kingdom), **2009**.

[83] J. H. E. Cartwright, B. Escribano, C. I. Sainz-Díaz, L. S. Stodieck, *Langmuir* **2011**, *27*, 3294-3300.

[84] D. E. H. Jones, U. Walter, *Journal of Colloid and Interface Science* **1998**, *203*, 286-293.

[85] D. E. H. Jones, *American Scientist* **2002**, *90*, 454-461.

[86] J. M. Garcia-Ruiz, E. Melero-Garcia, S. T. Hyde, *Science* **2009**, *323*, 362-365.

[87] W. Kunz, M. Kellermeier, *Science* **2009**, *323*, 344-345.

[88] M. Kellermeier, E. Melero-García, W. Kunz, J. M. García-Ruiz, *Journal of Colloid and Interface Science* **2012**, *380*, 1-7.

[89] J. M. G. Ruiz, A. Canerup, A. G. Christy, N. J. Welham, S. T. Hyde, *Astrobiology* **2002**, *2*, 353-369.

[90] M. Kellermeier, J. Eiblmeier, E. Melero-García, M. Pretzl, A. Fery, W. Kunz, *Cryst Growth Des* **2012**, *12*, 3647-3655.

[91] H. D. Keith, F. J. P. Jr., *Journal of Applied Physics* **1963**, *34*, 2409-2421.

[92] N. Goldenfeld, *Journal of Crystal Growth* **1987**, *84*, 601-608.

[93] M. Kellermeier, E. Melero-Garcia, F. Glaab, R. Klein, M. Drechsler, R. Rachel, J. M. Garcia-Ruiz, W. Kunz, *J Am Chem Soc* **2010**, *132*, 17859-17866.

[94] C.-C. Li, J.-H. Jean, *Journal of the American Ceramic Society* **2002**, *85*, 2977-2983.

[95] D. P. Grigoriev, *Ontogeny of Minerals*, Jerusalem (Israel), **1965**.

[96] M. N. Maleev, *Tschermaks Mineral. Petrogr. Mitt.* **1972**, *18*.

[97] F. Glaab, J. Rieder, J. M. Garcia-Ruiz, W. Kunz, M. Kellermeier, *Phys Chem Chem Phys* **2016**, *18*, 24850-24858.

[98] J. J. Pagano, S. Thouvenel-Romans, O. Steinbock, *Phys Chem Chem Phys* **2007**, *9*, 110-116.

2 Fluorescence based pH mapping

Detection of fluorescence emission offers many advantages for investigating local chemical properties: first of all, it is a high sensitive and, even more importantly, non-invasively technique, since the fluorescence can be acquired without direct contact with the detection instrument.[1] Moreover, fluorescence based methods permit good selectivity, short response time, real-time monitoring, and in situ observation.[2],[3],[4],[5],[6],[7] Finally, they afford much greater spatial sampling capability compared to other common techniques.[8],[9],[10]

The use of **fluorescent probes**, hence molecules that show a fluorescent signal dependent on the chemical properties of the local environment (and in particular the **pH**), is a powerful tool to perform chemical imaging. However, measurements based on the detection of simple fluorescence intensity changes may be influenced by many factors, including sample geometry, changes of temperature, fluctuations in the excitation intensities, varied emission collection efficiencies, probe bleaching, washout and light losses in the detection optics or in the samples.[11]

These undesired effects can be in part minimized by exploiting probes that respond to pH changes with a dramatic **switch on** of the luminescence.

One of the techniques that best exploit the advantages of fluorescence emission is fluorescence microscopy, which allows to follow local changes of the concentration of specific non fluorescent analytes, and in particular pH, in real time using molecular, supramolecular or nanosized systems (also called chemosensors) able to convert such changes in a detectable modification of their emission properties.

The use of fluorescent chemosensors have been, up to now, mostly limited to the investigation of biological processes at the cellular level where it was demonstrated to be an extremely powerful tool which allows to combine high space and temporal resolution and to follow biological events continuously and in real time. In particular, since pH is a fundamental parameter in the regulation of many cellular processes, a significant variety of fluorescent indicators for the physiological windows has been proposed.[12]

In this PhD research work we propose, in a very unusual and innovative approach, the application of fluorescence based pH sensing to investigate the dynamic of growth and the real-time evolution of the local properties of completely inorganic systems of fully inorganic microstructures, namely biomorphs and silica gardens.

2.1 General concepts

Fluorescence occurs when a molecule A is excited to a high energy electronic states by a radiation of a given wavelength (λ_{exc}). At low concentration regime, where the optical filter effects are negligible, the molecules absorb photons with a probability proportional to its molar absorption coefficient $\varepsilon(\lambda_{exc})$. The resulting excited state molecules A*, hence, emits a photon at a given λ_{em} with a probability proportional to the product $\alpha \cdot \varphi$, where φ is the fluorescence quantum yield and α is a wavelength dependent function which represents the spectral distribution of the emission (it results from the normalization of the emission spectrum). Since the concentration of the excited states in given excitation condition is proportional to the one of the ground state, the resulting fluorescence intensity (I) at a given emission wavelength is:

$$I = f\, \varepsilon\, \alpha\, \varphi\, [A]$$

where f is a proportional factor which is characteristic of the instrumental setup and [A] is the concentration of not excited molecule.[13] More in general, the total emission is the sum of the contributions of all the different species.

The mechanism of response of a fluorescent pH probe is based on the protonation of the A molecule to give a species AH^+ with different photophysical properties. Hence, in order to behave as a pH probe, the molecule A has, first of all, to have a protonable site.

The local concentration of the two forms A and AH^+ depends on the local pH:

$$AH^+ \underset{+\,H^+}{\overset{-\,H^+}{\rightleftharpoons}} A$$

As a consequence, the local fluorescence intensity, that is given by the sum of the contribution of the A and AH^+ species, is:

$$I = f(\varepsilon_A \alpha_A \varphi_A [A] + \varepsilon_{AH^+} \alpha_{AH^+} \varphi_{AH^+} [AH^+]),$$

and it is dependent on pH.

In a homogeneous equilibrated system, the total concentration of the fluorophore is constant, namely $[A] + [AH^+] = c_A$ (where c_A is the analytical concentration of A) and the local pH has a constant value. In this condition,

$$I = f(\varepsilon_A \alpha_A \varphi_A - \varepsilon_{AH^+} \alpha_{AH^+} \varphi_{AH^+})\chi_A + f\varepsilon_{AH^+} \alpha_{AH^+} \varphi_{AH^+},$$

where χ_A is the molar fraction of A. This means that a response to a pH change is expected only in the case in which $\varepsilon_A \alpha_A \varphi_A \neq \varepsilon_{AH^+} \alpha_{AH^+} \varphi_{AH^+}$, namely when, as already mentioned, the photophysical properties of A and AH^+ are different.

In very alkaline condition ($pH \gg pK_a$, where K_a is the acidic constant of A), $\chi_A = 1$ and hence:

$$I = I_2 = f(\varepsilon_A \alpha_A \varphi_A - \varepsilon_{AH^+} \alpha_{AH^+} \varphi_{AH^+}) + f\varepsilon_{AH^+} \alpha_{AH^+} \varphi_{AH^+}.$$

On the contrary, in very acidic conditions ($pH \ll pK_a$), $\chi_A = 0$:

$$I = I_1 = f\varepsilon_{AH^+} \alpha_{AH^+} \varphi_{AH^+}$$

and hence:

$$I = (I_2 - I_1)\chi_A + I_1.$$

Taking into account such equation, we can conclude that the maximum relative signal variation will be given by I_1/I_2.

2.2 Specific features required for biomorphs and silica gardens

In general, pH fluorescent probes present some unique advantageous features: i) they can be detected with a simple optical setup since their emission color is different from the excitation color ($\lambda_{em}>\lambda_{exc}$) and the excitation wavelength can be eliminated by optical filtering; ii) the response time, hence the time delay between excitation and emission, is typically of the order of 10^{-9} s, so that molecular diffusion is negligible, hence iii) local detection is possible.
Nevertheless, no probes are presently available for general application and the pH fluorescent probes have to be chosen strictly taking into account the properties of the system under investigation.

The first part of our research was devoted to the identification of pH fluorescence probes suitable for studying the formation of biomorphs and silica gardens. The inorganic systems under investigation present a common hydrophilic matrix (e.g. silica solutions, silica gels, metal ions solutions), hence the first feature required for the pH probes was water solubility and compatibility.
Other desired features included:

1) an appropriate pK_a. Each probe in fact gives optimal response to pH changes in the $pK_a \pm 1$ interval;
2) high extinction coefficient and fluorescence quantum yield with absorption/excitation and emission bands in the visible region. This is necessary to have bright probes compatible with the

excitation light sources and optical components (filters, objectives and detectors) tipically used in fluorescence microscopy;

3) very good photostability as well as chemical and thermal stability. This allows to minimize (photo-)bleaching effects and to achieve long-term investigation of the samples under continuous irradiation;
4) specific response only to the analyte of interest (H_3O^+ ions) is also fundamental to avoid false responses. pH sensors can be cross-sensitive toward metal ions which limits their use in practical applications unless corrections;[14]
5) possibly, a large Stokes shift. This feature allows to reduce the signal to noise ratio and hence to improve the sensitivity.

As mentioned in point 1, the pK_a of the fluorophore is a very important parameter, due to the fact that the actual response of the probe to pH variations depends on it. It is also useful, if possible, to know if the pH is expected to decrease or increase during the observation. Concerning biomorphs, as previous mentioned, they grow in a bulk solution with pH about 10.6 and a decrease of the pH is expected during their formation. Hence a probe with a poor emission at biomorphs bulk pH and OFF-ON response to protonation has to be preferred in order to avoid strong background fluorescence, and to obtain an easily detectable signal upon pH lowering. For these reasons only chemosensors that switch on their emission upon protonation are suitable for this kind of systems.[6]

Moreover, a probe with a pK_a close to 10.6 is needed. In fact, if we consider as examples two chromophores with respectively two different pK_a, one with a value much lower than 10.6 and the other with a value much higher, we expect the behavior schematized in figure 2.1. In the former case ($pK_a \ll 10.6$) the bulk signal coming from the sample is weak (as required) but the fluorescence change is also very weak upon moderate decrease of the pH. In the latter case ($pK_a \gg 10.6$), on the other hand, the bulk emission is very strong and it masks the local pH changes that produce a small relative increase of fluorescence.

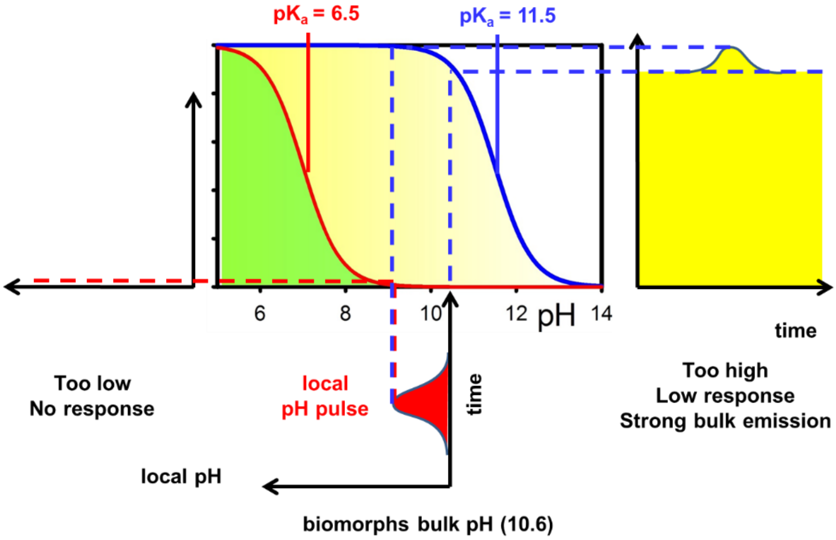

Figure 2.1 Example of fluorescent indicators with different pK$_a$ and their effect on visualizing biomorphs local pH decreases.

In conclusion, as schematized in figure 2.2, it is important to have a fluorescent probe that exhibits a pK$_a$ near the range of biomorphs local pH pulse. In fact, as we mentioned, the dynamic of the response of the fluorescent chemosensor is the result of the protonation equilibrium. Going more into the detail, according to the protonation equilibrium, at pH=pK$_a$ the 50% of the indicator is in the acidic form and the 50% in the alkaline one. In the range from pH=pK$_a$-1 and pH=pK$_a$+1 the concentration of the protonated form goes from 10% to 90%, hence in this region the variation of the fluorescence signal is 80% of the total difference between the emission of fully protonated and completely deprotonated forms. This means that the sensitivity of the sensor, which is $\frac{\Delta I_{norm}}{\Delta pH}\left(\text{where } \Delta I_{norm}=\frac{\Delta I}{(I_1-I_2)}\right)$, is 0.4 in this range but becomes much lower at pH higher than pK$_a$+1 and at pH lower than pK$_a$-1.

From the photophysical point of view, the OFF/ON behavior can be achieved either using a molecule with a small fluorescence quantum yield in the alkaline form and a high one in the acidic one or by exploiting selective excitation of a dye which is fluorescent in both forms but absorbs at a given wavelength only in the acidic one. This can be possible for example by taking advantage of a red shift of the absorption spectrum upon protonation. This last option guarantee, as an advantage, that only a small fraction of dye, namely the protonated one, is continuously excited. This approach allows to minimize the production of excited states and hence the photobleaching in a long term experiments.

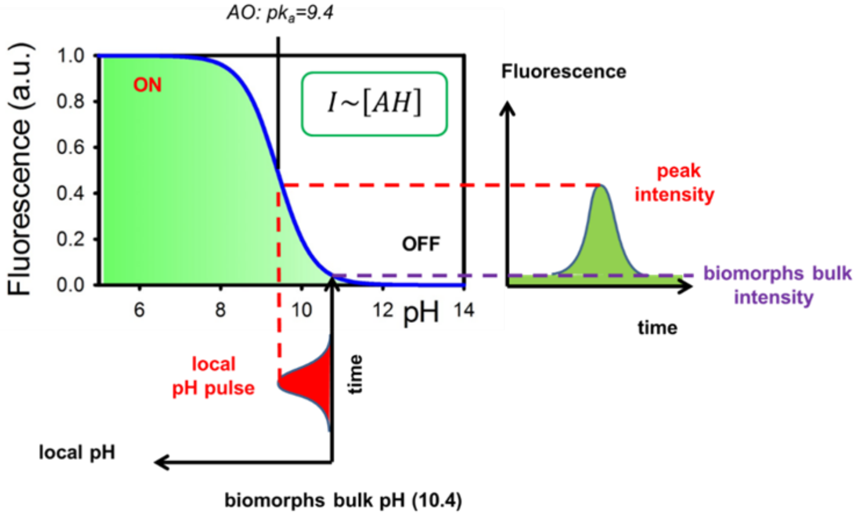

Figure 2.2 Principle of OFF/ON pH sensor for H_3O^+ ions: example given with AO (acridine orange).

For the study of silica gardens we followed a similar approach for identifying a suitable pH probe. Silica gardens are compartmentalized systems made by two solutions separated by a self-assembled membrane. The two solutions, the metal and the silicate one, have very different pH being the former acidic and the latter strongly alkaline. In particular, pH is between 11 and 12 (depending on the fraction of water) for sodium silicate, while metal salt saturated solution may show pH as low as 3: this means that local pH mapping requires to operate in very different pH windows in the inner part of the membrane of the hollow tubes with respect to the outer one. Hence different pH probes may be needed for the two solutions. Moreover, in silica gardens the two solutions can in principle be investigated independently by solubilizing the probes either in the metal or in the silicate.

We would like to stress that, because of the complexity of the system and in particular the presence of concentrated electrolyte, the behavior of the fluorescent dye is far from being ideal. Nevertheless, the experimental results showed that the fluorescence response can be fitted with a simplified model with an apparent pK_a. Hence, for simplicity, we did not consider explicitly the non-ideal factors in this work.

2.3 The pH fluorescent probes (AO, AY, HTPS)

Considering the requirements summarized in the previous section, we chose **acridine orange (AO)** and **acridine yellow (AY)** as promising candidate probes for mapping pH in biomorphs. In fact, we found out that these molecules are soluble in the silicate solution in which the crystal growth takes place, both in the acidic and alkaline form. Moreover, since we expected a local decrease of pH lower than one unit in this system, we decided to choose an indicator with pK_a close to the pH_{bulk} to optimize the sensitivity. These pH chemosensors are weakly fluorescent in the bulk of the solution ($pH_{bulk} \approx 10.6$) and they respond with a dramatic enhancement of the fluorescence to a local decrease of pH. These sensors hence behave as an OFF/ON sensor for H_3O^+ ions.

As already mentioned, these properties are important to minimize the background signal in fluorescence microscopy since they allow to increment the relative contribution of the observed fluorescence due to the small fraction of solution at the interface where biomorphs front grows, which is the main objective of our study.

This reduction of the background signal is particularly important for wide field microscopy where a large part of the sample is simultaneously excited and observed. In fact, the detector (a CCD camera) used for imaging in the wide field setup collects both the signal that derives from the small layer of solution that surrounds biomorphs (that is focused on the CCD sensor by the microscope objective) and the background fluorescence from the large volume of the bulk solution (which is out of focus). In order to minimize background signal, it is essential that the dye in the bulk has to be not emitting, otherwise emission deriving from biomorph would be covered by bulk signal.

2.3.1 Photophysical properties of AO in solution and in gel

The first fluorescent probe we used for mapping pH in silica gel during biomorphs formation is acridine orange (AO). The molar absorption coefficient of AO is about 2.7×10^4 $M^{-1}cm^{-1}$ at 430 nm and its fluorescence QY is 0.2. This fluorophore presents a nitrogen site that can be protonated at acidic pH, so the local concentration of the cationic and neutral forms depends on the local pH:

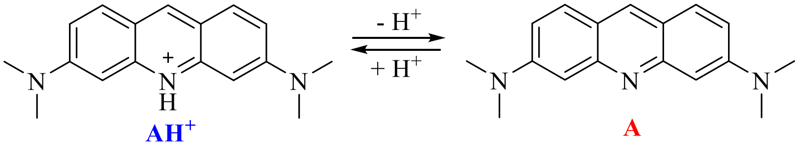

,

that could be seen as

$$AH^+ \underset{+\,H^+}{\overset{-\,H^+}{\rightleftarrows}} A$$

.

In order to find the analytical dependence of the fluorescence intensity on pH, we can consider that:

$$K_a = \frac{[A][H^+]}{[AH^+]}.$$

If $[AH^+]$ is set up as x it will result:

$$K_a = \frac{[c_A - x][H^+]}{x},$$

where c_A is the analytical concentration of AO.

In order to explicate x, it is found that:

$$xK_a = c_A[H^+] - x[H^+]$$

$$\Rightarrow x(K_a + [H^+]) = c_A[H^+]$$

$$\Rightarrow x = \frac{c_A[H^+]}{K_a + [H^+]}.$$

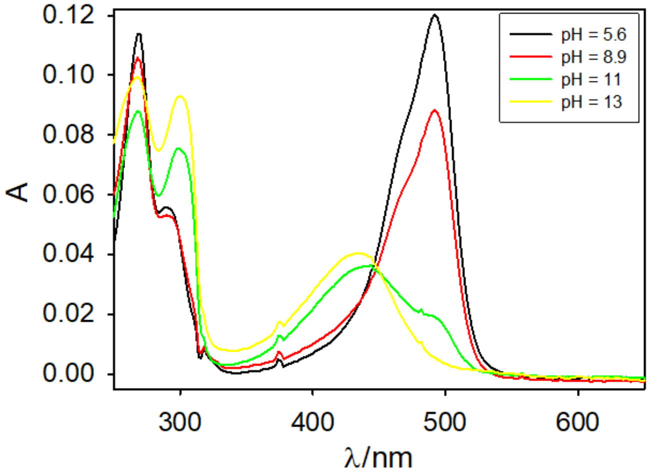

Figure 2.3 Absorbance spectra of AO as a function of pH in buffer solutions.

According to the equations previously shown, if molar fraction is considered, the equation of fluorescence intensity becomes:

$$I = I_0\frac{[AH^+]}{c_A} + I_\infty\frac{[A]}{c_A} = I_0\frac{[AH^+]}{c_A} + I_\infty\frac{c_A - [AH^+]}{c_A} =$$

$$= I_0\frac{x}{c_A} + I_\infty\frac{c_A - x}{c_A}.$$

At this stage, x is replaced by the expression found above:

$$I = I_0\frac{\frac{c_A[H^+]}{K_a + [H^+]}}{c_A} + I_\infty\frac{c_A - \frac{c_A[H^+]}{K_a + [H^+]}}{c_A} =$$

$$= \frac{I_0[H^+]}{K_a + [H^+]} + I_\infty \left(1 - \frac{[H^+]}{K_a + [H^+]}\right) =$$

$$= \frac{I_0[H^+]}{K_a + [H^+]} + I_\infty \left(\frac{K_a}{K_a + [H^+]}\right),$$

and then

$$I = \frac{I_0[H^+] + K_a I_\infty}{K_a + [H^+]}.$$

The intensity I_0 and I_∞ depends on the experimental condition and can be determined, together with k_a, by performing a set of measurements of fluorescence intensity at different pH values and using the last equation for fitting the data. We would like to stress that a similar approach can be used for the UV-Vis absorbance.

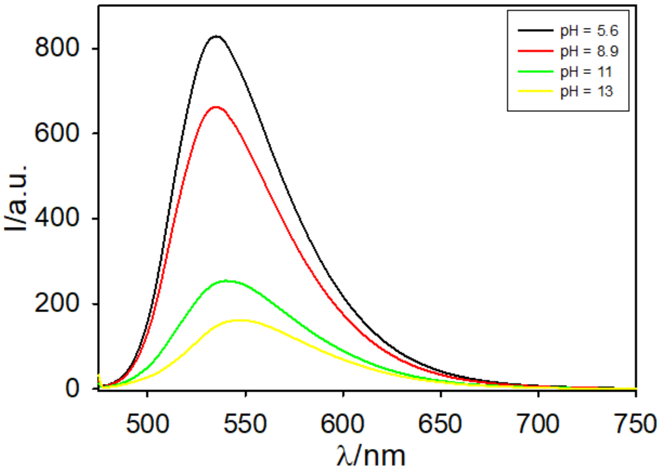

Figure 2.4 Fluorescence spectra of AO with λ_{exc}=470 nm in buffer solutions.

The AO titration was carried out starting from an acidic solution of AO ($1 \cdot 10^{-5}$ M) in water in the presence of buffers (acetate 10^{-3} M, phosphate 10^{-3} M, borate 10^{-3} M) by adding small amount of NaOH solution 1 M or 0.1 M and measuring the pH with a pH-meter. During the titration, absorption and fluorescence spectra were recorded: spectra obtained at selected pH are shown in figures 2.3 and figure 2.4, respectively. The absorbance and fluorescence at given wavelength are plotted in figure 2.5 and 2.6. Decreasing the pH below 6.0, the absorption spectrum does not show any variation since the protonation of the dye is complete. The corresponding absorption spectrum shows a maximum at 497 nm and can be attributed at the AH^+ species. In a similar way, the absorption spectrum at pH>12, having a maximum at 423 nm, can be attributed to the A species. The presence of an isosbestic point at 452 nm is observed during the pH titration as expected for the presence of only two absorbing species. Upon excitation at the isosbestic point, a quite strong emission with maximum at 536 nm is observed. The intensity of such emission is not pH dependent in this excitation condition, indicating that both A and AH^+ have similar fluorescence quantum yields and emission spectral shapes (although it is important to notice that the fluorescence maximum of AO is about 10 nm red-shifted with respect to AOH^+). This is confirmed by the excitation spectra (figure 2.7) with λ_{em}=530 nm recorded in acidic and alkaline conditions that match the absorption spectra of AH^+ and A respectively. On the contrary, the absorption spectrum of the AO solution at 488 nm or 514 nm is pH dependent, showing the variation plotted in figure 2.5.

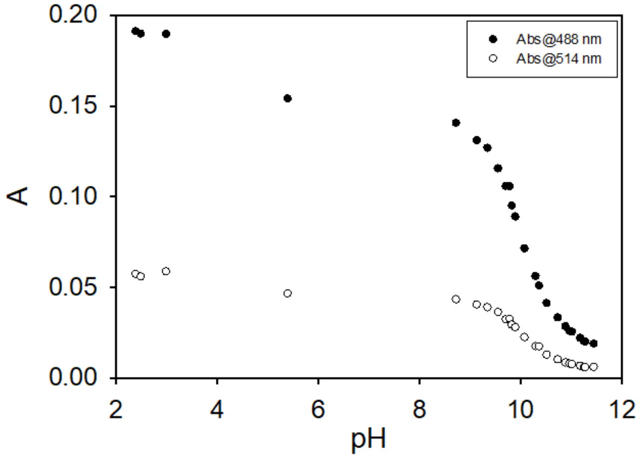

Figure 2.5 Comparison of AO absorbance at 488 nm 514 nm as a function of pH in water solutions.

Summarizing, in the alkaline form AO has a low molar absorption coefficient at λ = 488 nm. As a consequence, the population of its excited state is poorly efficient upon blue excitation, as previously explained. The protonated form (AH^+), on the contrary, strongly absorbs the excitation light; moreover, its pK_a in the silicate solution is about 10, which makes AO a suitable pH probe for detecting pH variations on the front of growth of biomorphs.

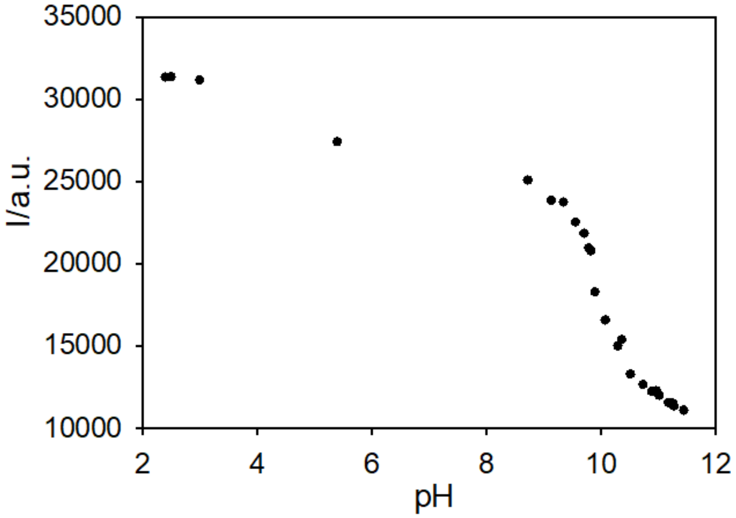

Figure 2.6 AO fluorescence at 530 nm as a function of pH in water solutions.

From non linear regression made on absorbance's data at 488 nm it has been found that:

$$K_a = (9.9 \cdot 10^{-11} \pm\ 6 \cdot 10^{-12})\ \mathrm{M},$$

while for the absorbance's data made at 514 nm:

$$K_a = (9.4 \cdot 10^{-11} \pm\ 6 \cdot 10^{-12})\ \mathrm{M}.$$

As consequence, K_a can be said to have a value about $9.9 \cdot 10^{-11}$ M.

This value is confirmed by emission spectra, for which λ_{exc} is 470 nm (figure 2.4), and its relative fitting curve as a function of pH observing it at

λ_{em} = 530 nm (figure 2.6), where the same equation used for absorption fitting has been used. In fact, K_a's value that has been found from it is:

$$K_a = (1.0 \cdot 10^{-10} \pm 1 \cdot 10^{-11})\ \mathrm{M}.$$

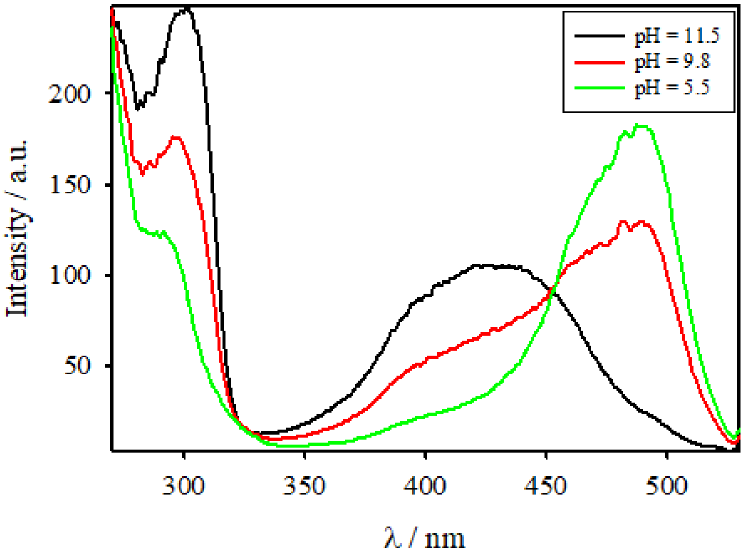

Figure 2.7 Excitation spectra with λ_{em}=530 nm at different pH in water solutions.

It is interesting to observe that the ratio between the peak at 497 and 423 nm in the absorption spectrum is strongly pH dependent and can be used to measure pH. Although light absorption measurements are not suitable for local pH detection, they are very convenient for bulk (or spatially averaged) analysis of homogeneous systems.

In view of the use of AO as a pH probe in silica gel, we first investigated the changes of the absorption properties of this dye in silicate during the gel formation. This was first done in optical cuvettes (1 cm optical path) by dissolving AO in a silicate solution, and adding increasing amounts of HCl.

As it can be seen in fig. 2.8, the absorption spectrum of AO in the alkaline silicate solution shows the typical peak at about 420 nm, identical to the one acquired in water for the neutral species. Upon addition of HCl, the raise of the typical band of the protonated AO can be detected at about 500 nm in the absorption spectrum confirming the response of the dye to protonation. The pH of the solution upon increasing addition of HCl was measured with a conventional pH-meter and the changes in the absorption spectra were analyzed as a function of the pH. This allowed us to conclude that the dependence of the absorption spectra from pH was the same observed in the absence of silicate and in particular that the **silicate did not affect significantly the pK$_a$ of AO**.

Upon addition of large amounts of HCl, jellification of the solution was observed in few minutes. Analyzing the absorption spectra of figure 2.8, we concluded that this fast jellification occurs, as expected, at pH about 10, as confirmed by pH-meter. It is important to notice that the absorption spectrum of AO, despite the increase of the baseline due to the scattering originated by the gel formation, is not affected by the jellification process. This experiment hence demonstrate that the **absorption spectra can be used to measure the bulk pH of the gel** using as reference the data acquired for AO in solution.

In the experiments described in the next chapters, the growth of the biomorphs is carried on in specific glass cassette filled with silica gel (these cassettes are made by two 100x50 mm^2 glasses which are separated by a 1 mm thick rubber spacer, and they are half filled with the gel; the actual size of the gel is 40x40x1 mm^3). In those systems the growth process is initiated by injecting a metal salt solution in the empty part of the cell.

In order to understand the behavior of our probe in these particular conditions, we investigated the photophysical properties of the AO containing gel inside the crystallization cassettes before the injection of the metal solution. Since in some cases (e.g. for the formation of calcium biomorphs) sodium carbonate will be added to the silicate before gel formation, we also investigated the effect of the presence of the carbonate on the photophysical properties of the fluorescent gel.

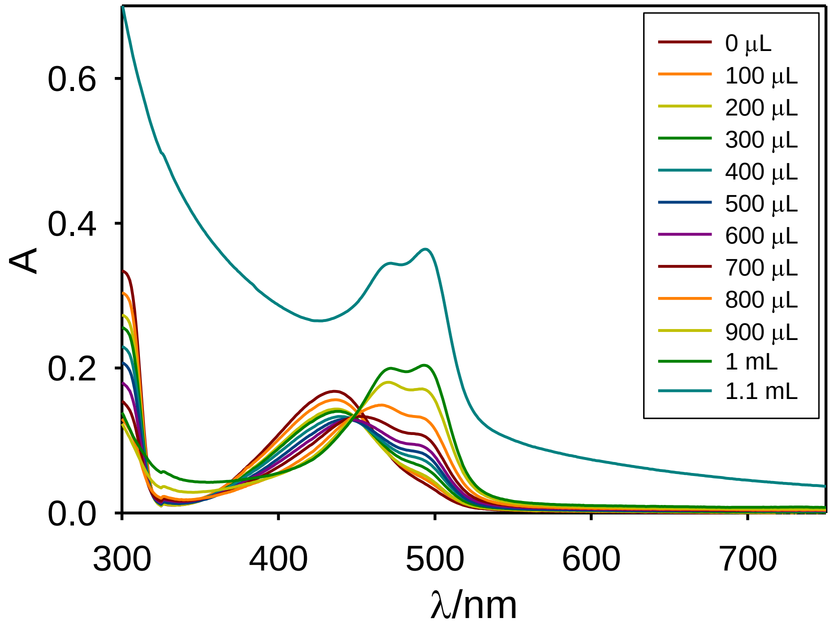

Figure 2.8 Absorption spectra of AO in 1:10=s.s.:H_2O solution (2.5 mL) adding different amount of HCl 1 M.

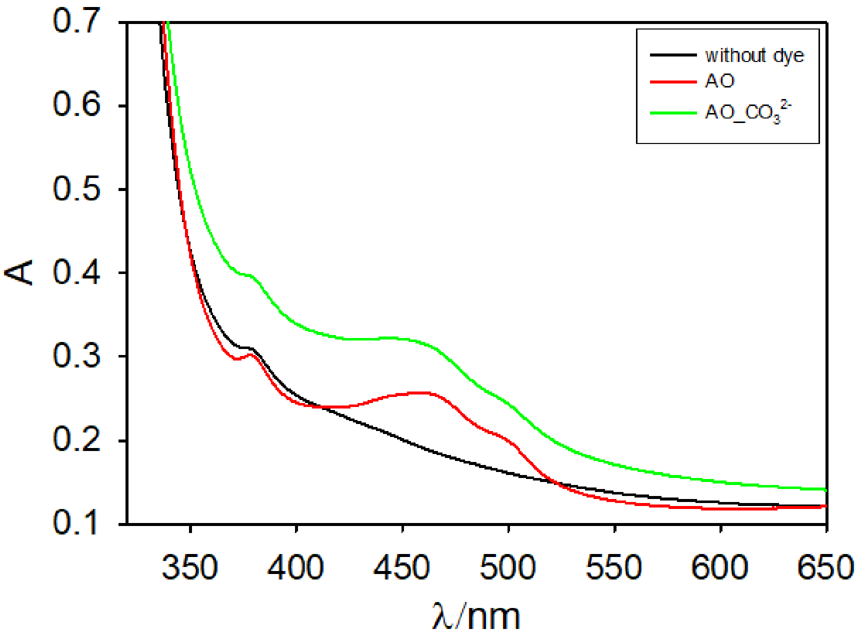

Figure 2.9 Absorption spectra of AO in gel inside the cassette with or without carbonate.

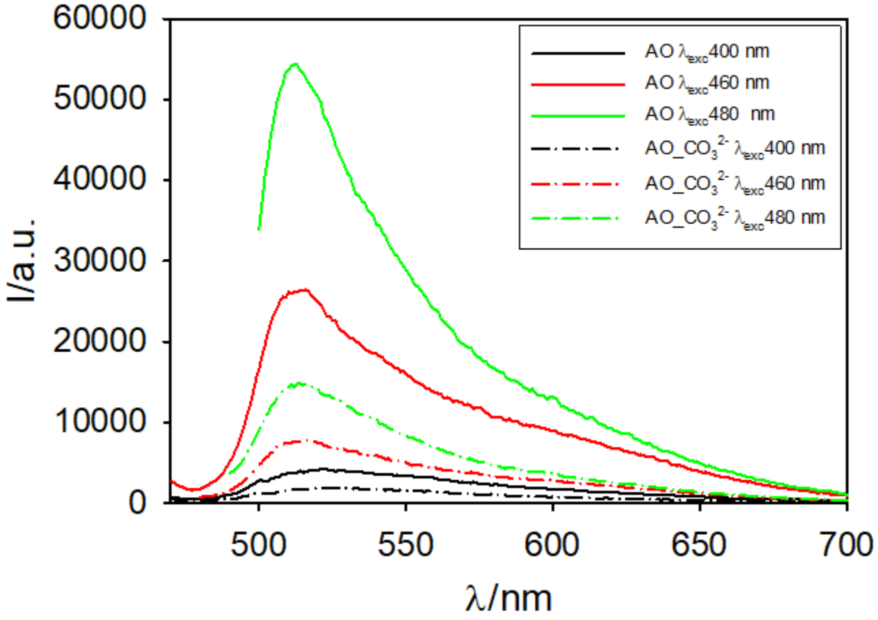

Figure 2.10 Emission spectra of AO in gel inside the cassette with or without carbonate at different excitation wavelengths.

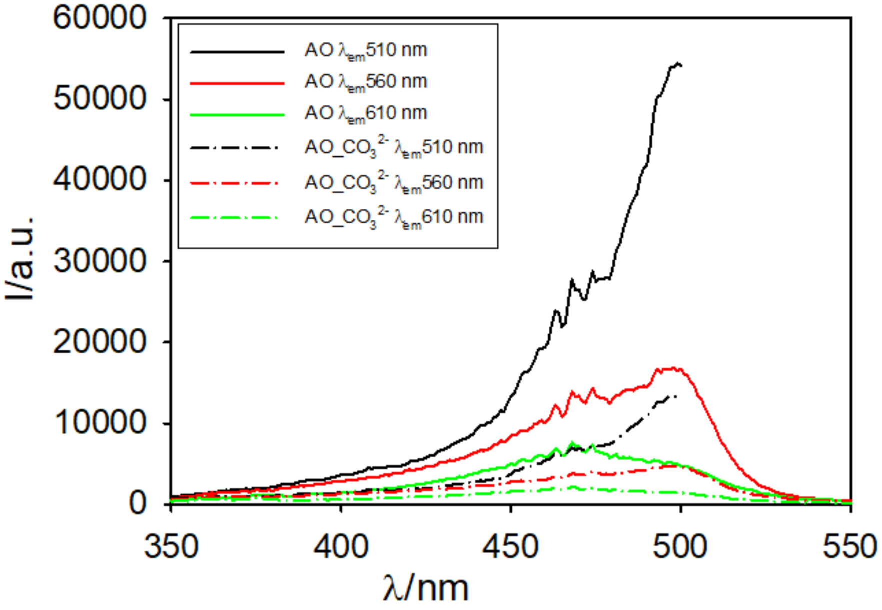

Figure 2.11 Excitation spectra of AO in gel inside the cassette with or without carbonate at different emission wavelengths.

The absorption spectra of two silica gel (either containing carbonate or not and both containing AO) are shown in figure 2.9. Despite the small difference in the baseline that indicates a slight different transparency, these spectra display the same absorption bands. The spectra present a band at about 450 nm which is the combination of the bands of the protonated and neutral AO in a ratio which is compatible with a pH of about 10.5. As previously mentioned we demonstrated that the dependence of the absorption of AO on pH is very similar in the gel and in water. Nevertheless, this consideration cannot be trivially extended to the fluorescence spectra, hence we investigated, experimentally, the fluorescence properties of AO in the gel directly in the crystallization cassette.

Fluorescence spectra were recorded in a conventional fluorimeter (Edinburgh) by positioning the gel at about 56° angle with respect to the excitation to minimize reflectance; the fluorescence was detected on the back-face with respect to the excitation (at 90° with respect to the excitation in a conventional L configuration). Fluorescence spectra at different excitation wavelengths are shown in figure 2.10: the emission band is quite broad and the band profile is quite independent on the excitation wavelength. In particular, the fluorescence spectra upon excitation at 460 nm 480 nm are very similar with a peak around 520 nm but the fluorescence intensity is, in the former case, about half than in the latter, despite the absorbance at 460 is higher than at 480 nm. Considering that at 480 nm excitation light is almost exclusively absorbed by AOH^+ while at 460 nm half by AOH^+ and half by AO, we can conclude that the fluorescence of AO is almost completely quenched in the gel. This is confirmed by the very weak fluorescence measured upon excitation at 400 nm where AO is preferentially excited. These conclusions are confirmed by the excitation spectra of the gel, shown in figure 2.11, that demonstrate that the dominating emitting species is AOH^+. Similar results were obtained in the presence of carbonate.

Further information about the properties of AO in the silica gel were obtained from the fluorescence anisotropy spectra (figure 2.12) and excited state lifetimes measurements.

Fluorescence anisotropy (r) is an indirect measurement of the rotational mobility of a fluorescent molecule, in particular a r=0.4 is typical of a completely immobilized molecule. Anisotropy values at about 520 nm as high as ~0.3 for sodium silicate-water solution and ~0.4 for sodium silicate-carbonate one clearly indicate that the AOH^+ molecules are immobilized in the gel. This was confirmed by the fluorescence anisotropy decay. It is worth noticing that at 650 nm, where the contribution to the fluorescence of the neutral AO form is higher, the fluorescence anisotropy is low, suggesting that this form is not adsorbed on the gel.

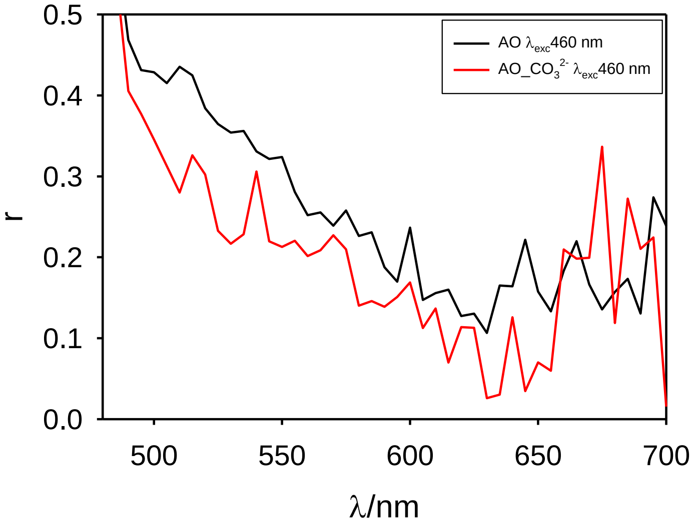

Figure 2.12 Anisotropy of AO in gel inside the cassette with or without carbonate.

Fluorescence decays were bi-exponentials and they were fitted with the following equation:

$$I(t) = A + B_1 e^{\left(-\frac{t}{\tau_1}\right)} + B_2 e^{\left(-\frac{t}{\tau_2}\right)}.$$

Fluorescence anisotropy decays were fitted with the equation:

$$r(t) = A + B_1 e^{\left(-\frac{t}{\tau_1}\right)}.$$

AO gel		
τ_1 = 3.5 ns; τ_2 = 6.40 ns		
	G = 1.508 (λ_{em} = 510 nm)	**G = 1.546 (λ_{em} = 520 nm)**
τ_{anis}	12.5816 ns	12.6891 ns
B	0.077	0.077
A	0.239	0.248

AO_CO_3^{2-} gel		
τ_1 = 3.79 ns; τ_2 = 7.90 ns		
	G = 1.305 (λ_{em} = 510 nm)	**G = 1.418 (λ_{em} = 520 nm)**
τ_{anis}	12.8152 ns	15.2551 ns
B	0.071	0.081
A	0.186	0.147

2.3.2 Photophysical properties of AY in solution and in gel

A second fluorescence pH probe suitable to investigate biomorphs is acridine yellow (AY), which is very similar to AO with a site that can be protonated as in the following scheme.

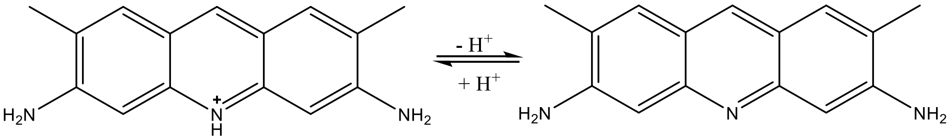

The molar absorption coefficient of AY is 3.9x10^4 M^{-1}cm^{-1} at 461 nm and the fluorescence QY is 0.47. The most relevant difference with respect to AO is that AY has a pK$_a$≈8.9 and it can be used to measure lower pH with respect to AO.

In order to investigate the pH dependence of the photophysical properties, a titration experiment was carried out starting from a AY solution, with a concentration of $1 \cdot 10^{-5}$ M in water in the presence of buffers (acetate 10^{-3} M, phosphate 10^{-3} M, borate 10^{-3} M) adding small amounts of NaOH solution 1 M or 0.1 M and measuring the pH with a pH-meter. During the titration, absorption and fluorescence spectra were recorded as shown in figures 2.13 and figure 2.14, respectively. Decreasing the pH below 8.0, the absorption spectra do not show any important variations since the protonation of the dye is complete. The corresponding absorption spectra show a maximum at 440 nm and can be attributed to the protonated species. On the other hand, the absorption spectrum at pH>11 shows a maximum at 400 nm that can be attributed at the deprotonated species.

Upon excitation at 440 nm, a quite strong emission with maximum at 510 nm is observed. The intensity of such emission is pH dependent, showing the variation plotted in figure 2.14.

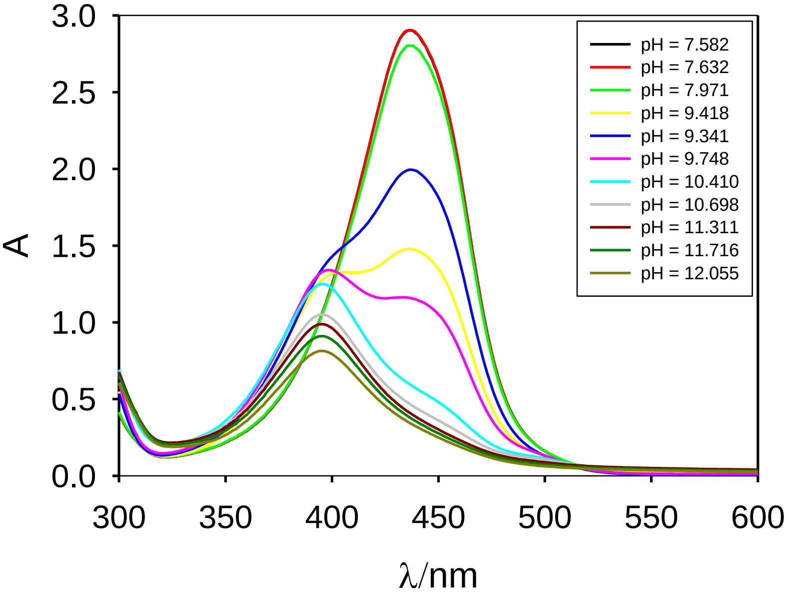

Figure 2.13 Absorbance spectra of AY as a function of pH in buffer solutions.

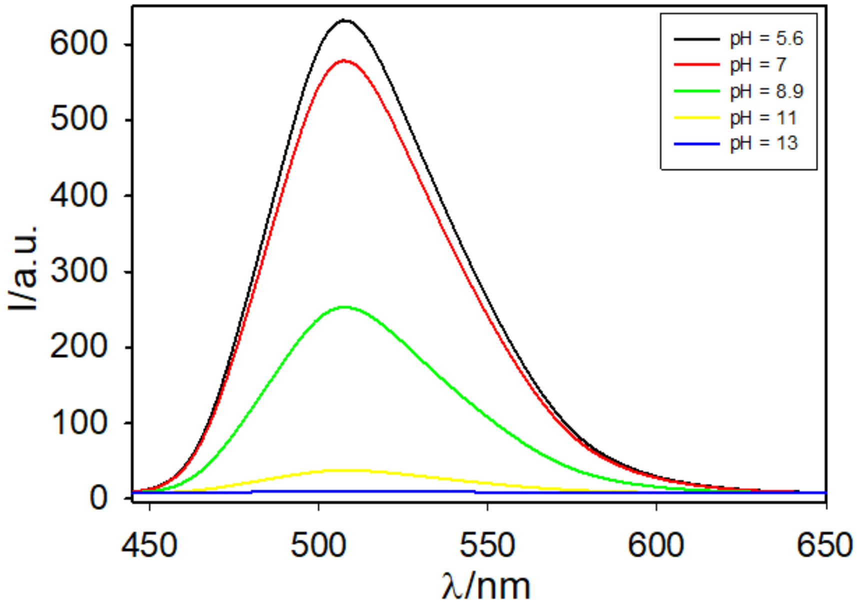

Figure 2.14 Fluorescence spectra of AY with λ_{exc}=440 nm in buffer solutions.

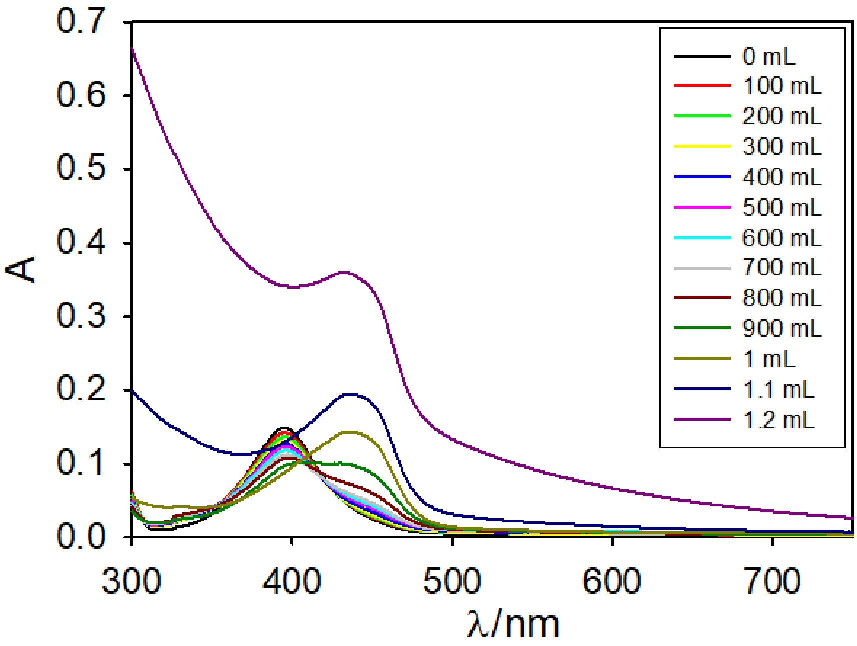

Figure 2.15 Absorption spectra of AY in 1:10=s.s.:H_2O solution adding different amount of HCl 1 M.

As for AO, with the aim of using AY as a suitable pH probe in silica gel, we first investigated the changes of the absorption properties of this dye in silicate during the gel formation. This was first done in optical cuvettes (1 cm optical path) by dissolving AY in a silicate solution, and adding increasing amount of HCl.

As it can be seen in fig. 2.15, the absorption spectrum of AO in the alkaline silicate solution shows the typical peak at about 400 nm, identical to the one acquired in water for the neutral species. Upon addition of HCl the raise of the typical band of the protonated AY can be detected at about 450 nm in the absorption spectrum confirming the response of the dye to protonation. The pH of the solution upon increasing addition of HCl was measured with a conventional pH-meter and the changes in the absorption spectra were analyzed as a function of the pH. This allowed us to conclude that the dependence of the absorption spectra from pH was the same observed in the absence of silicate and in particular that the **silicate did not affect significantly the pK_a of AY**.

Upon addition of large amounts of HCl, jellification of the solution was observed in few minutes. Analyzing the absorption spectra of figure 2.15, we concluded that this fast jellification occurs, as expected, at pH about 10, as confirmed by pH-meter. It is important to notice that the absorption spectrum of AY, despite the increase of the baseline due to the scattering originated by the gel formation, is not affected by the jellification process. This experiment hence demonstrate that the **absorption spectra can be used to measure the bulk pH of the gel** using as reference the data acquired for AY in solution.

As for AO, we investigated the photophysical properties of the AY contained in the gel (in the presence or absence of carbonate) inside the crystallization cassettes before the injection of the metal solution.

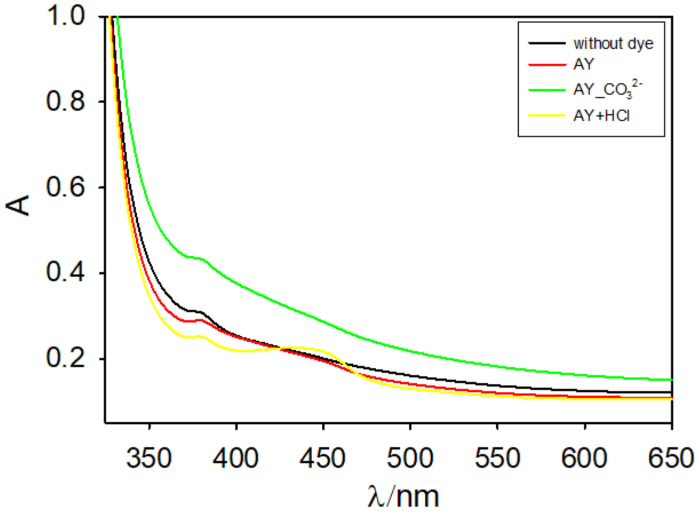

Figure 2.16 Absorption spectra of AY in gel inside the cassette with or without carbonate or pouring HCl 1M on the top of the gel without carbonate.

The absorption spectra of two silica gels (either containing carbonate or not and both containing AY) are shown in figure 2.16. After spectral deconvolution, necessary in this case to eliminate the contribution due to the scattering of the gel, the spectra present a band at about 400 nm which can be attributed to the neutral AY, which is the dominating species at the pH of about 10.5 of the gel. In order to test the responsivity of the gel to pH changes we injected a solution of HCl 0.1M on the top of the gel and we acquired the absorption spectrum after two days in order to allow the diffusion of the acid into the gel. The resulting spectrum, shown in fig. 2.16, clearly demonstrates the protonation of AY.

Fluorescence spectra at different excitation wavelengths are shown in figure 2.17: a defined emission peak at about 500 nm can be detected upon excitation of the gel at 400 nm while, on the contrary, only a background noise due to excitation scattering is acquired upon excitation at 460 nm. This demonstrated that, as expected because of the pK_a, AY is almost completely non protonated in the gel, that has a bulk pH of about 10.6. When the pH is decreased by adding HCl, on the other hand, fluorescence at 500 nm upon excitation at 460 nm can be clearly detected, being in this case more intense than upon excitation at 400 nm.

This demonstrates that AY is protonated and that, differently form AO, both AY and AYH^+ are fluorescent and present similar QY in the gel.

These conclusions are confirmed by the excitation spectra of the gel, shown in figure 2.18, that demonstrate that in the gel fluorescence is mostly due to neutral AY (excitation peak at 400 nm), while after addition of HCl the excitation peak of AYH^+ at 460 nm can be observed. Similar results were obtained in the presence of carbonate.

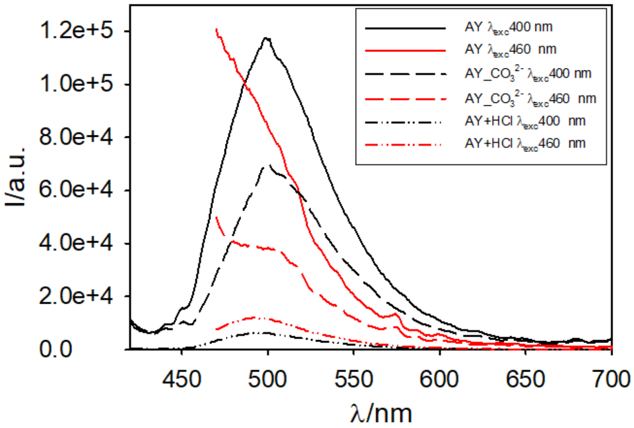

Figure 2.17 Emission spectra of AY in gel inside the cassette with or without carbonate or pouring HCl 1M on the top of the gel without carbonate at different excitation wavelengths.

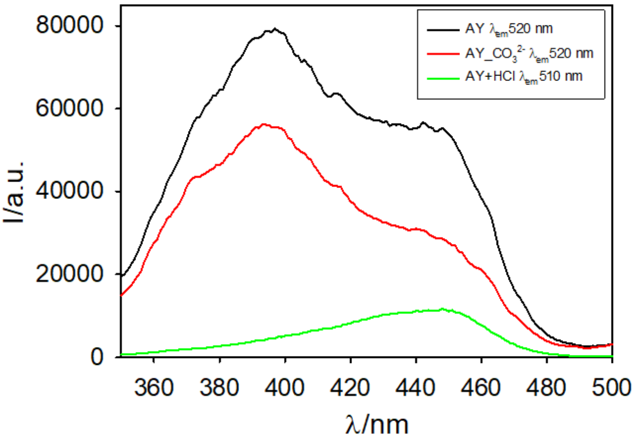

Figure 2.18 Excitation spectra of AY in gel inside the cassette with or without carbonate or pouring HCl 1M on the top of the gel.

Further information about the properties of AY in the silica gel were obtained from the fluorescence anisotropy spectra (fig. 2.19) and excited state lifetimes measurements.

Anisotropy values at about 520 nm as high as ~0.4 measured for the gel after penetration of HCl and formation of AYH^+ demonstrate that these cationic molecules are immobilized in the gel. On the contrary, AY shows a low anisotropy which suggests this molecule is not adsorbed on the gel. This was confirmed by the fluorescence anisotropy decay.

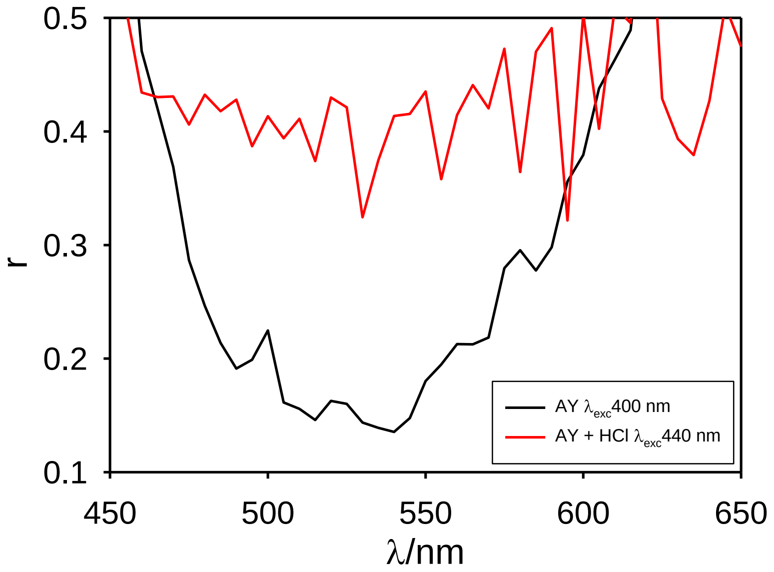

Figure 2.19 Anisotropy of AY in gel inside the cassette with or without pouring HCl on the top of the gel.

AY gel		
τ_1 = 1.07 ns; τ_2 = 5.45 ns		
	G = 1.510 (λ_{em} = 500 nm)	**G = 1.546 (λ_{em} = 520 nm)**
τ_{anis}	0.1703 ns	0.1714
B	0.013	0.013
A	0.141	0.149

AY_HCl gel		
τ_1 = 4.74 ns; τ_2 = 4.16 ns		
	G = 1.305 (λ_{em} = 495 nm)	**G = 1.418 (λ_{em} = 510 nm)**
τ_{anis}	16.8756 ns	17.9199
B	0.026	0.027
A	0.356	0.375

2.3.3 Comparison of AO and AY as pH probes for gel measurements

In conclusion, both AO and AY promise to be suitable for mapping pH in the silica gel. The two probes differ first of all for the pK_a (10.0 for AO and 8.9 for AY) which is, in the gel, very similar to the one measured in water solution. As far as AO is concerned, the spectra response to pH is very different with respect to water upon excitation at 400 nm, since the fluorescence of the neutral AO is much weaker in the gel than in water. This signal is, in any case, detectable and usable for ratiometric sensing. The fluorescence response to pH of AO at excitation at 480 nm is, on the other hand, very similar to the one observed in water.

In the case of AY, the neutral species AY are not quenched in the gel and the response to the pH of this probe is in the gel very similar to the one shown in water. Both for AY and AO, fluorescence anisotropy measurements demonstrate that the cationic forms present very hindered rotational mobility in the gel.

As a main advantage AY shows very weak fluorescence upon 460 nm excitation in the gel at the initial bulk pH, while a large increase is observed upon protonation. This indicates that AY fluorescence gives a huge response to pH decrease in the silica gel which is the most important requirement in the pH mapping experiments. Hence **AY will be used as probe for biomorphs investigation**.

2.3.4 Photophysical properties of HTPS in solution

Part of this thesis is dedicated to the investigation of pH in silica gardens and more in detail to detect pH changes in the metal solution contained inside the hollow tubes during and after tubes formation, because of diffusion through the membrane. In this case the solution is acid, and an increase of the pH is expected because of the possible diffusion of OH^- ion from the alkaline external silica solution. Hence, we preferred to focus on probes that showed weak fluorescence in the acidic form and bright fluorescence upon pH increase (hence and ON/OFF response to protonation: the opposite behavior with respect to AO and AY). Moreover, considered that the metal solutions show a pH<<7.0, a probe with a pK_a around 7.0 is expected to be suitable to observe increase of pH inside the tubes.

The pH probe 8-hydroxypyrene-1,3,6-trisulfonic acid (HPTS) shows the desired ON/OFF response to protonation and a $pK_a \approx 7.3$:

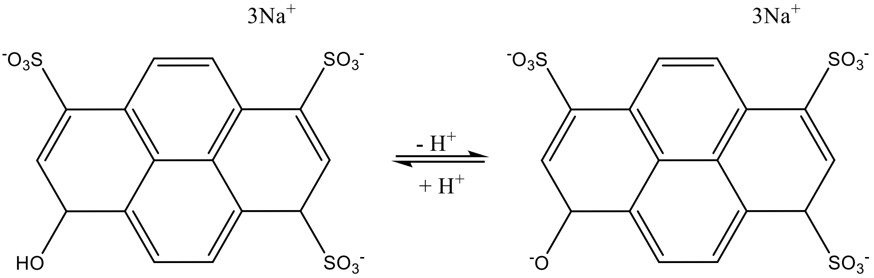

We studied HPTS photophysical properties as a function of pH starting from an acidic solution of the dye ($1 \cdot 10^{-5}$ M) in water in the presence of buffers (acetate 10^{-3} M, phosphate 10^{-3} M, borate 10^{-3} M) by adding small amount of NaOH solution 1 M or 0.1 M and measuring the pH with a pH-meter. During this titration experiment, absorption and fluorescence spectra were recorded: some selected spectra are shown in figures 2.20 and 2.21 – 2.22, respectively. Contrary to the behavior of AO and AY dyes, decreasing the pH below 6.0, the absorption spectrum does not produce any variation since the protonation of the dye is complete. The corresponding absorption spectrum shows a maximum at 375 nm that can be attributed to the protonated species. In a similar way, the absorption spectrum at pH>9.0, having a maximum at 440 nm, can be attributed to the deprotonated species. The presence of an isosbestic point at 420 nm is observed during the pH titration as expected for the presence of only two absorbing species.

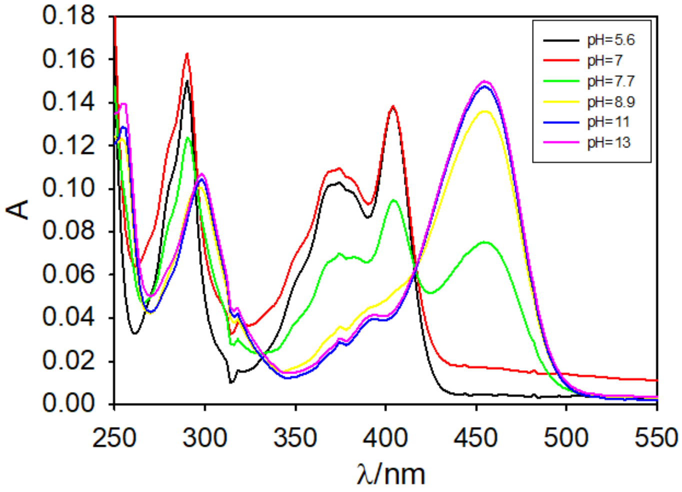

Figure 2.20 Absorbance spectra of HPTS as a function of pH in buffer solutions.

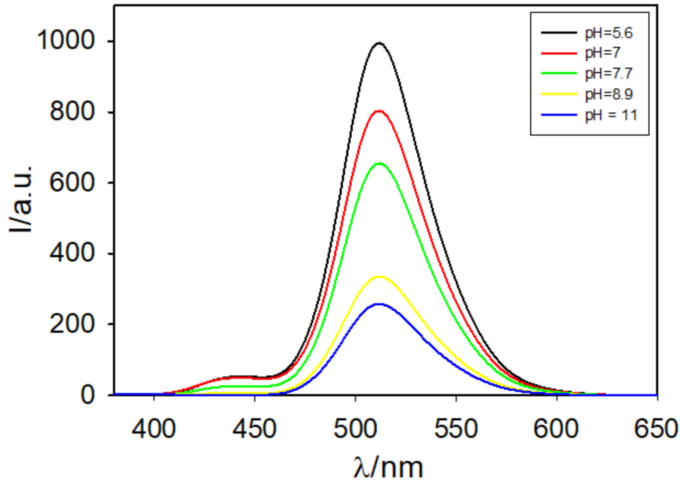

Figure 2.21 HPTS titration emission at λ_{exc}=375 nm as a function of pH in buffer solutions.

Upon excitation at 375 nm, a quite strong emission with maximum at 510 nm is observed. The intensity of such emission is pH dependent, showing the variation plotted in figure 2.21.

As it can be seen, increasing the pH there is a decrease of the fluorescence intensity.

On the other hand, upon excitation at 440 nm, a quite strong pH dependent emission with maximum also in this case at 510 nm is observed, but the intensity increases with the increase of the pH, as plotted in figure 2.22.

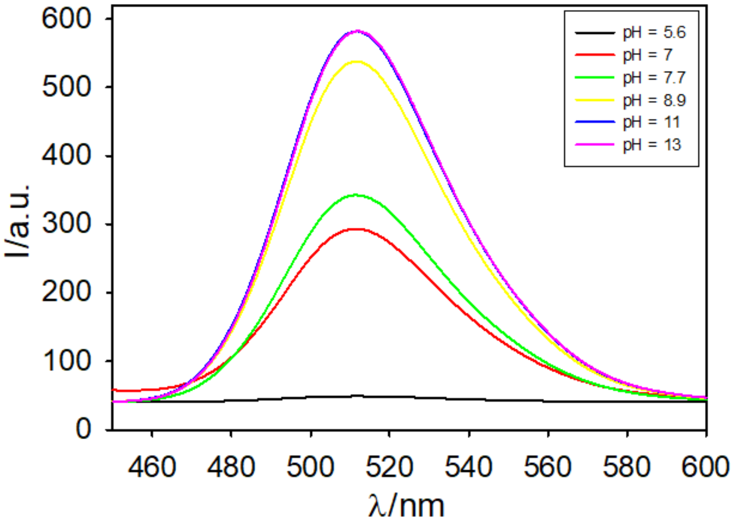

Figure 2.22 HPTS titration emission at λ_{exc}=440 nm as a function of pH in buffer solutions.

The lifetimes of HPTS are reported in chapter 6.4.1, where I needed them to explain the behavior of silica gardens growth.

We would like to stress that HPTS is a well known strong photoacid, so that in the excited state $pK_a^* < pK_a$. Because of this, the relationship between fluorescence and pH does not follow the simple equilibrium equations, since the excited state reaction alters the emission. Nevertheless, the experimental results showed that the fluorescence response can be fitted with a simplified model with an apparent pK_a. This simplified approach was followed in this work.

2.4 Conversion of fluorescence into pH

In order to correlate fluorescence intensity with the pH, we use the ImageJ software for images analysis. In particular, we wrote a specific macro based on the equilibrium reaction of the protonated and the deprotonated molecules of the dyes:

$$AH^{+} + H_2O \rightleftarrows H_3O^{+} + A.$$

It is easy to find that:

$$k_a = \frac{[H_3O^{+}][A]}{[AH^{+}]}$$

$$k_a = \frac{[H_3O^{+}][A]}{C_{AH} - [A]},$$

considering that

$$c = [HA^{+}] + [A] = \text{costant}.$$

Then, the consequent math is the following:

$$[H_3O^{+}] = K_a \frac{C_{AH^{+}} - [A]}{[A]}$$

$$[H_3O^{+}] = K_a \left(\frac{1}{\chi_A} - 1\right),$$

where χ_A is the molar fraction of the A molecules.
Considering then the equation reported in section 2.1:

$$I = (I_2 - I_1)\chi_A + I_1$$

and replacing it with $\chi_A = \frac{[A]}{c}$:

$$I = I_1 \frac{[AH^+]}{c} + I_2 \frac{[A]}{c},$$

which can be wrote like this

$$I = I_{ac}\chi_{AH^+} + I_{alk}\chi_A.$$

Continuing the equations:

$$I = I_{ac}(1 - \chi_A) + I_{alk}\chi_A$$

$$I = I_{ac} + (I_{alk} - I_{ac})\chi_A$$

$$\chi_A = \frac{I - I_{ac}}{I_{alk} - I_{ac}}$$

and then substituting this value of χ_A into the previous expression it is

$$[H_3O^+] = k_a\left(\frac{I_{alk} - I_{ac}}{I - I_{ac}} - 1\right).$$

At this point, it is simple to transform $[H_3O^+]$ into pH:

$$pH = pk_a - \log\left(\frac{I_{alk} - I_{ac}}{I - I_{ac}} - 1\right)$$

$$pH = pk_a - \log\left(\frac{I_{alk} - I}{I - I_{ac}}\right);$$

considering that we called previously I_{alk} as I_2 and I_{ac} as I_1, the overhead equation turns into the following one:

$$pH = pk_a - \log\left(\frac{I_2 - I}{I - I_1}\right).$$

This expression was used to write a macro for the ImageJ software in order to convert intensity profiles into pH maps.

It is important to stress that if the total concentration of the two species AH^+ and A is not constant, the calculated pH deviates from the one obtained with this macro.

Once these equations are imported inside the ImageJ software as a macro and once this macro is run over the selected fluorescence intensity images, the result obtained gives in false colors the pH map of the images (example reported in the following figure).

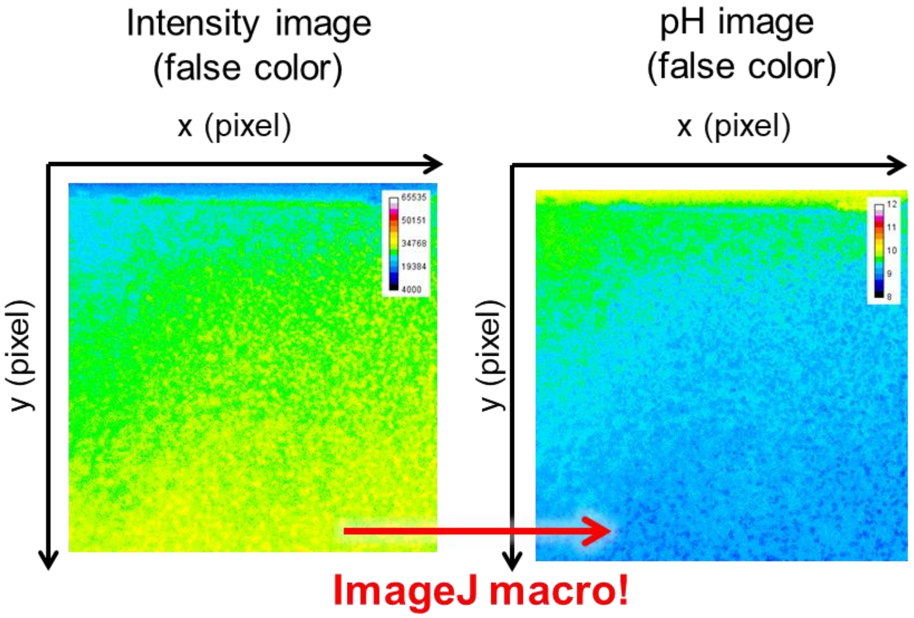

Figure 2.23 One frame from a real time film of calcium gel-grown biomorphs in false colors reproducing the intensities (left) and the corresponding pH values (right) after the application of the ImageJ macro.

2.5 Ratiometric detection of pH

Ratiometric spectroscopic method requires fluorescent sensors that are differentially sensitive to the analyte (i.e., protons for pH probes) for at least two excitation or emission wavelengths.[15],[16] Emission at one carefully chosen wavelength may be enhanced or diminished relative to the emission at another one. Ratios between these signals then can be calibrated to indicate pH values. Several advantages characterize ratiometric detection: parameters such as optical path length, local probe concentration and photobleaching can be corrected.[10]

With the purpose to apply a ratiometric detection over the acquired fluorescence images, two different excitations were used and two different emission frames are acquired. Obviously, the fluorescent probe must be excitable at two different wavelengths. In the simplest case, ratiometric response can be achieved when the pH probe at one excitation wavelength gives a strongly pH dependent (originating the signal image I_1), while at another excitation wavelength it shows a pH independent fluorescence (the reference image I_2). More in general, as mentioned, ratiometric detection is possible when I_1 and I_1 show a different pH dependence by using the ratio $R = \frac{I_1}{I_2}$ for calculating the pH. Also in this case we developed a suitable ImageJ macro that converted this ratio intensity R into a more reliable pH map, using the same equation reported before:

$$pH = pk_a - log\left(\frac{R_2 - R}{R - R_1}\right),$$

where R_1 and R_2 are the ratiometric values obtained at pH_1 and pH_2, where $pH_2 \gg pk_a$ and $pH_1 \ll pk_a$.

If we want to plot the ratiometric signal as a function of pH, we have to rewrite this formula, and the resulting equation is:

$$R = \frac{R_2 + R_1(10^{pK_a - pH})}{10^{pK_a - pH} + 1}.$$

The following figure shows the calibration plot, obtained with the previous equation, used for the AY dye which we used the ratiometric detection with:

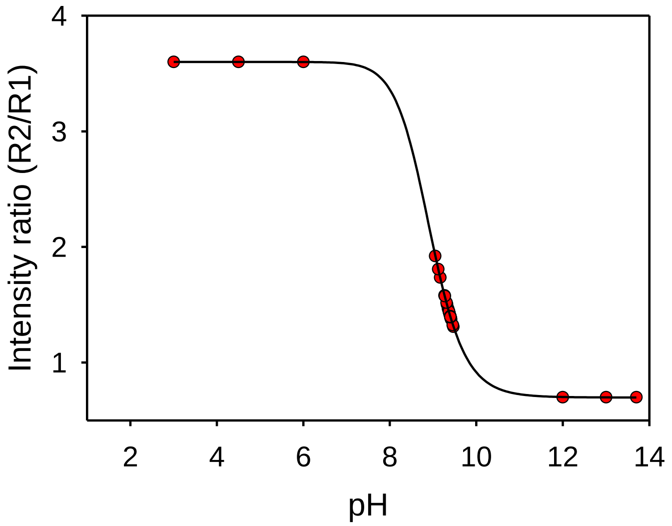

Figure 2.24 The calibration plot of AY dye used for the ratiometric detection.

Here is shown how the ratiometric detection and the conversion into pH work, using as example a frame collected during a Ca-biomorphs growth inside the gel filled with AY dye:

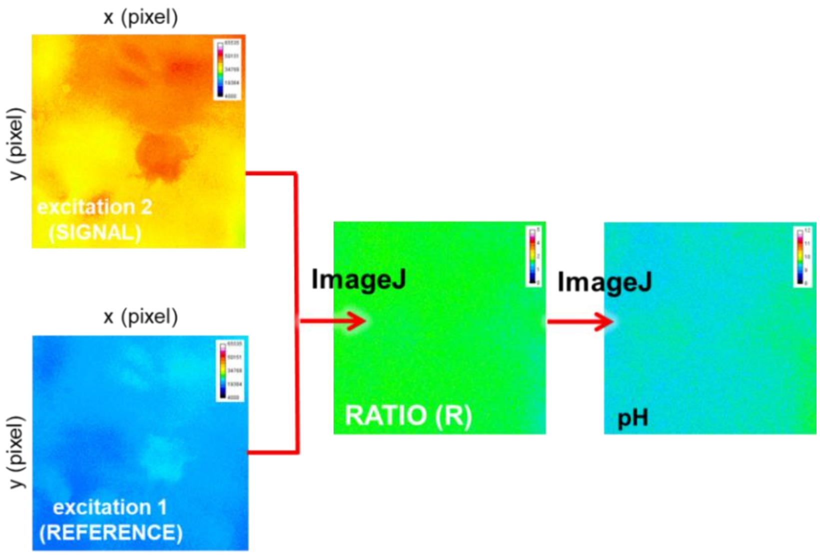

Figure 2.25 An example of how the ratiometric detection works: the ratio R is obtained dividing the signal intensity values by the reference ones. Then, this ratiometric intensity values can be used to obtain a more accurate pH map.

2 References

[1] H. R. Kermis, Y. Kostov, P. Harms, G. Rao, *Biotechnology Progress* **2002**, *18*, 1047-1053.

[2] A. W. Czarnik, America Chemical Society, Washington, DC, USA, **1993**.

[3] *Topics in fluorescence spectroscopy, Probe Design and Chemical Sensing*, Plenum Press, New York, USA, **1994**.

[4] L. Fabbrizzi, A. Poggi, *Chemical Society Reviews* **1995**, *24*, 197-202.

[5] J. P. Desvergne, A. W. Czarnik, Kluwer, Dordrecht, The Netherlands, **1997**.

[6] S. A. De Silva, K. C. Loo, B. Amorelli, S. L. Pathirana, M. Nyakirang'ani, M. Dharmasena, S. Demarais, B. Dorcley, P. Pullay, Y. A. Salih, *J Mater Chem* **2005**, *15*, 2791-2795.

[7] M. R. S. Fuhr, L. W. Burgess, T. Hirschfeld, G. D. Chrisstian, in *Analyst, Vol. 112*, Cambridge, UK, **1987**, p. 1159.

[8] J. B. Pawley, *Handbook of Biological Confocal Microscopy*, Springer LLC, New York, USA, **2006**.

[9] R. G. Haugland, *Handbook of Fluorescent Probes and Research Products*, Molecular Probes Inc., Eugene, OR, USA, **2002**.

[10] R. Wang, C. W. Yu, F. B. A. Yu, L. X. Chen, *Trac-Trend Anal Chem* **2010**, *29*, 1004-1013.

[11] H. Szmacinski, J. R. Lakowicz, *Anal Chem* **1993**, *65*, 1668-1674.

[12] J. Y. Han, K. Burgess, *Chem Rev* **2010**, *110*, 2709-2728.

[13] L. Moggi, A. Juris, T. Gandolfi, *Manuale del fotochimico*, **2006**.

[14] D. Wencel, T. Abel, C. McDonagh, *Anal Chem* **2014**, *86*, 15-29.

[15] R. Bright, G. W. FIsher, J. Rogowska, *The Journal of Cell Biology* **1987**, *104*, 1019-1033.

[16] N. O'Connor, R. B. Silver, *Methods in Cell Biology* **2007**, *81*, 415-433.

3 Experimental equipment

3.1 Absorption and fluorescence spectroscopy

3.1.1 Absorption

Molecules can be excited if some peculiar “perturbations” with an exact quantity of energy excite them. This quantity of energy should be exactly the energetic difference between the ground and the excited state: in this case, the energy can be absorbed by the molecule and the excited state is formed. The electronic transitions require energies with typical frequencies of UV-VIS light. These absorbed energies generate the absorption spectra.[1]

For the spectroscopic analysis, a spectrophotometer was used: in particular, a PerkinElmer Lambda 25 UV–VIS spectrophotometer (figure 3.1a).

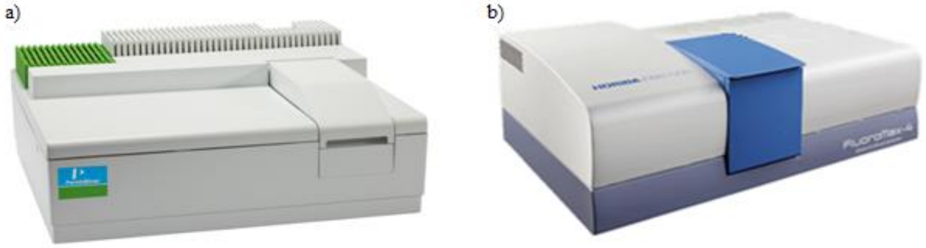

Figure 3.1 a) Spectrophotometer. b) Spectrofluorometer.

The solutions were housed in quartz cuvette for measurements with optical path length of 1 cm.

3.1.2 Fluorescence

Fluorescence spectroscopy is a technique that uses radiative deactivation of an excited molecule, following the selection rules. For this reason, the fluorescence transitions can happen very fast (10^{-9} – 10^{-6} s). The emission is extremely sensitive to impurities that can originate bimolecular processes of deactivation that compete with emission: this process is called quenching.[1]

A FluoroMax-4 (HORIBA) spectrofluorimeter (figure 3.1b) was used. And also in this case the solutions were housed in quartz cuvette for measurements with optical path length of 1 cm.

3.1.3 Single photon counting

As told before, luminescence can be characterized by the energy profile emission, but also by its lifetime (τ), namely the temporal characteristics of the emission measuring its intensity as a function of time.

The lifetime of an excited state that decades to the ground state can be calculated by its concentration as a function of time. The majority of methodologies that allow to calculate the lifetime of an excited state are named *time domain measurements* because of this.

The technique known as time correlated single photon counting is based on the probability that a single photon emitted by an excited state of a molecule could be detected by a highly sensitive photomultiplier, in a temporal range from hundreds of ps to tens of ms.[2]

For our measurements, a FLS900 Edinburgh time resolved fluorescence spectrometer was used:

Figure 3.2 Single photon counting instrument.

3.1.4 Steady state and time resolved fluorescence anisotropy

Fluorescence anisotropy measurements are mostly used in order to study the dynamic of rotation of a fluorophore in space and the energy transfer from an excited fluorophore to its ground state. The constant rate and the degrees of freedom are strongly dependent on the properties of the fluorophore, such as the mass and the structure, and of the surrounding environment. Fluorescence anisotropy measure the degree of polaritation of the fluorescence coming from a molecule excited with polarized light.

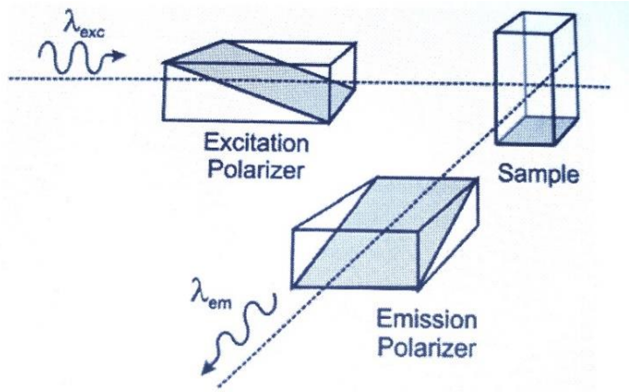

Figure 3.3 Schematic representation of how fluorescence anisotropy works.[2]

Interposing the excitation polarizer between the excitation source and the sample holder, as it is shown in figure 3.3, a vertical polarized light is obtained and the sample is excited. The emission polarizer analyzes the fluorescence, and the fluorescence anisotropy is calculated from the intensities as following:

$$r = \frac{I_{||} - I_{\perp}}{I_{||} + 2I_{\perp}}$$

where $I_{||}$ is the intensity measured when the emission polarizer is vertical, namely parallel to the excitation one, while $I_{\perp}$ is the intensity measured when the emission polarizer is horizontal, namely perpendicular to the excitation one.

Each electronic transition is associated to a transition moment, a vector that is the origin of the polarized electronic transition of the molecule and that has a specific orientation regarding to the molecule structure. Generally speaking, when the deactivation of an excited state happens in a radiative way, the emitted photon is polarized in parallel to the transition moment.

It is possible to measure the angle between the transition moment associated to whatever absorption transition and the one associated to the emission transition:

$$r_0 = \frac{2}{5}\left(\frac{3\cos^2\beta - 1}{2}\right)$$

where $r_0$is named *fundamental anisotropy*, that is the anisotropy in absence of rotation.

It has to be noted that if $r_0$is 0.4 it means that there is a perfect parallelism between the absorption transition and the emission one; while if $r_0$is -0.2 it means that between them there is a perfect perpendicularity.

Molecules are free to diffuse and rotate into space: this means that, even if they can be polarisingly excited, they can be strongly affected on their emission polarity. Between the excitation and the emission, molecules can reorientate themselves due to Brownian motion. This leads to a general non-polarized emission light; a phenomenon called *depolarization*, that exists just if the reorientation happens with a velocity equal or faster than τ. This reorientation time is called *rotational correlation time*:

$$\frac{r_0}{r} = 1 + \frac{\tau}{\theta} = 1 + 6D\tau$$

where D is rotational diffusion coefficient.

Another important cause that leads to depolarization is the energy transfer between similar fluorophores.

Actually, the response of the instrument is not independent from the polarized light: this means that the measured angle is different with the same intensity of the vertical (V) and the horizontal (H) components. In order to avoid this problem, there is a correction factor dependent on the used instrument and the emission wavelength: the G factor.

$$r = \frac{I_{VV} - GI_{VH}}{I_{VV} + 2GI_{VH}}$$

$$G = \frac{I_{HV}}{I_{HH}}$$

This G factor is purely experimental that has to be determined for each wavelength.

Until now, all the done considerations have been connected to anisotropy measurements in stationary state. It is possible to study time resolved fluorescence anisotropy: this kind of measurement is useful when the depolarization processes are faster than τ, that means that the majority of the emitted light is not polarized. Using pulsed light techniques, instead, it is possible to acquire anisotropy of these molecules with very fast depolarization. However, in this case, r_0 does not match perfectly with the anisotropy at time zero because in general the depolarization processes are faster than the pulse duration used for the excitation: this means that r_0 has a mean value over the entire impulse duration.

The equation reported above to determine the anisotropy (r) is the same for time resolved anisotropy, but it is important to notice that, in order to obtain two compatible decays, it is fundamental to use the same acquisition time. Moreover, the interpolation of the fluorescence anisotropy decays can be done using the following equation:

$$r(t) = r_0 e^{-t/\theta}.$$

However, this approach does not permit the deconvolution from excitation pulse.[2]

3.2 Wide field fluorescence microscopy

In order to study the crystals, a fluorophore that allows to follow their growth was required. Two types of microscopes were used to investigate the behavior of these structures: wide field and confocal fluorescence microscopes.

In this section wide field fluorescence microscope is going to be discussed. It allows to collect a high number of frames per minutes in low power excitation conditions and hence to follow the process with adequate temporal resolution for hours without severe effect of photobleaching. The main drawback of this technique is that it does not allow to cut out the fluorescence coming from the layers of the system out of focus which, especially in thick samples, origin a strong background. Nevertheless, by properly choosing the pH sensitive fluorophore, the signal arising from the bulk can be minimized and hence the effect of the background fluorescence too.

3.2.1 The basic set up

The basic task of the fluorescence microscope is to irradiate the specimen with the desired wavelength and then to separate the much weaker emitted light (fluorescence) from the excitation light. Only the emission light should reach the eye or other detector so that the fluorescent areas are contrasted against a dark background. The detection limit is largely determined by the darkness of the background. The excitation light is typically 10^5 or 10^6 times brighter than the emitted light.[3]

In our case the specimen is illuminated by a xenon lamp beam which is focused on the back focus of the microscope objective by a lens of 50 mm focal length. In order to obtain a ratiometric detection (see chapter 2.5), two kinds of excitation filters were used: 445/45 nm (that gives the signal fluorescence images) and 390/18 nm (that gives the reference intensities).

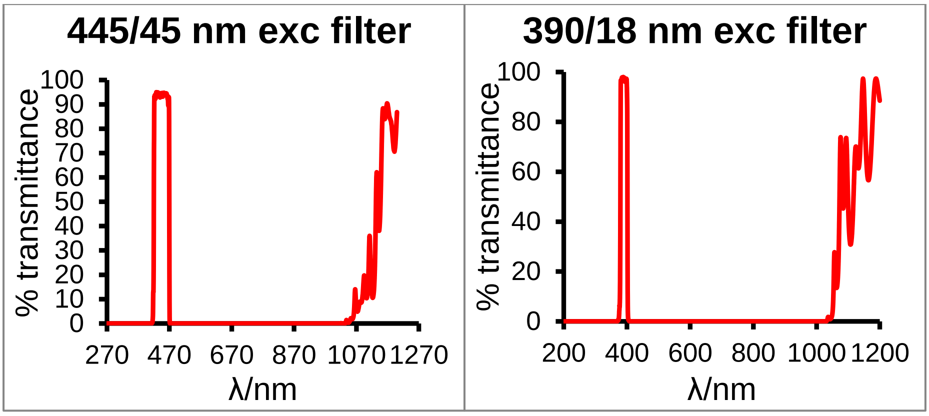

Figure 3.4 Spectra of the two different excitation filters by Thorlabs® used to obtain ratiometric detection.

The light coming from the lamp passes through the excitation filter where there is the selection of the excitation wavelength light (excitation filters wheel) and the blockage of undesired wavelengths (attenuator filters wheel, which could have filters of transmittance between 50% and 0.01%).

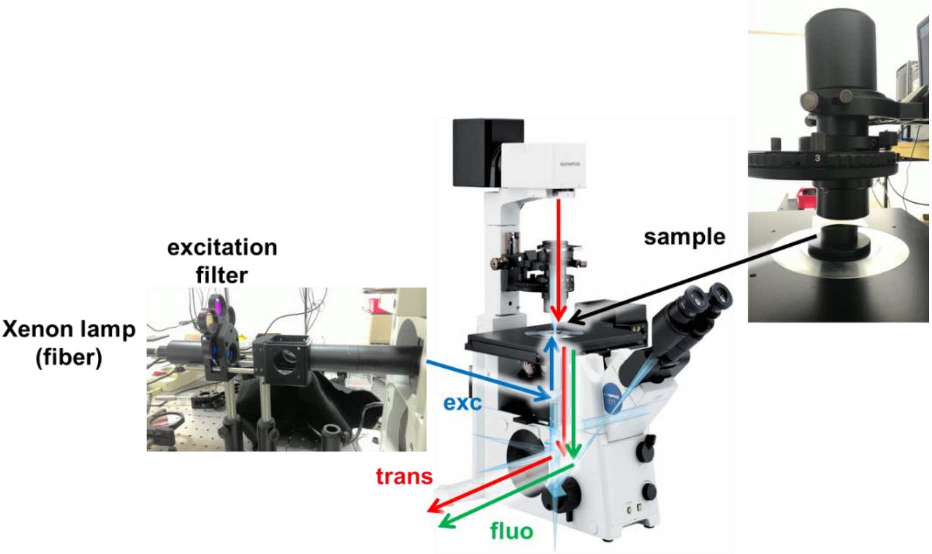

Figure 3.5 Pictures of the wide field microscope used with enlarged view of the excitation part (left) and the stage (right) where the sample is laid down.

In the path between the lens and the objective (whose optical axes are perpendicular) the beam is reflected by a dichroic mirror (that reflects light in a given wavelength range - the excitation one - and transmits that of a longer wavelength, namely the fluorescence). This dichromatic beam splitter is tilted at 45° to the incoming excitation light and reflects the excitation light at a 90° angle directly through the objective and onto the specimen:

Figure 3.6 Dichroic mirror and barrier filter in a typical cube for insertion inside microscope.

Since the beam converges in the back focus of the objectives (OLYMPUS brand, with different magnification depending on the measurements), it exits the microscope as a spot composed of beams parallel to the optical axis that irradiate the specimen in a homogeneous way within a circle that depends on the optical aperture of the excitation system. In the specimen the light is absorbed by the fluorophores, that start to emit fluorescence light in random directions and with a wavelength longer than that of the excitation.

The fluorescence microscope used is an optical inverted instrument, where a lens (called tube lens, 180 mm focal length) reconstructs the enlarged infinity focused image of a sample placed in the focal plane of the objective on the sensor of the detector. In particular, the microscope used is an Olympus IX71:

Figure 3.7 Schematic representation of optical structure of the microscope.

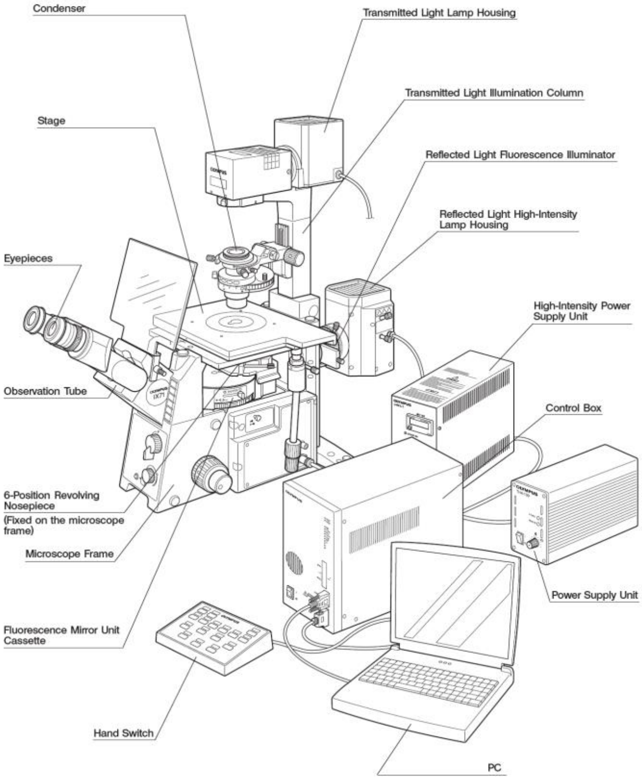

Figure 3.8 All the parts of an Olympus IX71 microscope.

Because the emitted light consists of longer wavelengths, it is able to pass through the dichroic mirror. Any scattered excitation light reaching the dichroic mirror is reflected toward the light source.[4]

3.2.2 Set-up for simultaneous fluorescence and transmission detection

With the aim to collect simultaneously transmission and emission images of the samples, two cameras were put on the exiting path light. In order to do this, a beam splitter was put just before the two cameras: then, it was necessary to put an emission filter (a green one) just before the EMCCD camera (Photon Max) used to detect emission light in order to avoid all the undesired wavelength, and another emission filter (a red one) just before the B&W camera (Tube Lens) used to collect transmission images to avoid all the emission light:

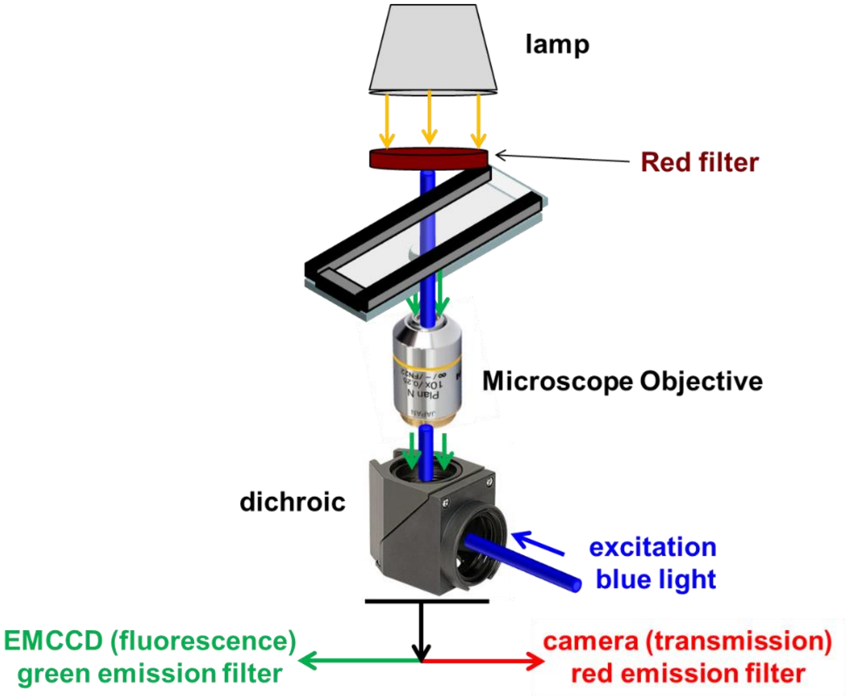

Figure 3.9 Schematic representation of the filters setup of the microscope for the two detection channels.

A similar band pass filter of 640/20 nm was laid down over the cassette in which crystals were created in order to make the microscope light not be seen by EMCCD camera. It has to be noted that these filters are useful for all the different kinds of dyes I used during the experiments.

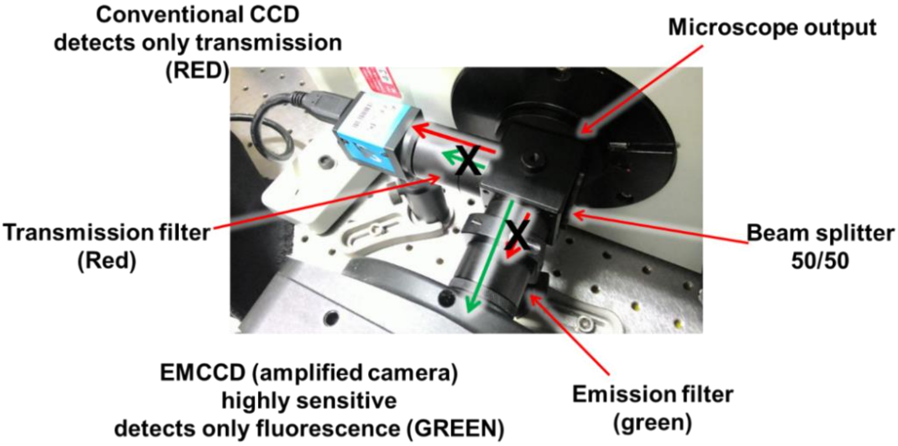

Figure 3.10 Picture of the double channel emission part of the wide field microscope used.

Considering these filters, the dichroic mirror that best suited my setup is *MD480* produced by Thorlabs©, whose characteristic spectrum is shown below:

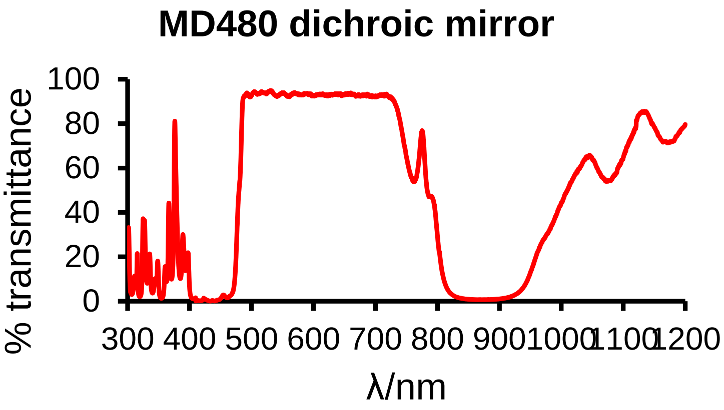

Figure 3.11 Transmittance spectrum of the used MD480 dichroic mirror by Thorlabs®.

3.3 Confocal microscopy

3.3.1 Conventional confocal microscope

Differently from wide field fluorescence microscope, confocal one offers several advantages such as shallow depth of field, elimination of out-of-focus glare, and the ability to collect serial optical sections from thick specimens.

In wide field microscope, the entire specimen is bathed in light from the lamp source, while in confocal microscope the illumination is achieved by scanning one or more focused beams of light across the specimen, the so called optical sections. Considering this, when a widefield fluorescent microscope is used to observe specimens, secondary fluorescence emitted by the specimen appears away from the region of interest, often interfering with the resolution of those features that are in focus. The thicker is the specimen the more problematic is the situation. On the other hand, confocal imaging approach provides a marginal improvement in both axial and lateral resolution. Another important consequence of being able to scan different optical sections is that it is possible to collect three-dimensional (z-series) data over the same sample with the same x-y coordinates.[5]

The confocal inverted microscope used was a Zeiss one, more precisely the one in GenYo department of the Univeristy of Granada:

Figure 3.12 The Zeiss confocal inverted microscope used.

3.3.2 Fluorescence Lifetime imaging microscopy

Fluorescence Lifetime Imaging Microscopy (FLIM) produces an image based on the differences in the excited state decay rate from a fluorescent sample. Thus, FLIM is a fluorescence imaging technique where the contrast is based on the lifetime of individual fluorophores rather than their emission spectra. It has to be considered that fluorescence lifetime does not depend on concentration, absorption by the sample, sample thickness, photo-bleaching and/or excitation intensity, and, on the other hand, it depends on many different environmental parameters such as pH, ion or oxygen concentration, molecular binding or the proximity of energy acceptors, in order to obtain congruent results.[6]

The FLIM used was a MicroTime 200 of the PicoQuant company:

Figure 3.13 The FLIM used: outer (left) and inner (right) views.

3.4 Preparation of biomorph in gel

3.4.1 The crystallization cell

With the aim to create biomorphs in gel, two identical rectangular plates (typically about 10x4 cm) of thin glass were used, separated by appropriately cut frame of rubber (1–2 mm of thickness) covered with grease on both sides to seal the contact area with the plates. Further, three needles are inserted between the rubber and the plates, in order to poured inside the solutions. The whole assembly is finally fixed by applying clamps around the rim, pressing together the glass plates and the rubber in order to seal the whole cassette:

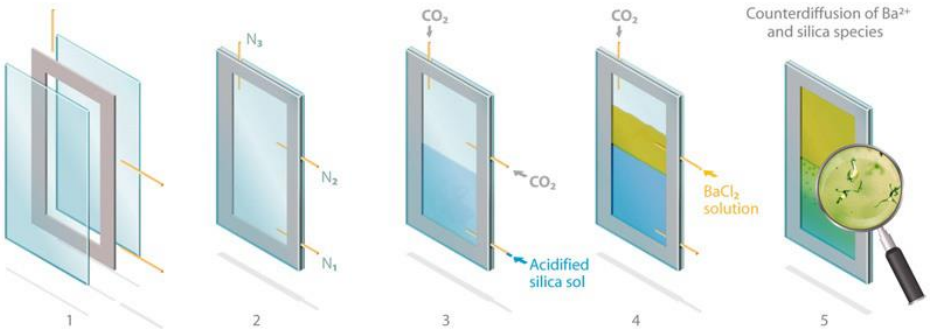

Figure 3.14 Gel-grown biomorphs cassette.[7]

3.4.2 Preparation of the sample

In order to prepare the gel over which pouring the barium solution, a commercial sodium silicate was diluted in a ratio of 1:10 (v/v) with water and then 3.25 mL of 1 M HCl were added to 10 mL of this solution with the aim to gellify the mix, and then this mix was put under vigorous stirring. When the gel is formed, after 5 days latest, a solution of $BaCl_2$ 0.5 M or of $CaCl_2$ 0.2 M, depending on which kind of biomorphs I wanted to create, was poured on top of it. Doing this, the diffusion of Ba^{2+} or Ca^{2+} ions across the gel-solution interface will gradually increase the supersaturation of carbonate and decrease the pH, as functions of time and location in the gel. At the same time, counterdiffusion of silicate species and OH^- ions into the supernatant metal salt reservoir raises the pH (initially ca. 5.5), such that carbonate crystallization will eventually take place there, yielding structures similar to those formed in a regular solution synthesis.[8]

3.5 Preparation of silica gardens

The most common way to produce silica gardens is to place crystals of a metal salt into a beaker and pour alkaline silica solution on them (or, conversely, submerge the salt crystals into a large volume of the sol).

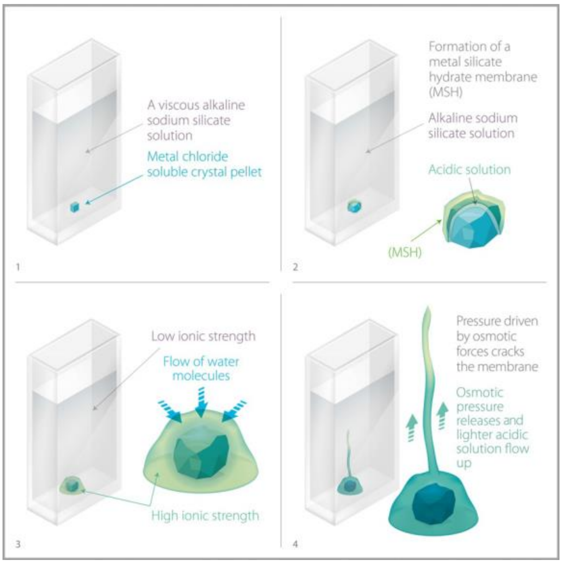

Figure 3.15 Typical method to make silica gardens growth.[7]

The metal salt should contain cations that precipitate upon reaction with hydroxide and/or silicate anions (which is essentially true for all multivalent cations): the most typical cations are Co^{2+}, $Fe^{2+/3+}$, Cu^{2+}, Ni^{2+}, Zn^{2+}, Mn^{2+}, Al^{3+}, and Ca^{2+} in salts with counterions such as Cl^-, NO_3^-, or SO_4^{2-}.[9],[10],[11]

The concentration of the solution (and with it, the different pH) change the morphological evolution, and the optimum range of silica concentrations varies depending on the type of metal salt used to create the chemical garden. The choice of the cation determines the color of the resulting precipitates, while morphologies seem to be not affected by it.[7]

Considering our inverted microscopes setup, which requires that the sample has to be spread out on the horizontal stage, the cassette in which silica garden had to be grown should be totally different. With this aim, I created a double layer made of two microscope and/or cover slides (depending on the working distance of the objective that was used) separated by a double layer of tape on two edges, in order to give some space to the metal salt to grow as a silica garden. In the middle of the two glass slides I put at the beginning a piece of the metal salt and the I poured through an open edge the silicate solution. Lately I was also used to use directly a drop of 2 µL of solution of the metal salt, that Prof. Juan Manuel García-Ruiz and co-workers discovered recently, in the middle of a cover slip glass and then a bigger drop of sodium solution on a microscope slide or another cover slip. Then I put them in contact and started with the acquisition.

3 References

[1] L. Moggi, A. Juris, T. Gandolfi, *Manuale del fotochimico*, **2006**.

[2] V. Balzani, P. Ceroni, A. Juris, *Photochemistry and Photophysics. Concepts, Research, Applications.*, **2014**.

[3] K. R. Spring, in *Encyclopedia of Optical Engineering* (Ed.: I. Marcel Dekker), 270 Madison Avenue, New York, New York 10016, **2003**, pp. 548-555.

[4] M.-T. Abramowitz*, Vol. 4* (Ed.: Fellow), New York Microscopical Society, **1993**.

[5] Nikon.

[6] S. Trautmann, V. Buschmann, S. Orthaus, F. Koberling, U. Ortmann, R. Erdmann, *PicoQuant*.

[7] M. Kellermeier, F. Glaab, E. Melero-García, J. M. García-Ruiz, in *Methods in Enzymology, Vol. 532* (Ed.: J. J. D. Yoreo), Elsevier Inc., **2013**, pp. 225-256.

[8] E. Melero-Garcia, R. Santisteban-Bailon, J. M. Garcia-Ruiz, *Cryst Growth Des* **2009**, *9*, 4730-4734.

[9] D. Balköse, F. Özkan, U. Köktürk, S. Ulutan, S. Ülkü, G. Nişli, *Journal of Sol-Gel Science and Technology* **2002**, *23*, 253-263.

[10] J. H. E. Cartwright, B. Escribano, S. Khokhlov, C. I. Sainz-Diaz, *Phys Chem Chem Phys* **2011**, *13*, 1030-1036.

[11] J. H. Cartwright, B. Escribano, C. I. Sainz-Diaz, L. S. Stodieck, *Langmuir* **2011**, *27*, 3294-3300.

4 Barium biomorphs in gel

4.1 Introduction

The growth of biomorphs in silica gel was investigated in the presence of a fluorescent pH probe with the aim to map the local pH during the process by fluorescence microscopy. The experimental setup is described in detail in chapter 3. In summary, a glass crystallization cell having an internal size of about 80x40x1 mm^3 (see figure 4.1) was half-filled with the gel solution precursor containing the fluorescent probe. After jellification (the setting takes several days), a solution of $BaCl_2$ was injected on top of the gel ins the empty part of the cell.[1] The solution and the gel come into contact at the interface and diffusion of the barium from the solution into the gel starts.[2] The permeation of the barium solution into the gel creates a time dependent profile of the metal and initiates chemical reactions that finally bring to the formation of the biomorphs which are expected and in part known to induce changes in the local pH.[3],[4] Investigating these local pH changes is one of the objective of this PhD thesis work.

Figure 4.1 Picture of a typical cassette used to create gel-grown barium biomorphs.

4.2 Brief description of the experimental approach

Mapping fluorescence and pH in a large (several cm^2) system as a gel with good spatial resolution and precision for several days is a hard task.

In the first experiments we tried to image the whole area of the gel (about 40x40 mm^2) simultaneously using a custom optical set up. In this initial approach we used a Xe lamp in combination with specific filter for the excitation while the fluorescence was acquired through a photographic objective and a CCD camera. This approach gave quite poor quality results because of the following problems:

1) **weak signal**. Imaging of a large area requires to position the objective quite far (several centimeter) from the sample. As a consequence, a very small fraction of the emitted light (fluorescence) is collected;
2) signal intensity can be in part improved by increasing the excitation intensity. As a severe drawback this causes a serious **photobleaching** of the pH probe;
3) sensitivity can be improved by using amplified CCD camera for detection (EMCCD). Nevertheless, EMCCD sensors are typically composed by a limited array of pixel (512x512), hence **poor resolution** is achieved when a large area is observed.

Hence for a complete pH mapping, we preferred to use a wide field fluorescence microscope, to acquire and combine different images, each of them corresponding to a size of about 5x5 mm^2, as schematized in figure 4.2. The use of the microscope allowed us to collect fluorescence in close proximity to the gel with a high numerical aperture (NA) objective and an EMCCD camera, increasing the sensitivity. Moreover, acceptable resolution could be achieved mapping relatively small area.

Although photo-bleaching was in part reduced by decreasing the excitation intensity, considering the duration of the experiment (about 3 weeks including gel preparation), its effect on the fluorescent probe became relevant especially considered that photodegradation becomes very sever in alkaline environment. Additionally, undesired diffusion of the probe in the gel during the experiment was observed.

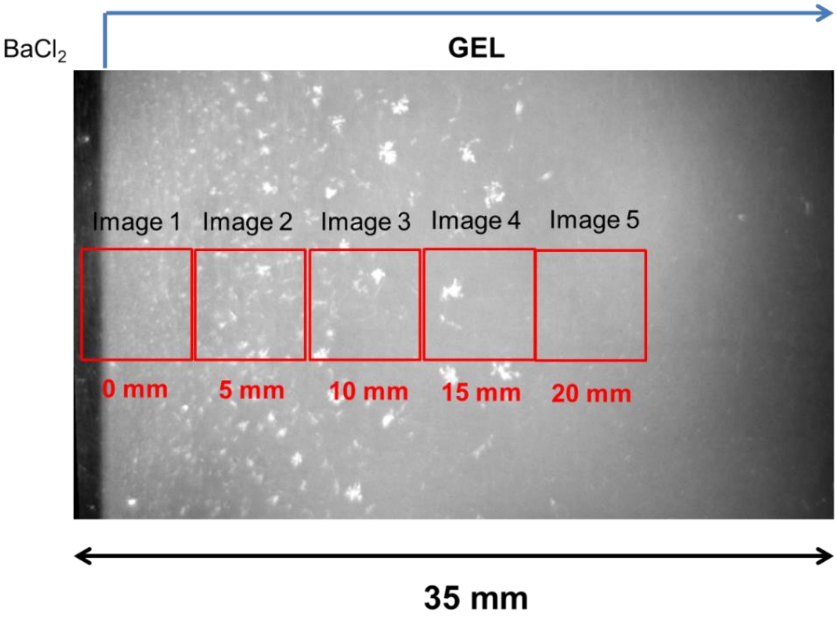

Figure 4.2 Frames of the different areas chosen to monitor the gel-grown barium biomorphs. λ_{exc}=460 nm.

In order to avoid these problems, we preferred to use the **ratiometric signal detection** for pH measurements, since it allows to take into account possible dis-homogeneity in the distribution of the pH probe in the gel arising from probe photo-bleaching or diffusion.

As mentioned in chapter 3 this method is based on the acquisition of two signals that present a different dependence on the pH (for example one is pH dependent and the other is pH independent) and to combine them to have a parameter which is independent on the probe concentration.

The criteria at the basis of the choice of the pH probe have been widely discussed in chapter 3. In particular, we selected a pH probe that could switch on its fluorescence (being very weakly fluorescent in the alkaline form) upon protonation at about 1 pH unit below the bulk pH of the gel which is about 10.6. We investigated acridine orange (AO) and acridine yellow (AY) that demonstrated to match these requirements (see chapter 3). Comparing these two dyes we concluded that AY, for the pK_a and the photophysical properties in silica gel, was the most suitable pH probe. Preliminar experiments confirmed this expectation.

4.3 Results and discussion

The gel was prepared as described in experimental section 3.5.2, using a commercial sodium silicate solution (Sigma Aldrich) diluted in a ratio 1:10 (v:v) with MilliQ water, to which HCl 1M (325 µL/mL with respect to the diluted silica) was added in order to activate the jellification process. The HCl solution also contained the pH fluorescent probe AY at a concentration 0.33 mM.

Silicate content of commercial sodium silicate is expressed in terms of amount of silica (SiO_2 about 27% w/w) and Na_2O (about 8% w/w). These concertation values correspond to a 6.0 M molar concentration of SiO_2 while of Na_2O is 1.7 M. Hence the dilute solution (1:10 v:v) contained SiO_2 0.45 M, Na_2O 0.17 M and HCl 0.3 M.
In figure1.8 is shown the titration plot of 10 mL of the diluted silica solution with HCl 1 M.[2] The initial pH of the solution is about 11.8 and a small decrease is observed up to the addition of 3 mL (pH=10.8). The pK_a of $Si(OH)_2O_2^=$ is about 9.9 and this pH is reached after the addition of about 3.5 mL of HCl. This corresponds to the complete neutralization of Na_2O (0.17 M, corresponding to NaOH 0.34 M).
From geometrical considerations we estimated the volume of the cell shown in figure 4.1 to be 80x40x1 mm^2 and hence about 320 µL. Hence, about 160 µL were necessary to fill half-cell. For each experiment we prepared 3 mL of gel precursor solution and five different cells. The cassettes were positioned vertical and kept at room temperature in the dark for 5 days in order to allow the complete setting of the gel. Final gel had a pH of about 10.6-10.8. Gel presenting bubbles or fractures were discarded.

The formation of the barium carbonate biomorphs was initiated by injecting, very slowly, a solution of $BaCl_2$ (0.25 M) on the top of the formed gel. The diffusion of the barium solution into the gel produced a partial decrease of the transparency of the gel that became slightly turbid at the interface.

In order to correlate the fluorescence change to biomorphs formation it was fundamental to acquire simultaneously the optical transmission image of the gel and the fluorescence one. For this purpose, we developed a specific setup which is described in detail in chapter 3. In particular, we used the illuminator (on the top of the sample in the inverted configuration of microscope Olympus IX-71) to acquire the transmission image with a black and white conventional CCD camera (The ImagingSource). The fluorescence image was acquired with an amplified camera EMCCD (Princeton PhotonMax 512) upon excitation with a xenon lamp connected through an optical fiber to the back-port of the microscope. The two cameras were coupled to the left port of the microscope (exit port) by splitting the image with a prism (50/50). To avoid cross-taking between fluorescence and transmission detection we used two well separated color channels. Considered that the AY emission is green, inside the channel used to acquire fluorescence a suitable band-pass filter (520/40 nm) was inserted in the front of the EMCCD camera. For transmission, red channel was used by filtering the illuminator light with a red band-pass (650/40 nm) filter. Summarizing we used a two-channels system using a red band-pass filter for optical transmission and a green one for fluorescence.

As previously discussed, our first experiments demonstrated that photobleaching and pH probe diffusion are very critical, so finally we developed an approach alternative to simple single channel detection of the fluorescence exploiting ratiometric imaging.

This method required the use of suitable pH probe (we showed that AY is appropriate) and the simultaneous acquisition of two fluorescence images at different excitation wavelengths. This was achieved by using two different band pass excitation filters for the xenon lamp and in particular a first filter (EXC1) centered at 390/18 nm and a second one (EXC2) at 445/45 nm. Summarizing, we acquired a set of 3 image for each time (t) of observation, hence: transmission (T(t)), fluorescence at EXC1 (F1(t)) and fluorescence at EXC2 (F2(t)). We would like to stress that indeed it is not experimentally possible to detect images F1 and F2 exactly at the same time since it is required to alternate excitation EXC1 and EXC2. Nevertheless, considered that the processes under investigation (diffusion and biomorphs formation) are quite slow we first verified in preliminary experiments that no detectable changes in the images occur in a 120 seconds time interval and hence we assumed that the images acquired within 60 seconds could be considered as simultaneously acquired.

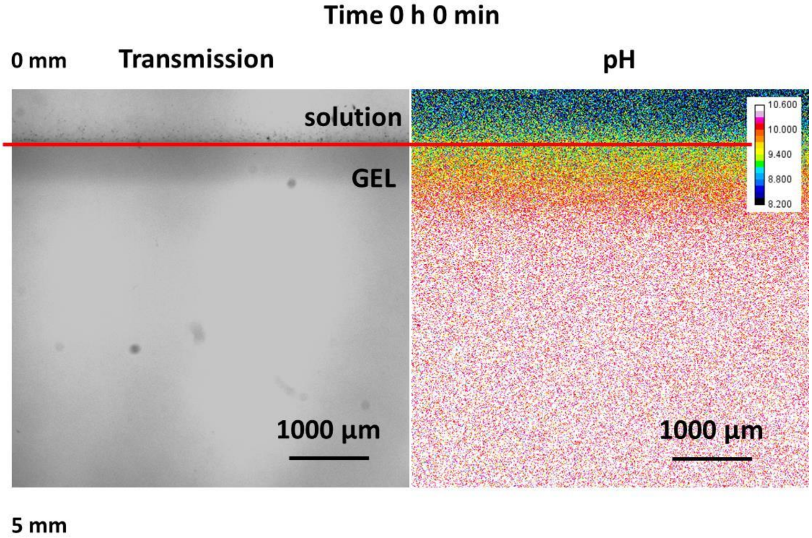

Figure 4.3 Transmission image (left) and pH map (right) calculated from ratiometric intensity analysis (λ_{exc1}=400 nm, λ_{exc2}=460 nm) immediately after the injection of $BaCl_2$ solution. Images were collected with a wide field fluorescence microscope.

In the representative experiment we reported in this chapter, the process of biomorphs growth was investigated for 5 days after the injection of $BaCl_2$ solution. As mentioned the field observed with the microscope at a 2X magnification objective was 5x5 mm^2, hence, in order to map the pH, five different images were acquired at different distances with respect to the interface (0, 5, 10, 15 and 20 mm) to cover a total area of 25x5 mm^2. Summarizing, **at any time t it was necessary to acquire three images (T, F1, F2) at five different positions x as a total of 15 images.**

Nevertheless, preliminary experiments showed that during the first hour of observation diffusion was limited to the first 5 mm layer, so we preferred to avoid to reposition the sample during first initial time.

In order to calculate pH fluorescence images, F1 and F2 were processed to calculate the ratiometric signal R=F1/F2 that was hence converted into pH using ImageJ software.

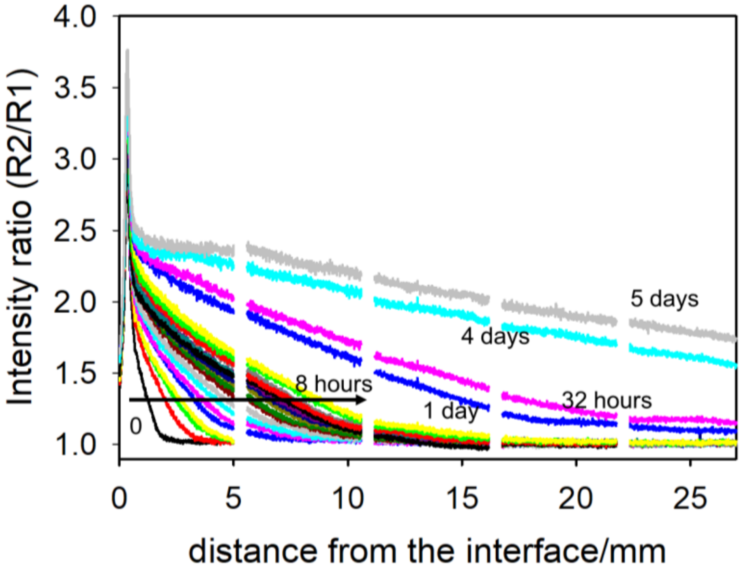

Figure 4.4 Intensity ratio of the signal (λ_{exc2}=460 nm) and the reference (λ_{exc1}=400 nm) along the different frames reported in fig. 4.1 at different times.

Figure 4.3 shows the transmission and pH images acquired immediately after the injection of $BaCl_2$ in the top of the cell. In the transmission images a dark band can be observed in the close proximity of the interface that indicates the **precipitation of hydrate barium silicate** or **barium carbonate.** Considered that the concentration of carbonate is very low in the system, we believe that it concerns the formation of silicate more likely, although a more detailed investigation of the nature of the precipitate in the closed system was not possible. Interestingly the pH map (figure 4.3 right) reveals a drop of the pH from 10.6 to about 9.0 at the interface. A decrease of the pH, even if less pronounced, is observed also in the gel region in close proximity to this precipitation band. The pH dependence on the distance from the interface can be better analyzed by plotting the fluorescence intensity ratio R (which is the experimental parameter used for pH calculation) or the calculated pH as a function of the distance from the interface. The plots are shown in figure 4.4 and 4.5, respectively, and they were obtained with the function “plot profile” of ImageJ.

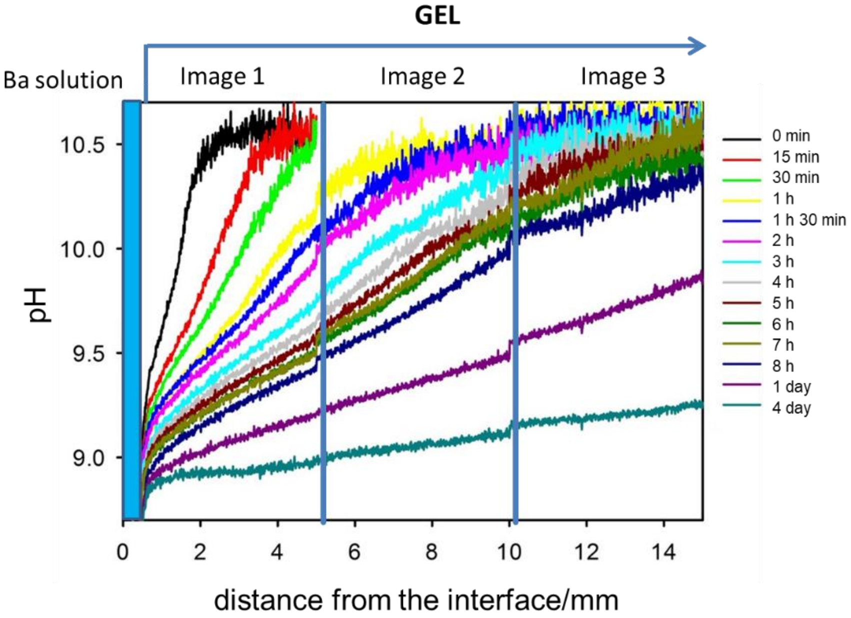

Figure 4.5 pH along the different frames reported in figure 5.2 at different times.

The ratiometric fluorescence profile at t=0 min is shown in figure 4.4. as a black line: the ratiometric signal decreases fast to the bulk value (R~1.0) in the first 2 mm from the interface. This change corresponds in the pH plots of figure 4.5 to a rise of the pH from about 9.0 to the bulk value 10.6 in the same 2 mm. We would like to stress that the images of figure 4.3 are the first one acquired after barium injection and correspond to acquisition time t=0 min but indeed about 1-2 minutes are necessary for this first acquisition, and so partial diffusion of the barium into the gel already occurred.

The change in pH observed in the gel near the interface (from 10.6 to 9) is dramatic if it is considered that, looking at the titration curve of figure

1.8, it corresponds virtually to the addition of HCl 0.1 M. This completely ruled out the possibility that the pH change is due to the formation of barium carbonate; this would require a concentration of carbonate in the gel of the same order of magnitude, namely 0.1 M, which is not reasonable to consider even if the gel was partially exposed to air CO_2. We can hence conclude that acidification is due to barium silicate formation.[3]

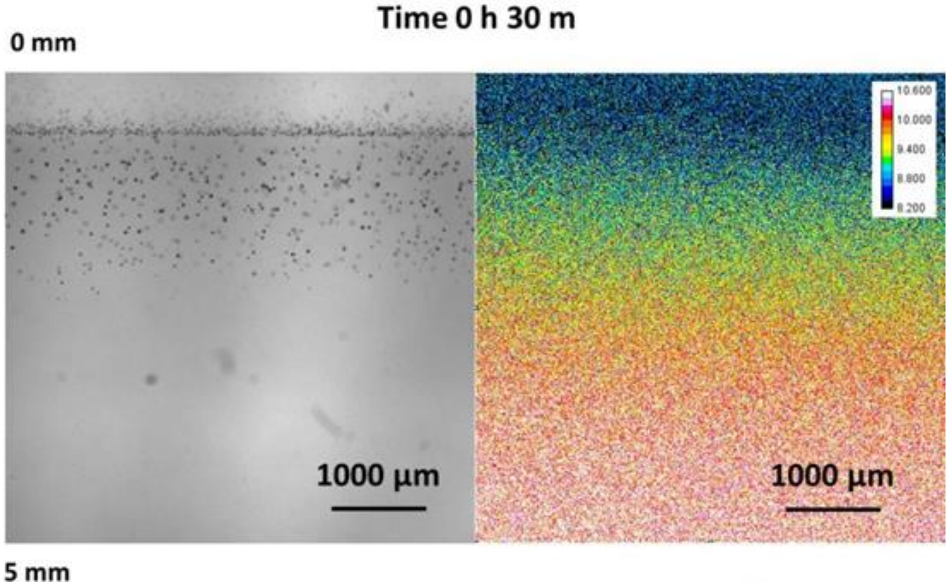

Figure 4.6 Transmission image (left) and pH map (right) calculated from ratiometric intensity analysis (λ_{exc1}=400 nm, λ_{exc2}=460 nm) 30 min after the injection of $BaCl_2$ solution. Images were collected with a wide field fluorescence microscope.

The formation of visible individual crystals is possible already 15 min after Ba injection. In particular, figure 4.6 shows in the transmission image on the left the presence of small (up to tens of µm) particles in the first 2 mm from the interface. The pH map, on the right in the same figure, indicates that the region of decreased pH is larger than the one at t=0 min. Also in this case a darker region in transmission is detected in the area where the pH is decreased. In figures 4.4 and 4.5 it can be clearly observed that the “acidic front” (indeed the gel is still alkaline but a pH decrease is propagating inside it) has moved to about 5 mm, a distance at which the pH is still the initial one. We would like to stress that, in this phase, the shape of the particles is still rather “spherical” and no actual defined biomorphic shapes can be detected.

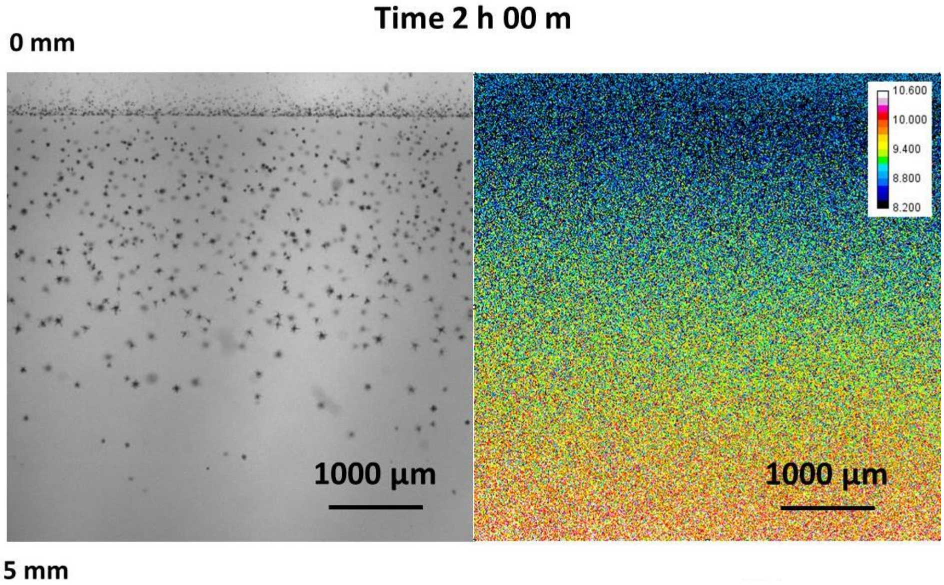

Figure 4.7 Transmission image (left) and pH map (right) calculated from ratiometric intensity analysis (λ_{exc1}=400 nm, λ_{exc2}=460 nm) 2h after the injection of $BaCl_2$ solution. Images were collected with a wide field fluorescence microscope.

The ratiometric profiles of figure 4.4 can be, at least for the first few hours, fitted as pure diffusion profile assuming a 1D model where the solution behaves as a reservoir with constant concentration (of barium that diffusing in the gel produces the pH change). To indicate the position of this diffusion front it is convenient to indicate the distance $x_{1/2}$ from the front at which the change of the R signal is half the total variation (the difference between the interface and the bulk). After 30 min this distance is about 2 mm and it increases with time.

As shown in figure 4.7, after 2 h biomorphic structures start forming at about 2 mm from the interface. Looking at the pH map reported in the same figure it is possible to observe that biomorphs are formed in a horizontal band which has a pH around 9.5. This can be seen also in the pH profiles of figure 4.5. We would like to underline that the particles already formed closer to the interface and that are embedded in an environment with lower pH (about 9.0) do not evolve into biomorphs.

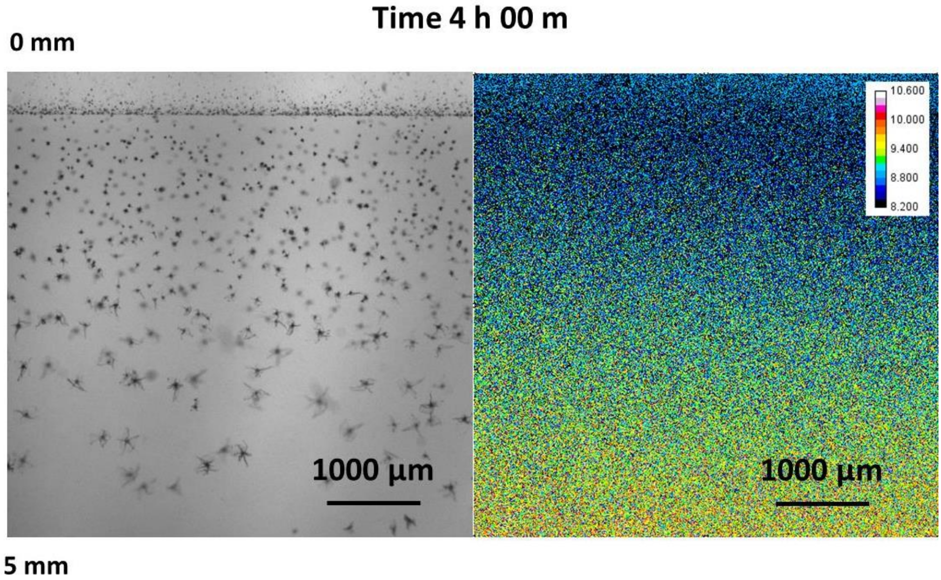

Figure 4.7 Transmission image (left) and pH map (right) calculated from ratiometric intensity analysis (λ_{exc1}=400 nm, λ_{exc2}=460 nm) 4h after the injection of $BaCl_2$ solution. Images were collected with a wide field fluorescence microscope.

Larger star-shaped biomorphic structures are formed after 4 hours at about 3 mm from the interface. These biomorphs have sizes of the order of hundreds of µm and are formed in a band where the pH is about 9.5. Comparing these results with what discussed for the images acquired after 2 h, we can reach the very important conclusion that this **pH value of 9.5 is characteristic of the environment where the biomorphs are formed.**

Figure 4.8 reports the transmission and pH images 8 hours after the injection. It is possible to identify very large biomorphs that are forming at about 4 mm from the interface again in gel region where the pH is around 9.5.

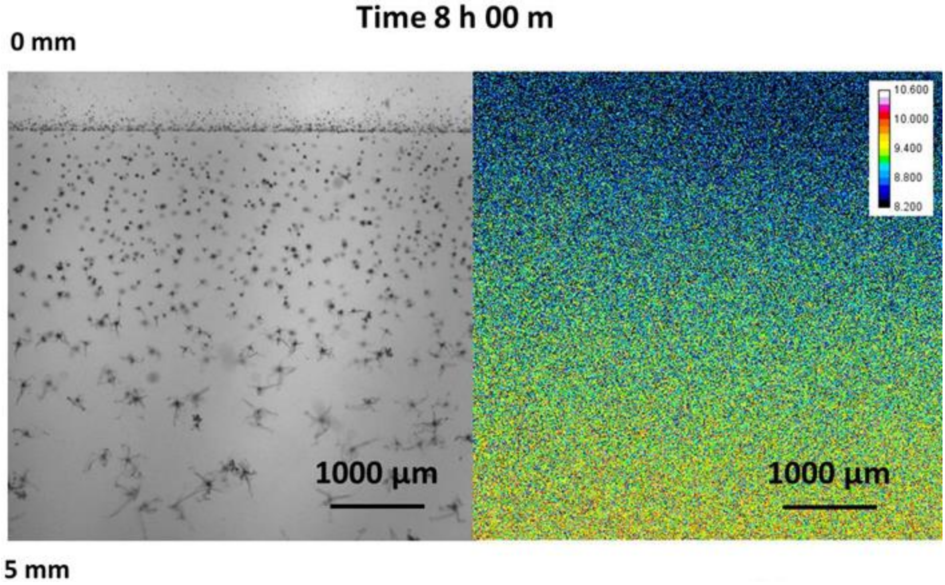

Figure 4.8 Transmission image (left) and pH map (right) calculated from ratiometric intensity analysis (λ_{exc1}=400 nm, λ_{exc2}=460 nm) 8 h after the injection of $BaCl_2$ solution.

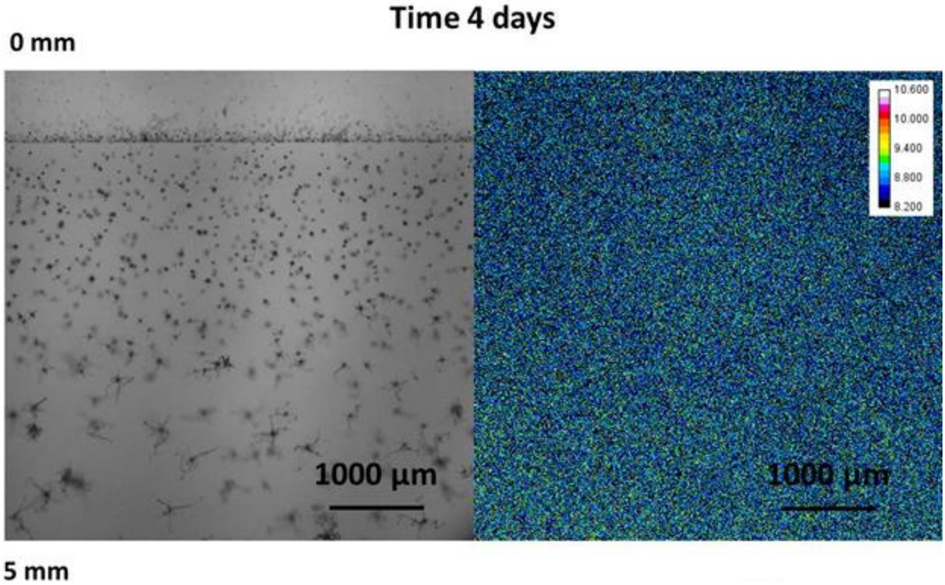

Figure 4.9 Transmission image (left) and pH map (right) calculated from ratiometric intensity analysis (λ_{exc1}=400 nm, λ_{exc2}=460 nm) 4 days after the injection of $BaCl_2$ solution.

Four days after the injection of Ba, the image observed in transmission optical microscopy is very similar to the one acquired after 8 h (figures 4.9 and 4.8). The biomorphs did not increase significantly their size or changed their morphology. On the contrary, the “acidic front” continued to propagate (as observable in figures 4.4 and 4.5) and the pH in the whole area from 0 to 5 mm from the interface seems to remain constant about 9.0 (figure 4.9).

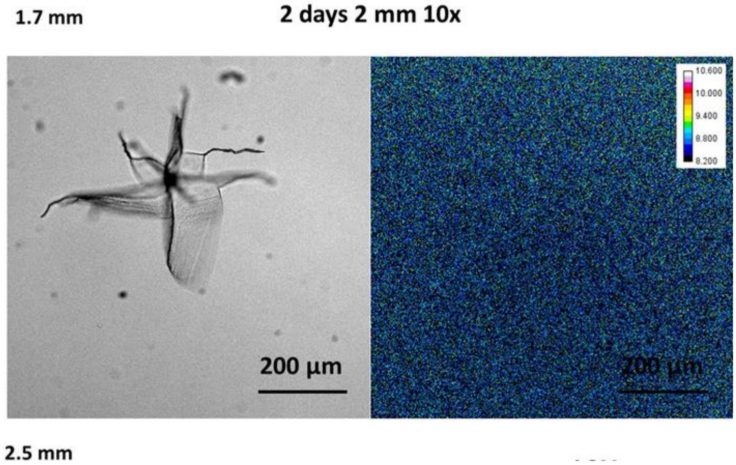

Figure 4.10 Transmission image (left) and pH map (right) calculated from ratiometric intensity analysis (λ_{exc1}=400 nm, λ_{exc2}=460 nm) 4 days after the injection of $BaCl_2$ solution.

Images of figure 4.9 were magnified using a 10x objective: one biomorph is shown in figure 4.10. It has a size, after 4 days, which is as large as 500 µm.

Since in a previous paper it has been reported a relevant decrease of the local pH in close proximity of the forming biomorph **in solution,**[3] we analyzed the pH profile with 10X magnification in search of very local pH variation. As shown, for example in figure 4.10 right, **no local pH changes could be observed around the biomorphs in the gel.**

4.3.2 Estimation of the diffusion rate coefficient

Fluorescence and intensity profiles discussed in the previous sections are related to diffusion of chemical species from the solution into the gel.

In order to better characterize these diffusive processes, we analyzed the diffusion plots in a more quantitative way to estimate the diffusion coefficients of the diffusing species. In particular, using the Fick's law in the case of 1D diffusion into a homogenous medium from a reservoir at concentration c_0 we expect the diffusion profile to evolve in time according to the following equation:

$$c = c_0(1 - erf\frac{x}{2\sqrt{Dt}})$$

where *c* is the concentration of the tracer at a distance *x* from the surface, *t* is time of the diffusion, and *D* is the diffusion coefficient.

Hence if we define $x_{\frac{1}{2}}(t)$ as the distance at which $c = \frac{c_0}{2}$ we obtain the following simple equation:

$$x_{\frac{1}{2}}(t) = 0.954\sqrt{Dt}.$$

Hence we plotted $x_{1/2}$ as a function of time in figure 4.11.

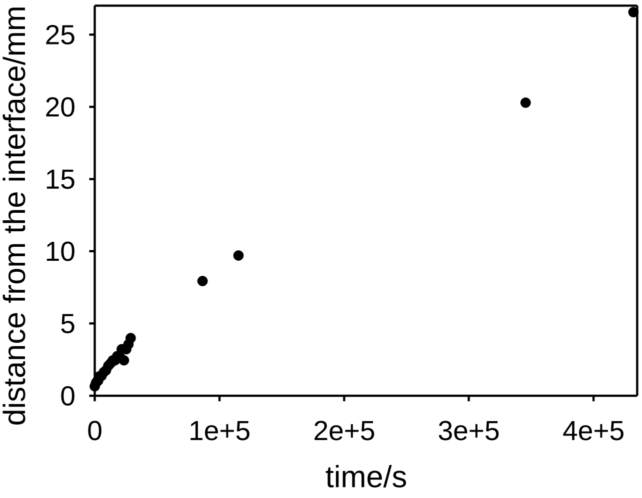

Figure 4.11 Plot of $x_{1/2}$ as the distance at which $c = \frac{c_0}{2}$ as a function of time.

In order to better visualize whether the data of figure 4.11 were compatible with a pure diffusional behavior, we plotted the square of $x_{1/2}$ as a function of time (figure 5.12): in the case of diffusion a linear plot is expected.

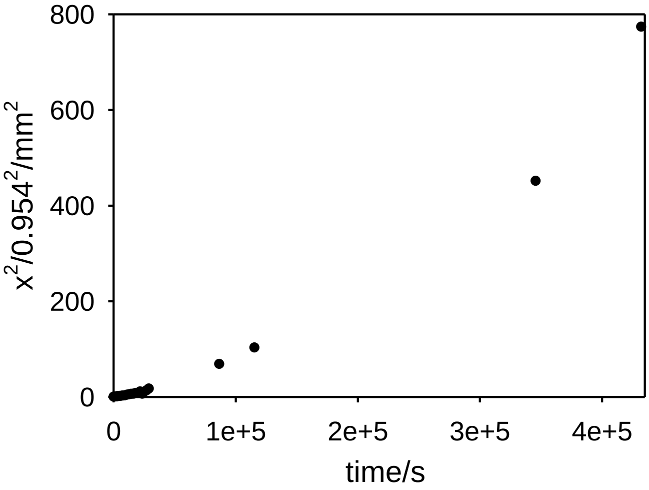

Figure 4.12 Plot of the square of $x_{1/2}$ as the distance at which $c = \frac{c_0}{2}$ as a function of time.

The data shown in figure 4.12 clearly presents a linear dependence, at least for the first 30 hours. For longer times, on the other hand, the model adopted for 1D diffusion stops to be acceptable because the diffusion distance becomes comparable to the gel length and the calcium solution is no more an ideal reservoir.

Hence we fitted this first part of the plot and got a diffusion coefficient D=1x10^{-3} mm^2/s. This corresponds to a diffusion coefficient 1x10^{-9} m^2/s which is of the typical order of magnitude of diffusing ionic species.

4.5 Conclusions

The growth of biomorphs in silica gel was investigated in the presence of a fluorescent pH probe with the aim to map the local pH during the process by fluorescence microscopy.

In order to avoid problems such as dis-homogeneity in the distribution of the pH probe in the gel arising from probe photo-bleaching or diffusion, we preferred to use the ratiometric signal detection for pH measurements. Moreover, in order to correlate the fluorescence change to biomorphs formation, we acquired simultaneously the optical transmission image of the gel and the fluorescence one. Hence, this method required the simultaneous acquisition of two fluorescence images (F1, the fluorescence derived from signal excitation, and E2, the fluorescence derived from reference one) at different excitation wavelengths: this means that at any time t it was necessary to acquire three images (T, F1, F2) at different positions.

In order to calculate pH fluorescence images, F1 and F2 were processed to obtain the ratiometric signal R=F1/F2 that was hence converted into pH using ImageJ software.

In the transmission images a dark band was observed in the close proximity of the interface that indicates the precipitation of hydrate barium silicate or barium carbonate. Interestingly the pH map reveals a drop of the pH from 10.6 to about 9.0 at the interface. A decrease of the pH, even if less pronounced, is observed also in the gel region in close proximity to this precipitation band. This completely ruled out the possibility that the pH change is due to the formation of barium carbonate, and so we could conclude that acidification is due to barium silicate formation.

We also observed that biomorphs are formed in a horizontal band which has a pH around 9.5; while the particles already formed closer to the interface and that are embedded in an environment with lower pH (about 9.0) do not evolve into biomorphs.
Larger star-shaped biomorphic structures are formed after few hours at about 3 mm from the interface. These biomorphs have sizes of the order of hundreds of µm and are formed in a band where the pH is about 9.5. Comparing al the obtained results, we reached the very important conclusion that this pH value of 9.5 is characteristic of the environment

where the biomorphs are formed. Moreover, no local pH changes could be observed around the biomorphs in the gel.

Considering that fluorescence and intensity profiles are related to diffusion of chemical species from the solution into the gel, we decided to better characterize these diffusive processes. Hence we analyzed the diffusion plots in a more quantitative way to estimate the diffusion coefficients of the diffusing species, in particular, using the Fick's law in the case of 1D diffusion into a homogenous medium. We found out that our data clearly present a linear dependence, at least for the first 30 hours. For longer times, on the other hand, the model adopted for 1D diffusion stops to be acceptable because the diffusion distance becomes comparable to the gel length and the calcium solution is no more an ideal reservoir. Fitting the first 30 hours data we got a diffusion coefficient $D=1x10^{-3}$ mm^2/s. This corresponds to a diffusion coefficient $1x10^{-9}$ m^2/s which is of the typical order of magnitude of diffusing ionic species.

5 References

[1] M. Kellermeier, F. Glaab, E. Melero-García, J. M. García-Ruiz, in *Methods in Enzymology, Vol. 532* (Ed.: J. J. D. Yoreo), Elsevier Inc., **2013**, pp. 225-256.

[2] E. Bittarello, D. Aquilano, *Eur J Mineral* **2007**, *19*, 345-351.

[3] E. Melero-Garcia, R. Santisteban-Bailon, J. M. Garcia-Ruiz, *Cryst Growth Des* **2009**, *9*, 4730-4734.

[4] J. Eiblmeier, M. Kellermeier, D. Rengstl, J. M. Garcia-Ruiz, W. Kunz, *Crystengcomm* **2013**, *15*, 43-53.

5 Calcium biomorphs in gel

5.1 Introduction

In this chapter we will describe the pH mapping based on the use of a fluorescent probe in the case of calcium gel-grown biomorphs. The method for the preparation of these structures is quite similar to the one discussed in chapter 4 for barium biomorphs, with the exception that the silica gel is en**riched of carbonate** since during the preparation of the precursor solution Na_2CO_3 is added to the silicate. Gellification is initiated by adding amount of HCl solution that contains also the pH probe AY; the complete gel setting takes place after about one week. The $CaCl_2$ solution is then poured on the top of the gel starting diffusion of the barium in the silicate matrix.[1] It is known that in these conditions both calcite and aragonite crystals are obtained. Interestingly the two forms of $CaCO_3$ are formed in different positions with respect to the interface and they are organized in bands or stripes perpendicular to the calcium diffusion direction. In particular, only aragonite is biomorphic giving characteristic **flower like structures** that appear in **a single band at a distance of 10-15 mm from the interface** with the calcium solution.[2] Both at shorter and longer distances elongated non biomorphic calcite crystals are formed.[3] One of the objective of this research is indeed to understand if this band structure is related to the evolution of pH in the system during the growth.

5.2 Brief description of the set up

In some preliminary experiments we tried to redesign the cells used for biomorphs growth and in particular to reduce the gel area in order to have a smaller sample more suitable for the observation at the fluorescence microscope. These experiments demonstrated that changes in the geometry of the cell has a detrimental effect on the formation of the biomorphs and no aragonite flower like crystals bands could be obtained in those conditions.

Hence we used the same cassette shown in chapter 4 for barium biomorphs with 1 mm thickness and an area of about 50x50 mm^2 filled with the gel. The cassette was made by two glasses separated by rubber as described in figure 3.15 in chapter 3.5.1.[4]

The gel was prepared as described in experimental section 3.5.2, using a solution of commercial sodium silicate (Sigma Aldrich containing about 27% SiO_2, 7% Na_2O) that was diluted ten times (1:10 v/v) with MilliQ water. In this case Na_2CO_3 0.2 M was added to the silicate solution. Gellification was initiated by adding an acidic solution, HCl 1M (350 µL/mL with respect to the silicate), already containing the pH probe.

The crystallization cell was half-filled with this solution. Five different cells were prepared and stored at room temperature in the dark for 1 week. After that, gels showing bubbles or clear ruptures were discard, and the remaining cells were used for crystallization experiments.

For starting the experiment, we injected a $CaCl_2$ solution 0.2 M on the top of the gel, filling completely the empty volume of the cassettes.

The choice of AY used as pH fluorescent probe was discussed in chapter 2. Shortly summarizing, this probe is non fluorescent (upon excitation at 460 nm) at the alkaline pH (about 10.5) of the gel but it becomes fluorescent upon pH decrease (OFF/ON response to protonation), having a pK_a=8.9 (this means that at pH 8.9 the signal is 50 % switched ON). Hence this molecule is suitable to detect local pH decrease of 1-2 units of pH starting from the bulk gel pH. Furthermore, this molecule is suitable as a ratiometric probe upon dual excitation (400 and 460 nm, using 445/45 nm and 390/18 nm excitation Thorlabs® filters). As mentioned, and as it will be show in the next sections, ratiometric detection allows to correct artifacts on the pH measurements due to probe diffusion and photobleaching.

5.3 Results

The aim of this part of my thesis was to map the pH in the gel at the local level during the growth of the biomorphs. As mentioned in chapter 4, using fluorescence for mapping pH in large object is not trivial. As previously discussed, our first experiments demonstrated that photobleaching and pH probe diffusion are very critical, so finally we developed an approach alternative to simple single channel detection of the fluorescence exploiting ratiometric imaging. Moreover, for improving spatial resolution and sensitivity we preferred imaging small area (5x5 mm^2) acquiring **partial images** of the gel, and then to reconstruct a larger image by merging with ImageJ the single part (this approach in microscopy is called **image stitching**).

Summarizing we combined **ratiometric detection and image stitching**; this means that we acquired a set of 3 image for each time (t) of observation hence: transmission (T(t)), fluorescence at EXC1 (F1(t)) and fluorescence at EXC2 (F2(t)), and that five different images were acquired at different distances with respect to the interface (0, 5, 10, 15 and 20 mm) to cover a total area of 25x5 mm^2. Hence **at any time t it was necessary to acquire three images (T, E1, E2) at five different positions x for a total of 15 images.**

Although, since preliminarily experiments showed that during the first hours of observation diffusion was limited to the first 5 mm layer, we preferred to avoid to reposition the sample during first initial time.

In order to calculate pH fluorescence, images F1 and F2 were processed to calculate the ratiometric signal R=F1/F2 that was hence converted into pH using ImageJ software.

We would like to stress that this approach based on ratiometric detection and image stitching is very powerful and combine precise pH determination to large area imaging. Nevertheless, as drawback the acquisition process is quite low and it requires sample repositioning.

For this reason, we also performed **simpler experiments** using a single channel fluorescence detection (**non ratiometric**) and limiting the observation are the **first 5 mm** of the gel. As an advantage these experiments allowed us to follow the evolution of morphology and pH simultaneously almost in **real time** using two different CCD (and wavelength intervals) to monitor transmission and fluorescence (the setup is described in detail in chapter 3).

We will report and discuss first the results obtained with this simple method.

5.3.1 Short-term pH imaging (non-ratiometric)

In this experiment we collected time-lapse video both in fluorescence, using only the 445/45 nm excitation, and in transmission mode, for the first 3 hours and a half after $CaCl_2$ injection in a region of the gel of about 5 mm starting from the interface.

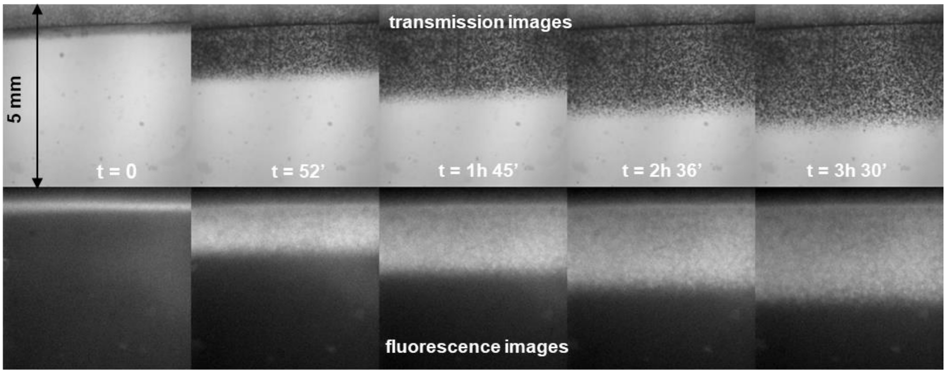

Figure 5.1 Transmission (top) and fluorescence (bottom, λ_{exc}=460 nm) images of the first 5 mm from the interface of the silica gel (containing AY) during calcium diffusion at different times, using an inverted wide field fluorescence microscope. $CaCl_2$ solution is on the top of the interface, while the gel is in the bottom, where there is the formation of the crystals over time. 5 sec of integration time.

Images acquisition in this single fluorescence channel approach is very fast (with respect to the process observed, hence the diffusion of chemical species in solution over several mm distances) and we could acquire a frame every 5 seconds (12 frames in a minute). Faster acquisition in principle is possible but it would require a stronger excitation intensity that would cause an enhanced photobleaching of the pH probe. Some of the images acquired, at selected delay time after the calcium injection, are reported in figure 5.1. The transmission images (on the top in figure 5.1) clearly show the formation of densely packed crystal in proximity of the interface. The region where precipitation occurs expands during time, being about 1.5 mm wide (starting from the interface) after 52 minutes and about 3 mm after 210 minutes.

Precipitation is clearly due to the diffusion of calcium into the gel and the formation of $CaCO_3$ crystals. We would like to underline that this process is expected to affect the pH of the gel. As the bulk pH (10.5), part (about 50%) of the carbonate is in fact present in the form of HCO_3^- (the pK_a of this species is 10.3). Calcium itself is very slightly acidic and the hydrolysis of Ca^{2+} inside the solution that is poured on top of the gel drives the pH value close to 5.8, according to the equilibrium:

$$Ca^{2+} + H_2O \rightleftarrows Ca(OH)^+ + H^+.$$

This process has negligible effect on the pH of the gel; nevertheless, the diffusion of Ca^{2+} inside the gel in the presence of HCO_3^- and CO_3^{2-} leads to the precipitation of calcium carbonate:

$$Ca^{2+} + CO_3^{2-} \rightleftarrows CaCO_3$$

$$Ca^{2+} + HCO_3^- \rightleftarrows CaHCO_3^+$$

$$CaHCO_3^+ \rightleftarrows CaCO_3 + H^+.$$

The latter reaction clearly produces a decrease of the pH.

Fluorescence images in figure 5.1 clearly confirm this decrease of pH in the region where the precipitation occurs. Fluorescence intensity in fact strongly increased in the precipitation area because of the protonation of AY.

To demonstrate that there is a very good correlation between crystals formation and fluorescence increase we processed all the data (images acquired every 5 seconds) as shown in figure 5.2. We first selected a line vector in the direction of the calcium diffusion (hence perpendicular to the interface and directed from the solution toward the gel) which is represented as a yellow line in the figure 5.2. Hence we used the “plot profile” function of ImageJ to calculate the intensity profile across this line. The intensity profiles at different times were merged in a single data array that, as a consequence, contains intensity values as a function of time and position across the diffusion vector. This intensity surface was plotted in false colors as contour plot in figure 5.2 and correlate to the initial transmission image (left) and the final one (right). Figure 5.2 clearly shows that after 208 minute the front of the fluorescent band and the front of the precipitation area perfectly coincide. The co-localization of these two fronts is clear (even if not reported in the figure) at any time.

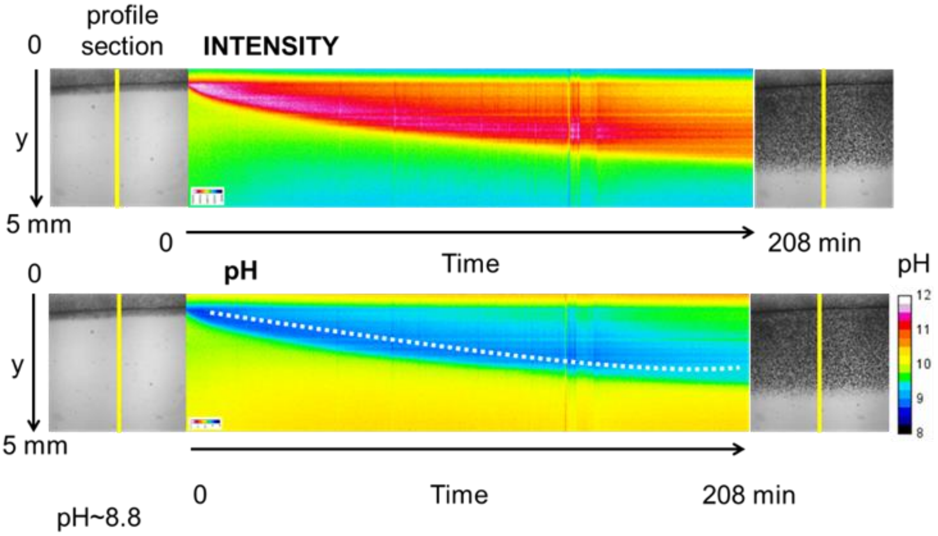

Figure 5.2 Intensity (top, λ_{exc}=460 nm) and pH (bottom) contour plots of the first 5 mm of gel from the interface of the silica gel (containing AY) during calcium diffusion at different times. $CaCl_2$ solution is on the top of the interface, while the gel is in the bottom, where there is the formation of the crystals over time. 5 sec of integration time.

Looking at the fluorescence map, it is possible to observe as the fluorescence front moves over time across the diffusion vector, showing, at least qualitatively, a profile compatible with a diffusional process. We used ImageJ to convert the local intensity signal into pH according to the equation discussed in chapter 2; pH map is shown in figure 5.2. Considered the properties of AY, the observed fluorescence enhancement reveals a local decrease of the pH that is as low as 8.8 value and moves in parallel with the front of growth of the crystals.

This very interesting result demonstrated for the first time the actual correlation between calcium carbonate precipitation and local pH drops in this kind of systems.

Nevertheless, single channel fluorescence detection, although as fast as convenient, presents as mentioned some drawbacks related to possible dis-homogeneity of the distribution of the fluorescent probe in the system as the result of probe diffusion or photobleaching.
This will be demonstrated in the following example.

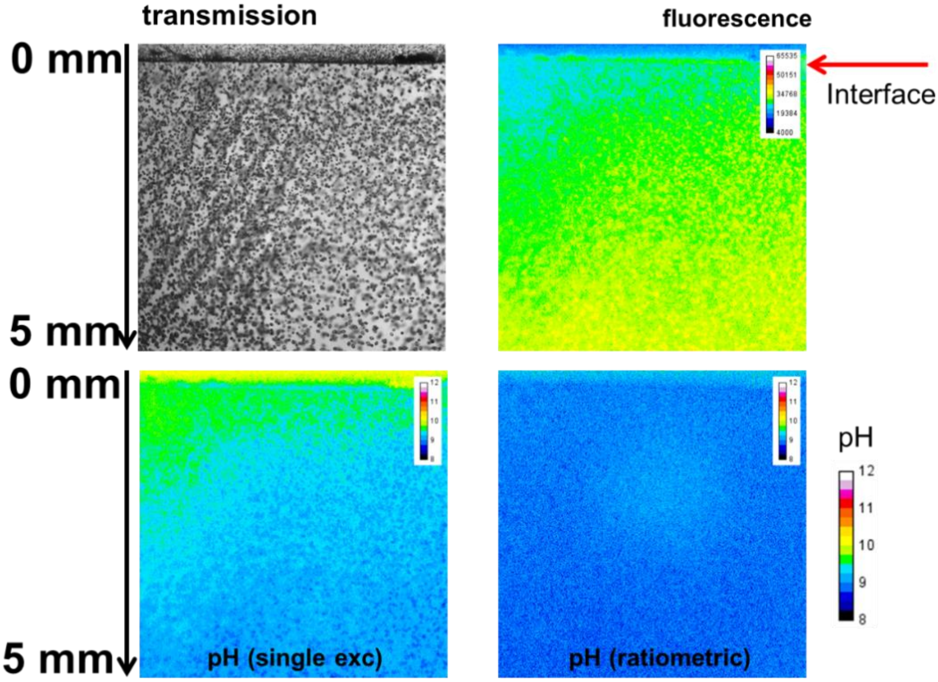

Figure 5.3 The first 5x5 mm^2 area from the interface between $CaCl_2$ and the gel observed in transmission 3 days after injection of the calcium solution (top left). Fluorescence image (λ_{exc}=460 nm) is shown on top right and it was used to calculate the pH (bottom left). This pH map obtained with single excitation is compared with pH measured with dual excitation (400 nm and 460 nm) and ratiometric analysis.

In figure 5.3 it is shown a case of an experiment (similar to the one just discussed) where diffusion of calcium initially occurred in an anomalous way because of an imperfection of the gel. In this case the formation of Liesegang rings not parallel to the interface clearly demonstrates that diffusion occurred in an oblique direction in the initial stages. This is expected to produce also an anomalous diffusion of the pH probe. In fact, fluorescence images acquired upon 460 nm excitation show an unexpected horizontal asymmetry (see figure 5.3) which is still detectable in the pH map calculated from this fluorescence image.

In order to check whether this was or not due to probe diffusion we applied to the same system ratiometric analysis by combining fluorescence images acquired upon two different excitation wavelengths (445/50 nm and 390/18 nm). The resulting pH map is shown in figure 5.3 and it clearly shows a more homogenous pH distribution confirming that the unusual asymmetry previously observed was just the result of probe diffusion.

5.3.2 Long-term pH imaging (ratiometric detection)

Problems related to probe photobleaching and diffusion in fluorescence pH imaging become severe in long-term experiments. For this reason, we decided to use ratiometric detection for long-term analysis. Moreover, we avoided to irradiate the sample continuously but just during fluorescence acquisition at given time intervals. The results obtained, for example 7 days after $CaCl_2$ injection, are shown in figure 5.4. Images on the left show the optical transmittance of the gel in four different positions, moving the sample in the vertical direction (perpendicular to the solution/gel interface), starting from the interface (top). Since the field of view was 5x5 mm^2 the sample was displaced by 5 mm, hence the first image covers the interval from 0 to 5 mm (A), and the others 5-10 mm (B), 10-15 mm (C) and 15-20 mm (D), respectively. These pictures clearly show that, as expected, biomorphic aragonite structures are formed at about 10 mm distance from the interface after 4 days while in the 0-7 mm region only small calcite crystals are observed. At distances longer than 15 mm large calcite elongated crystals appear.

As far as pH is concerned, we used dual excitation (400 and 460 nm) and ratiometric analysis and we obtained the maps shown in false colors in figure 5.4.

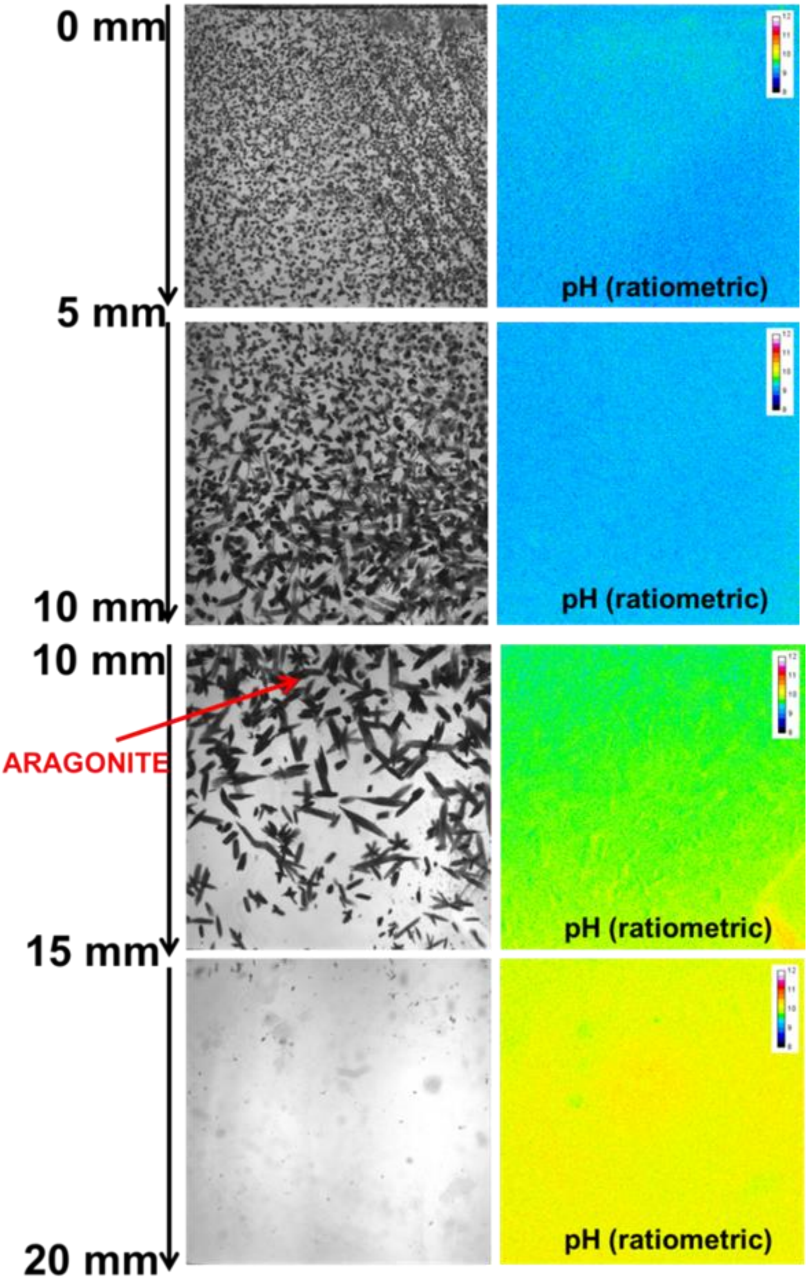

Figure 5.4 Left: Transmission images of the gel at different position with respect to the interface 7 days after calcium injection. Right: pH maps obtained for the same areas with fluorescence ratiometric analysis based on dual excitation (400 nm and 460 nm). AY is used as the pH fluorescent probe.

These maps clearly demonstrate that the pH decrease (to about 9.0), already observed in the short-term experiment discussed in the previous section, propagates deeper in the gel after 7 days. In particular the whole gel section between 0 and 10 mm from the interface presents a homogenous pH around 9.0 while at distance larger than 15 mm the gel still maintains the initial pH 10.5. In the 5-10 mm section a progressive increase of pH from 9 to 10 is detectable and it reveals that the diffusion of the calcium solution has indeed reached this region.

The pH dependence on the distance from the interface can be better analyzed by plotting the fluorescence intensity ratio R (which is the experimental parameter used for pH calculation) or the calculated pH as a function of the distance from the interface. The plots are shown in figure 5.5 and 5.6 respectively and were obtained with the function “plot profile” of ImageJ.

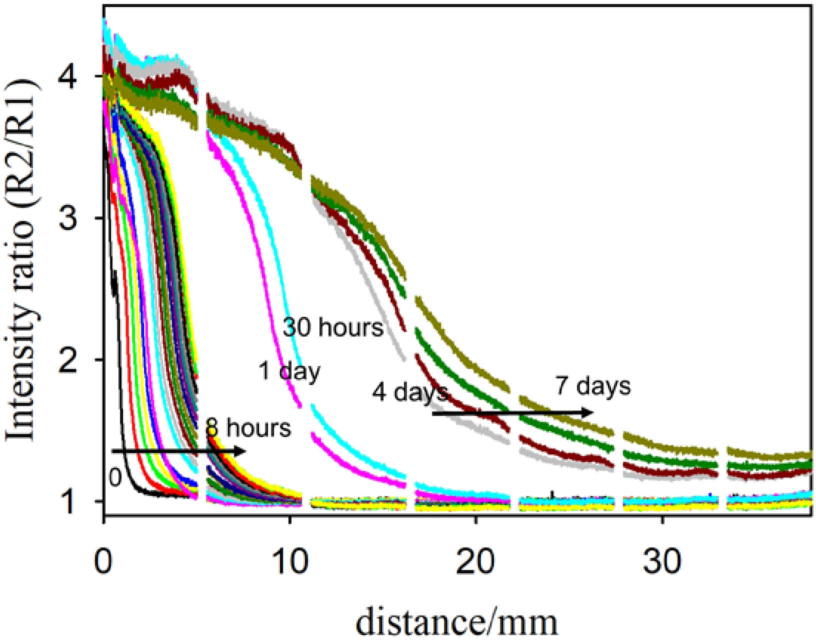

Figure 5.5 Profiles of the ratiometric intensities values measures at 460 and 400 nm excitation in the gel at different times after calcium injection as a function of the distance from the interface.

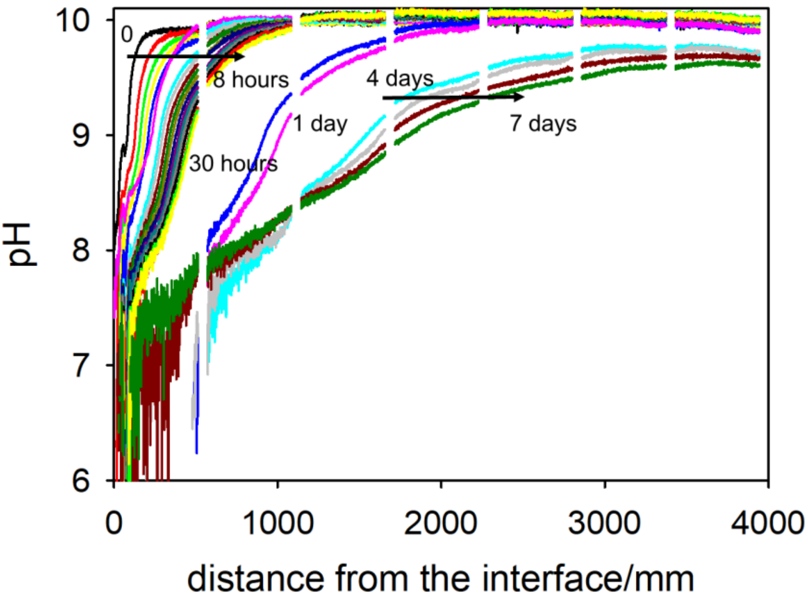

Figure 5.6 Profiles of the pH values obtained by ratiometric fluorescence analysis (λ_{exc}=460 nm as signal; λ_{exc}=400 nm as reference) in the gel at different times after calcium injection of a calcium as a function of the distance from the interface.

As already mentioned for barium biomorphs in chapter 4, considered the broadening of the pH profiles during diffusion into the gel it is convenient to introduce a numeric parameter that identify univocally the position of the front at a given time. We hence defined as $x_{\frac{1}{2}}(t)$ the distance at which the change in the ratiometric signal R is half the total one, which is the difference from the value at the interface R_0 and the one at a long distance R_∞ (in principle infinite, in the real system 5 mm). Figure 5 confirms that indeed after 4 days the front position is at $x_{1/2}$=15 mm.

We would like to stress that, with respect to the results discussed in chapter 4 for barium biomorphs, we observed two important differences in the case of calcium:

1. the **pH drop is much higher in the case of calcium** diffusion. As it can be seen in figure 5.5 the fluorescence ratio becomes as high as 4, corresponding to a complete protonation of AY, while in the case of barium R was at maximum 2.5. As far as the pH is concerned, the minimum pH value reached in the case of barium was about 9.0 and the pH at $x_{1/2}$ is about 9.5. For calcium we

measured a pH as low as 8.0 as minimum and a pH at which $x_{1/2}$ is about 9.0. We believe that this difference is mostly due to the presence of carbonate in the gel used for the growth of aragonite biomorph;

2. the **calcium biomorphs** are formed in a section at about 10 mm from the interface when the **pH become about 9.0**. Barium biomorphs on the other hand are formed at about pH 9.5.

5.3.3 Local and real-time measurement of pH around biomorphs

One of the objective of this thesis was the local analysis of pH in close proximity of the biomorphs during their formation. For this purpose, we used a larger magnification (4X). As we mentioned, ratiometric detection has some limitations when continuous acquisition is required, so for this experiment, aimed to real-time observation, we used single excitation fluorescence.

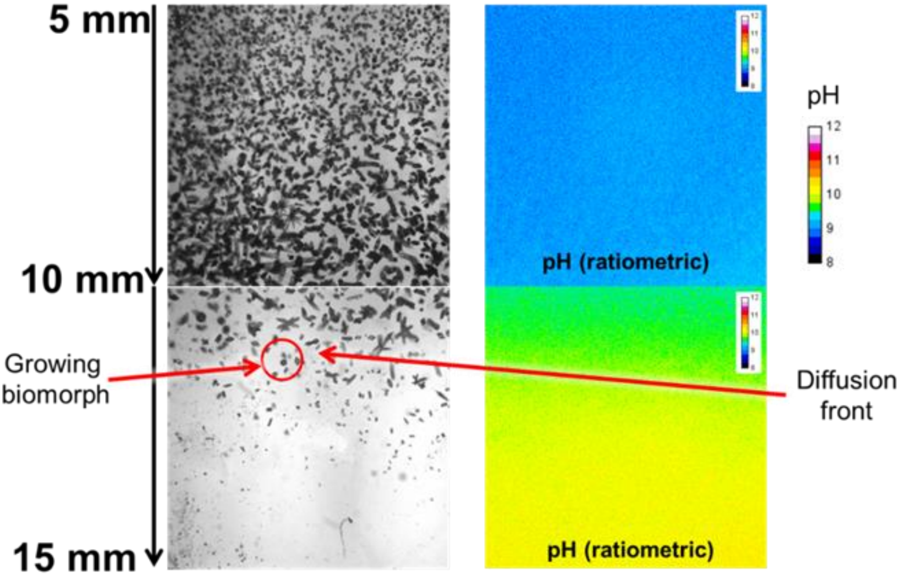

Figure 5.7 Left: Transmission images of the gel at different position with respect to the interface 3 days after calcium injection. Right: pH maps obtained for the same areas with fluorescence ratiometric analysis based on dual excitation (400 nm and 460 nm). AY is used as the pH fluorescent probe.

In particular, during one of the low-magnification (2X) pH mapping experiments, we started to observe the formation of a biomorphic structure at about 11 mm from the interface and 72 h after the injection of calcium. It is interesting to note that the formation of the **biomorph starts at an initial pH of about 9.5**.

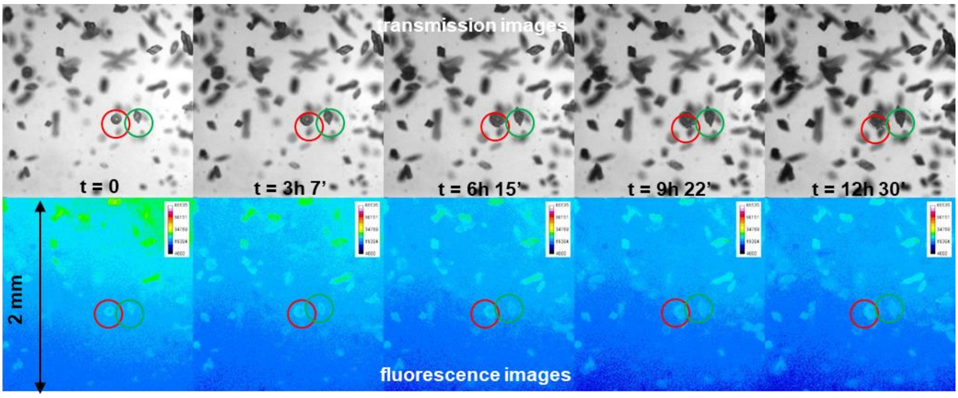

Figure 5.8 Top: Transmission images of the gel at different times at 12.5 mm from the interface 3 days after calcium injection. Bottom: The corresponding fluorescence images (λ_{exc}=460 nm). Red circles surround an aragonite crystal while green circles a calcite one. AY is used as the pH fluorescent probe. Reported times start from 3 days after Ca injection.

Transmission and fluorescence images were acquired for about 3 days simultaneously, every 5 seconds. Some selected frames are shown in figure 5.8. The images on the top show the optical transmittance: the growth of an aragonite biomorph (red circle) and a calcite crystal (green circle) in close proximity can be clearly observed. This situation was very intriguing since gave us the opportunity to understand whether the two processes produces very different local effect on the pH or not. The fluorescence images on the bottom clearly demonstrate that there are no significant differences in the fluorescence intensity around the two structures over time, hence **biomorphic aragonite and non-biomorphic calcite are formed in very similar pH environments**.

We would like to stress that, although **photobleaching** clearly occurs in the gel and it alters to some extent the possible conversion of the fluorescence image into a pH map, it **is irrelevant as soon as the relative comparison of pH is considered** as in this case.

For accurate pH mapping, we measured the pH at the beginning of the experiment (that started as mentioned from 72 h after injection) and at the end (after additional 12 hours) with the ratiometric method. Results are shown in figure 5.9. This figure clearly shows that after 12 hours the diffusion front has moved deeper into the gel and that the local pH is changed from 9.5 to 9.0.

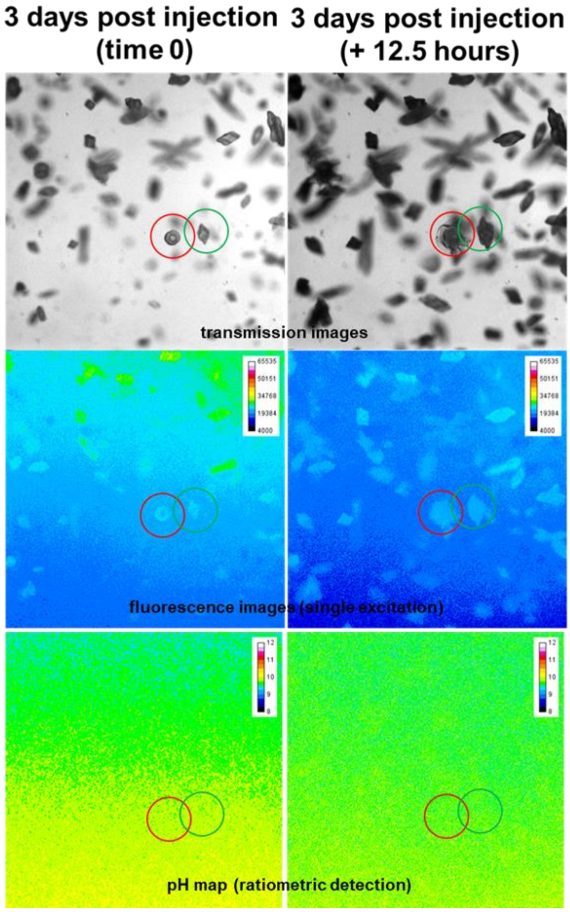

3 days post injection (time 0)

3 days post injection (+ 12.5 hours)

Figure 5.9 Transmission (top), single excitation fluorescence images (center) and ratiometric pH map (bottom) of the growing aragonite biomorph (red circled) close to a growing calcite crystal (green circled), at time 0 and after 12 hours and a half after 3 days from the injection of $CaCl_2$.

In order to further increase the resolution in the pH local detection we increased the magnification to 10X and preformed again the ratiometric measurements, obtaining the images of figure 5.10 for the calcium aragonite biomorphic structures and figure 5.11 for the elongated calcite crystals.

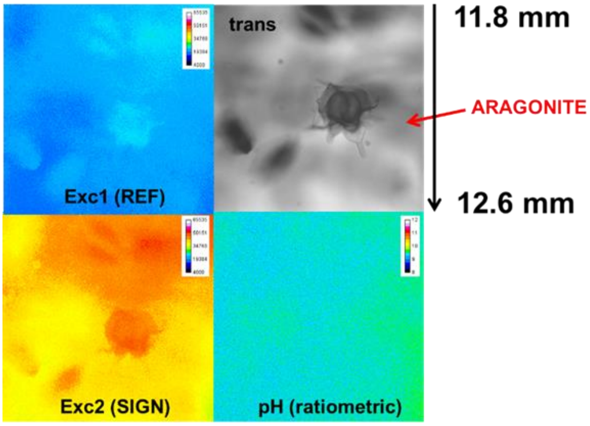

Figure 5.10 Higher magnification of aragonite biomorphic crystal after 18 hours and a half after 3 days from the injection of $CaCl_2$ in fluorescence mode, both with the reference excitation and the signal one and correlated pH map derived from the ratiometric calculation.

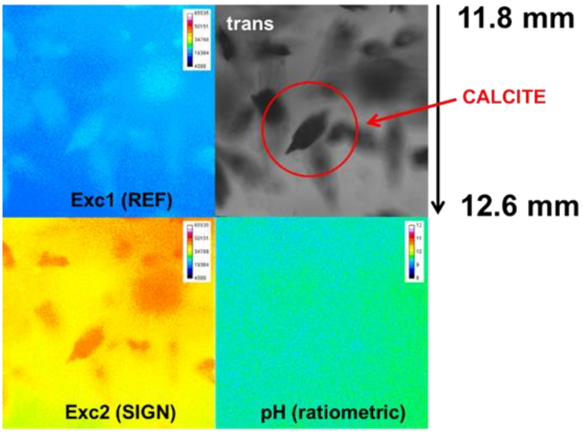

Figure 5.11 Higher magnification of elongated calcite crystal after 18 hours and a half after 3 days from the injection of $CaCl_2$ in fluorescence mode, both with the reference excitation and the signal one and correlated pH map derived from the ratiometric calculation.

Also these magnified images demonstrate that there is no relevant local pH variation and that pH around the crystal is quite homogeneously and close to 9.0. Moreover, similar results are obtained both for aragonite and calcite crystals.

5.3.4 Estimation of the diffusion rate coefficient

Fluorescence and intensity profiles discussed in the previous sections are related to diffusion of chemical species from the solution into the gel.

In order to better characterize these diffusive processes, we analyzed the diffusion plots in a more quantitative way in order to estimate the diffusion coefficients of the diffusing species. In particular, using the Fick's law in the case of 1D diffusion into a homogenous medium from a reservoir at concentration c_0 we expect the diffusion profile to evolve in time according to the following equation:

$$\mathrm{c} = c_0\left(1 - erf\,\frac{x}{2\sqrt{Dt}}\right),$$

where c is the concentration of the tracer at a distance x from the surface, t is time of the diffusion, and D is the diffusion coefficient.

Hence if we define $x_{\frac{1}{2}}(t)$ as the distance at which $\mathrm{c} = \frac{c_0}{2}$ we obtain the following simple equation:

$$x_{\frac{1}{2}}(\mathrm{t}) = 0.954\sqrt{Dt}.$$

Hence we plotted $x_{1/2}$ as a function of time in figure 5.12.

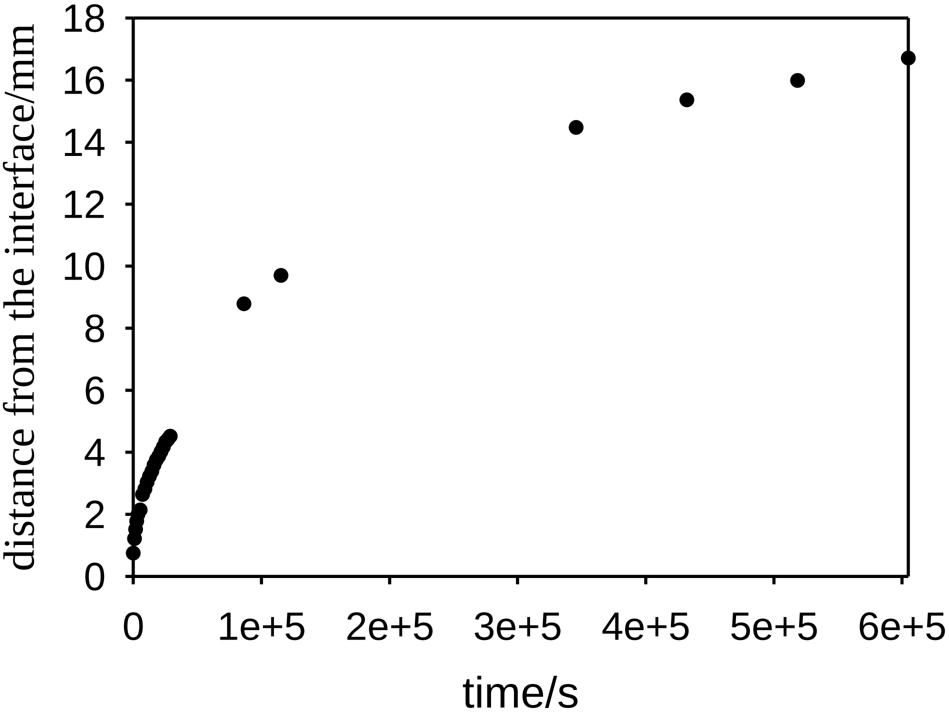

Figure 5.12 Plot of $x_{1/2}$ as the distance at which $c = \frac{c_0}{2}$ as a function of time.

In order to better visualize whether the data of figure 5.12 were compatible with a pure diffusional behavior, we plotted the square of $x_{1/2}$ as a function of time (figure 5.13): in the case of diffusion a linear plot is expected.

The data shown in figure 5.13 clearly presents a linear dependence, at least for the first 30 hours. For longer times, on the other hand, the model adopted for 1D diffusion stops to be acceptable because the diffusion distance becomes comparable to the gel length and the calcium solution is no more and ideal reservoir.

Hence we fitted this first part of the plot and got a diffusion coefficient D=1x10^{-3} mm^2/s. This correspond to a diffusion coefficient 1x10^{-9} m^2/s which is of the typical order of magnitude of diffusing ionic species.

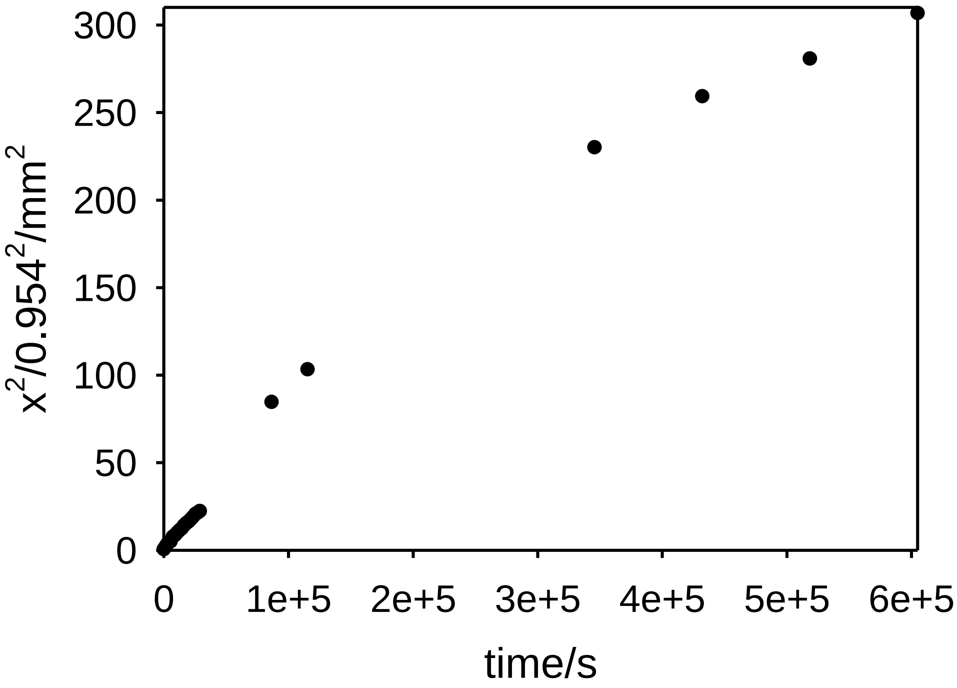

Figure 5.13 Plot of the square of $x_{1/2}$ as the distance at which $c = \frac{c_0}{2}$ as a function of time.

5.4 Conclusions

In this section, we described the pH mapping based on the use of a fluorescent probe in the case of calcium gel-grown biomorphs. The method for the preparation of these structures is quite similar to the one discussed in chapter 4 for barium biomorphs, with the exception that the silica gel is enriched of carbonate.

Two forms of $CaCO_3$ are produced in different positions with respect to the interface and they are organized in bands or stripes perpendicular to the calcium diffusion direction. However, only aragonite gives characteristic flower like biomorphic structures that appear in a single band at a distance of 10-15 mm from the interface with the calcium solution. Both at shorter and longer distances elongated non biomorphic calcite crystals are formed.

As already mentioned, photobleaching and pH probe diffusion are very critical, so we used ratiometric imaging and, for improving spatial resolution and sensitivity, also image stitching. We acquired a set of 3 image for each time (t) of observation: transmission (T(t)), fluorescence at EXC1 (F1(t)) and fluorescence at EXC2 (F2(t)) at different distances with respect to the interface to cover a total area of 25x5 mm^2.

For short-term analysis, we decided to use a simple single channel fluorescence detection (non ratiometric) combined to transmission one. This kind of setup allowed us to follow the evolution of morphology and pH simultaneously almost in real time. Considering that precipitation is due to the diffusion of calcium into the gel and the formation of $CaCO_3$ crystals, for the first time we were able to correlate calcium carbonate precipitation and local pH drops in this kind of systems.

Problems related to probe photobleaching and diffusion in fluorescence pH imaging become severe in long-term experiments. For this reason, we decided to use ratiometric detection for long-term analysis. As expected, biomorphic aragonite structures are formed at about 10 mm distance from the interface after 4 days while in the 0-7 mm region only small calcite crystals are observed. At distances longer than 15 mm large calcite elongated crystals appear.

We would like to stress that, with respect to the results discussed in chapter 4 for barium biomorphs, we observed two important differences in the case of calcium:

1. the pH drop is much higher in the case of calcium diffusion. As it can be seen in figure 5.5 the fluorescence ratio becomes as high as 4, corresponding to a complete protonation of AY, while in the case of barium R was at maximum 2.5. As far as the pH is concerned, the minimum pH value reached in the case of barium was about 9.0 and the pH at $x_{1/2}$ is about 9.5. For calcium we measured a pH as low as 8.0 as minimum and a pH at which $x_{1/2}$ is about 9.0. We believe that this difference is mostly due to the

presence of carbonate in the gel used for the growth of aragonite biomorph;

2. the calcium biomorphs are formed in a section at about 10 mm from the interface when the pH become about 9.0. Barium biomorphs on the other hand are formed at about pH 9.5.
3. the formation of the biomorph starts at an initial pH of about 9.5.

there are no significant differences in the fluorescence intensity around the two structures over time, hence biomorphic aragonite and non-biomorphic calcite are formed in very similar pH environments.

Increasing the magnification, we demonstrated that there is no relevant local pH variation and that pH around the crystal is quite homogeneously and close to 9.0. Moreover, similar results are obtained both for aragonite and calcite crystals.

Considering that fluorescence and intensity profiles are related to diffusion of chemical species from the solution into the gel, we decided to better characterize these diffusive processes. Hence we analyzed the diffusion plots in a more quantitative way to estimate the diffusion coefficients of the diffusing species, in particular, using the Fick's law in the case of 1D diffusion into a homogenous medium. We found out that our data clearly present a linear dependence, at least for the first 30 hours. For longer times, on the other hand, the model adopted for 1D diffusion stops to be acceptable because the diffusion distance becomes comparable to the gel length and the calcium solution is no more an ideal reservoir. Fitting the first 30 hours data we got a diffusion coefficient $D=1x10^{-3}$ mm^2/s. This corresponds to a diffusion coefficient $1x10^{-9}$ m^2/s which is of the typical order of magnitude of diffusing ionic species.

5 References

[1] G. Zhang, J. M. Delgado-Lopez, D. Choquesillo-Lazarte, J. M. Garcia-Ruiz, *Crystengcomm* **2013**, *15*, 6526-6532.

[2] M. Kellermeier, E. Melero-García, F. Glaab, J. Eiblmeier, L. Kienle, R. Rachel, W. Kunz, J. M. García-Ruiz, *Chemistry – A European Journal* **2012**, *18*, 2272-2282.

[3] G. Zhang, J. M. Delgado-Lopez, D. Choquesillo-Lazarte, J. M. Garcia-Ruiz, *Cryst Growth Des* **2015**, *15*, 564-572.

[4] M. Kellermeier, F. Glaab, E. Melero-García, J. M. García-Ruiz, in *Methods in Enzymology, Vol. 532* (Ed.: J. J. D. Yoreo), Elsevier Inc., **2013**, pp. 225-256.

6 Silica gardens

6.1 Introduction

As described more in detail in chapter 1.2, silica gardens are self-assembled hollow structures forming from the precipitation of an inorganic membrane at the interface between a metal and a silicate solution. Generally, a hydrated metal salt seed is immersed in a sodium silicate solution forming a semipermeable membrane and precipitates in contact with the cations of the internal solution at the pH of the internal solution.

The colloidal membrane is formed during the early stages of seed dissolution, when the metal ions readily react with the aqueous sodium silicate:

$$2M^{n+}_{(aq)} + nNa_2SiO_{3(aq)} \rightarrow 2nNa^{+}_{(aq)} + M_2(SiO_3)_{n(s)}.$$

Because of the presence of the membrane, the exchange of ions and molecules between the outer silicate solution and the inner metal salt is partially restricted. Due to the high concentration of the inner solution, an osmotic pressure occurs across the membrane, which constantly ruptures and re-precipitates across the front between the different fluids, while buoyancy forces make the inner solution flows up.

The inner solution has a lower pH than the external one: thus, when the silicate of the external solution encounters the lower pH medium, it precipitates, while the metal cations of the inner solution precipitate in the inner part of the wall because of the high pH of the external solution, forming metal hydroxides:

$$mM^{n+}_{(aq)} + nOH^{-}_{(aq)} \text{ -> } M_m(OH)_{n(s)}.$$ [1]

Although several hypotheses have been postulated about the diffusion and precipitation processes in silica garden, a complete understanding of the chemical behavior of these systems is still missing especially as far as the local changes in concentration of the different species over time are concerned. We found out that the very complicate dynamics of formation and growth of chemical gardens can be investigated with a simple approach using optical and fluorescence microscopy. In particular, we succeed in preparing the membrane at the interface between two thin layers (~0.1 mm) of metal and silica solutions and in investigating in real time the processes of diffusion though the membrane in the microscale range. After testing several different metals, we focused on **Fe(III)** and **Mn(II)** silica gardens that, as it will be discussed below, offer important advantages for our experimental platform.

6.2 Brief description of the set up

The formation and evolution of the silica gardens was investigated by optical microscopy both in transmission and fluorescence mode. For fluorescence both wide field and laser scanning confocal setups were exploited.

In all cases the samples were placed **horizontally** on the stage of the microscopes, using a set up for the formation of the silica gardens slightly different from the conventional one. In general, we prepared thin optical cells placing the reactants between two microscope slides, sometimes separated by a tape as a spacer in order to control the actual cell thickness. In some cases, depending on the kind of experiment, the type of microscope and the kind of objective used, the upper slide or both the slides were thin (0.1 mm) coverslips.

The use of concentrated solution (typically saturated) of metal ions in place of crystal seeds allowed us to achieve a good **control** and **reproducibility** of the **membrane formation** and gave sample more suitable for investigation with optical microscopy. Hence, in general, the reactants used in the experiments were: a **saturated metal ion solution** (here we describe the cases of $FeCl_3$ and $MnCl_2$) and a **sodium silicate solution** containing a fraction of water that depended on the type of metal salt used.

We performed **two different kinds** of experiments that gave complementary information about the mechanism of formation and evolution of silica garden.

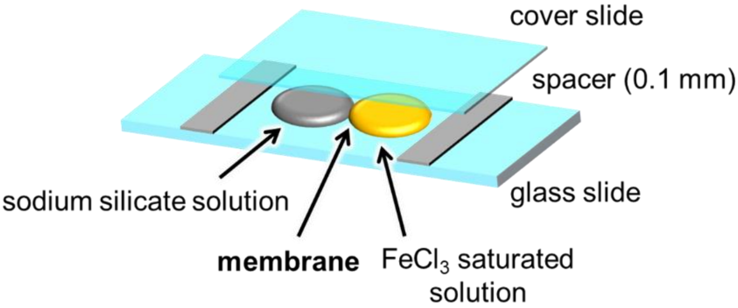

Figure 6.1 Schematic representation of the cassette used for the experiments with $FeCl_3$ and sodium silicate solution.

Experiment 1: Investigation of the diffusion through the membrane

In the first experiment, the inorganic membrane was formed at the interface between an **iron solution drop** (10 µL) and a **silicate solution drop** (10 µL) which were interposed between two glass slides separated by a spacer (0.1 mm thick). In this arrangement, the contact section of the two drops is about 5 mm long while the remaining border of the drop (not in contact with the glass) is exposed to atmospheric air (figure 6.1). Hence, the **inorganic membrane is open** and it does not undergo to any mechanical pressure. In this experiment we observed changes in the optical images, acquired with a camera mounted on the microscope, because of the **local** formation of precipitates (mostly hydroxide and silica). We correlated the precipitation to the diffusion of ionic species (in particular OH^-) though the membrane.

We would like to stress that in this experiment actually **the growth and propagation of the membrane, after initial formation, do not occur**, since these processes are originated by osmotic pressure and buoyancy whose effects are minimized in the selected setup.

For this experiment we focused on $FeCl_3$ silica garden since Fe(III) ions and hydroxide are yellow-brown colored and they can be easily detected at the optical microscope and distinguished from the sodium silicate, which, on the contrary, is colorless.

Experiment 2: Investigation of the mechanism of growth of micro-tubes in quasi 2D silica garden with fluorescent probes

In the second kind of experiment we explored the local changes of the chemical properties (and in particular of pH) in silica gardens during their growth and propagation. Silica gardens are a typical example of compartmentalized system were two media (the metal solution **MS** and the silicate solutions **SS**) are separated by a membrane.

One of the most interesting feature of silica gardens is the growth of the self-assembling membrane in the form of tubes. The actual mechanism of propagation of these tubes is widely debated and its detailed investigation definitively needs new tools suitable to characterize the chemical evolution of silica gardens in real time and space. In particular, it is known that during the membrane growth the **MS** contained inside the tubes is ejected out into the external **SS** causing the continuous growth of the tube at the interface. Nevertheless, the actual dynamic of this process is not well established and the processes occurring in the **MS** jet needs clarification. Here we use optical and fluorescence microscopy to investigate the **physical-chemical evolution of the jet during tube growth**. For doing this we labelled the solution with pH sensitive fluorescent probe and exploited fluorescence to:

1) investigate the possible, and still largely disregarded, mixing of the **MS** and **SS** solution in the jet;
2) measure (at least qualitatively) **changes of pH in the jet** and in the surrounding regions;
3) detect possible changes in the **pH inside the tube** or in proximity of the external surface of the tubes after their formation.

Our interest in pH is due to the consideration that the MS and the SS present a radically different pH, being **acidic** the former and **strongly alkaline** the latter. Moreover, the most important chemical processes involved in silica garden growth, like silica, metal silicate and hydroxide formation, are expected to have a large effect on local pH.

For these experiments, that exploit the fluorescence of molecular probes excited with visible light, we preferred metal ions that form **un-colored** or weakly colored species (as ions or precipitate) but that, in the meantime, could produce **tubular structures** in the micro-scale suitable for our experimental set-up. After several tests, we chose $MnCl_2$ as the best candidate.

For the experiments a droplet of saturated metal solution (2 µL) was deposited on the top of a glass coverslip (24x24 mm^2) while the **SS** (100 µL) was dropped on a microscope glass slide (75x25 mm^2). Hence the coverslip was reversed top-down and placed on the larger glass slide, immerging the smaller MS drop into the larger SS one (the two slides were spaced with a plastic tape 0.1 mm thick). In this experiment, differently to what described in the previous section (experiment 1), the **MS droplet was completely surrounded**, being either in contact with the SS or with the glass. This led to the formation of a c**losed membrane**. The increasing of the internal osmotic pressure led to local membrane rupture and to the **formation of tubes** that, because of the geometry of the system, could **grow only horizontally**. We followed the growth by time-lapse acquisition using a CCD camera and detecting simultaneously the transmission and fluorescence images. The pH fluorescent probe (**HPTS**) was dissolved either in the MS, in the SS or in both solutions depending on the experiment.

6.3 Experiment 1: Investigation of the diffusion through the membrane

As mentioned in the previous section, we chose $FeCl_3$ as optimal candidate for the investigation of membrane permeation. For this experiment a droplet (10 µL) of the saturated metal salt solution (MS) was placed on a microscope slide near (about 2 mm distance) to a droplet (10 µL) of sodium silicate solution (SS) (Sigma Aldrich 27% SiO_2 and 7% Na_2O, diluted 1:1, v:v with water). Then, the glass was covered with another microscope slide, paying attention to not mix the two solutions but making them get in touch just on the border of the two drops, avoiding in this way solution mixing and membrane rupture (a tape 0.1 mm thick was used as a spacer).

With this setup there are some **advantages, for diffusion analysis**, with respect to the usual vertical growth of silica gardens: i) the system is **not affected by osmotic pressure** because both the solutions can expand, and, ii) due to the very small thickness of the film that can be placed between the two glass slides, the **buoyancy has no effect**.

The changes in **optical transmittance** of the system were acquired at different times after membrane formation with the optical microscope with a 4x objective and a color CCD camera.

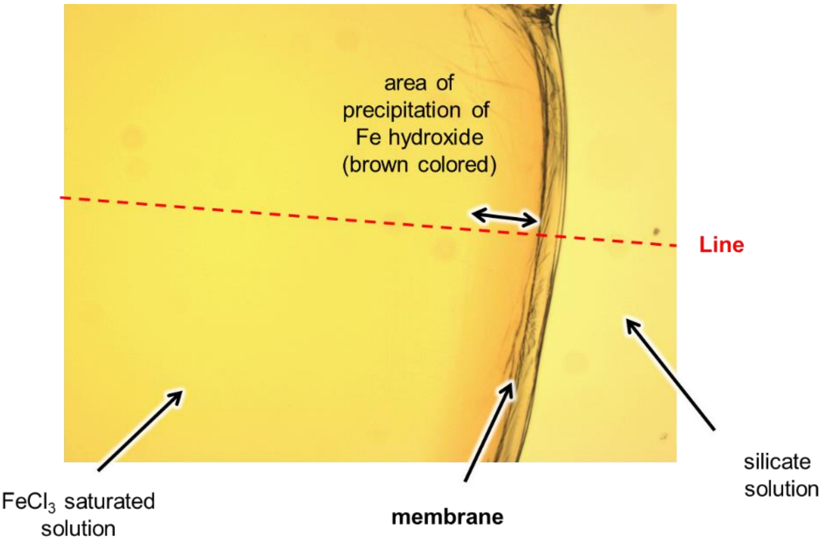

Figure 6.2 Optical transmission image of the membrane formed at the $FeCl_3$/silicate interface. Size: 1.43 mm (width), 1.07 mm (height). Thickness 0.1 mm. The red line was selected as vector for the diffusion analysis.

The first image, that was acquires in a typical experiment 1 minute after the sample preparation, is shown in figure 6.2. A thin **brown membrane** can be clearly observed in the region of contact of the **MS** (on the left) and the **SS** (on the right). The membrane is about 5 mm long and the part visible in figure 6.2 is about 1 mm long. The **iron solution is yellow** because of the presence of the metal ion while the silicate in uncolored. Just after one minute a **brown precipitate** is formed in proximity of the membrane on the MS side.

In order to analyze the changes in the system **over time**, we preferred to analyze just the **blue component** of the RGB images because $FeCl_3$ and Fe^{3+} hydroxides, that are expected to form in the system, have a yellow-brownish color: hence they absorb light mostly in the blue region and they can be easily detected using the blue component of the adsorbed light. Some of the acquired images (blue component of the RGB picture) are represented in fig. 6.3, where some frames, equally temporally separated (Δt=10 sec), are shown over 90 minutes. In order to enhance the transmission difference in the monochromatic images (as mentioned, just the blue component is considered), in figure 6.3 images are converted into false colors. White-pink color of the SS indicates very high transmission, the iron solution partially absorbs the blue light (orange indicates moderate transmission). Formation of the precipitates leads to a decrease of the transmittance (yellow bands).

The images of figure 6.3 demonstrate that the darker region, initially formed in close proximity of the membrane and corresponding to the formation of a gelly, brownish precipitate (image A) inside the metal salt solution, **propagates inside the iron solution over time** (images B and C). This behavior is due to the diffusion of OH^- ions from the silicate solution through the membrane that brings to the precipitation of $Fe(OH)_3$, according to the following reaction:

$$FeCl_3 + 3OH^- \rightarrow \downarrow Fe(OH)_3 + 3Cl^-.$$

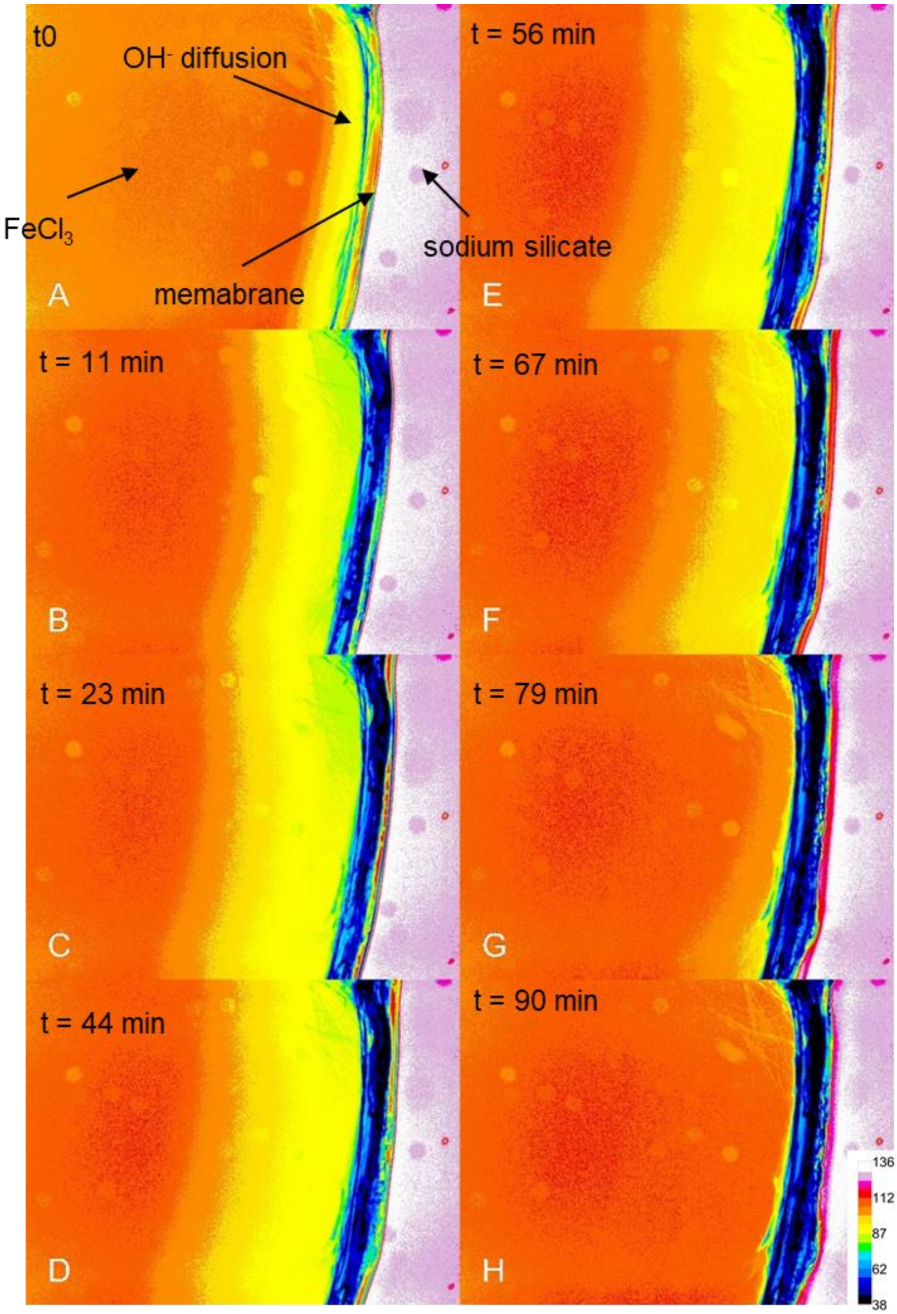

Figure 6.3 Blue component of the transmission images (in false colors) at different times after membrane formation of $FeCl_3$/silicate system. Size: 1.43 mm (width), 1.07 mm (height).

The decrease of transmission can be hence correlated to the precipitation of iron insoluble hydroxides. Pictures shown in figure 6.3 hence demonstrate that the **OH^- ions diffuse through the membrane and cause a propagation of the precipitation** in the MS.

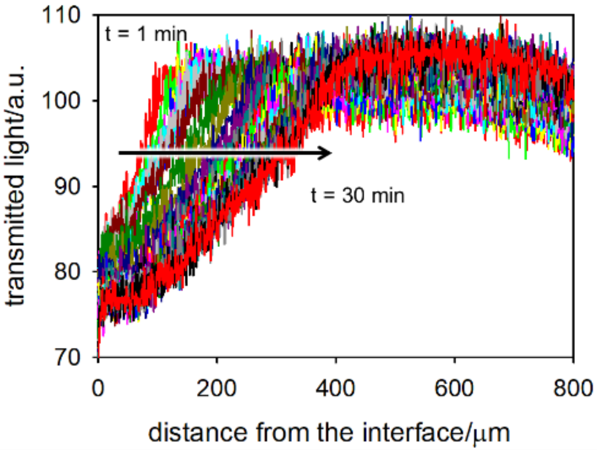

Figure 6.4 Optical transmission profiles along one line chosen for the analysis (see figure 6.2) perpendicular to the membrane of $FeCl_3$/silicate system sample over time during the first 30 minutes after membrane formation.

In order to analyze the process, we chose a **line vector** in the system (see figure 6.2) **perpendicular to the membrane** in the SS to MS direction. Hence, we analyzed the time-lapsed images to get the transmission profiles as a function of the distance from the membrane at increasing delay time, as shown in figure 6.4, using the function “profile plot” of ImageJ. Such figure clearly shows that the precipitation front moves far from the membrane during the first 30 minutes of acquisition.

Quite surprisingly after 30 minutes the **precipitate formed starts to re-dissolve**. As shown in figure 6.5, in fact, the transmission profile moves back towards the membrane in the time interval between 30 and 90 minutes and finally the precipitate completely disappears from the MS.

This result is quite surprisingly, and it may be explained in two ways:

1) diffusion of OH^- leads to the formation of **soluble iron hydroxides, like $Fe(OH)_4^-$**.

2) diffusion of OH^- is stopped and re-dissolution occurs due to the **diffusion of the still acidic Fe^{3+} solution** (not yet reached by OH^-).

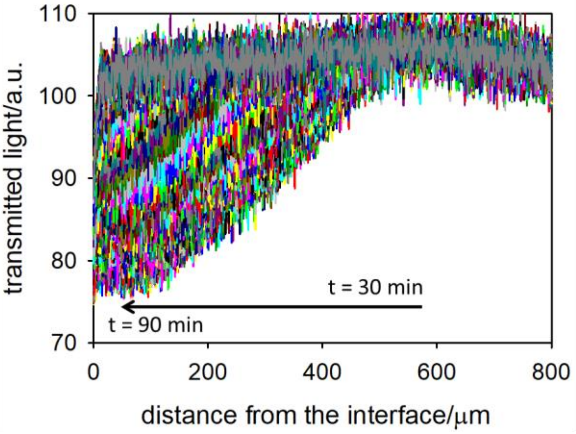

Figure 6.5 Optical transmission profiles along one line chosen for the analysis (see figure 6.2) perpendicular to the membrane of $FeCl_3$/silicate system sample over time: in the 30-90 minutes interval after membrane formation.

Considered that re-dissolution starts form the iron solution side rather than from the membrane, we concluded that indeed the **OH^- diffusion through the membrane is strongly slowed down after 30 min**.

The reason for this can be clearly found by observing the pictures of figure 6.3. Over time **thickening of the membrane is observed**, and the formation of several layers on the membrane is observed too.

We would like to stress that both MS and SS are very concentrated solutions. Considering that the commercial sodium silicate solution contains an amount of silica (SiO_2) 27% v/v and more or less 8% v/v of Na_2O, the molar concentration of SiO_2 is 6.0 M while the one of Na_2O is 1.6 M. This solution was diluted 1:1 v:v with water, hence in our system the concentrations are about 3.0 M for SiO_2 an 0.8 Na_2O (corresponding to NaOH 1.6 M). The iron solution has a concentration about 6.0 M.

Silica in the solution is solubilized as silicate but **SiO_2 precipitates upon acidification of the solution**. Hence the thickening of the membrane is due to two main factors:

1) diffusion of OH^- from SS to MS through the membrane causes a local decrease of pH close to the external (SS exposed) side of the membrane. As a consequence, **SiO_2 precipitation occurs**;
2) Fe(III) diffuses through the membrane and precipitates as silicate on the external SS exposed side.

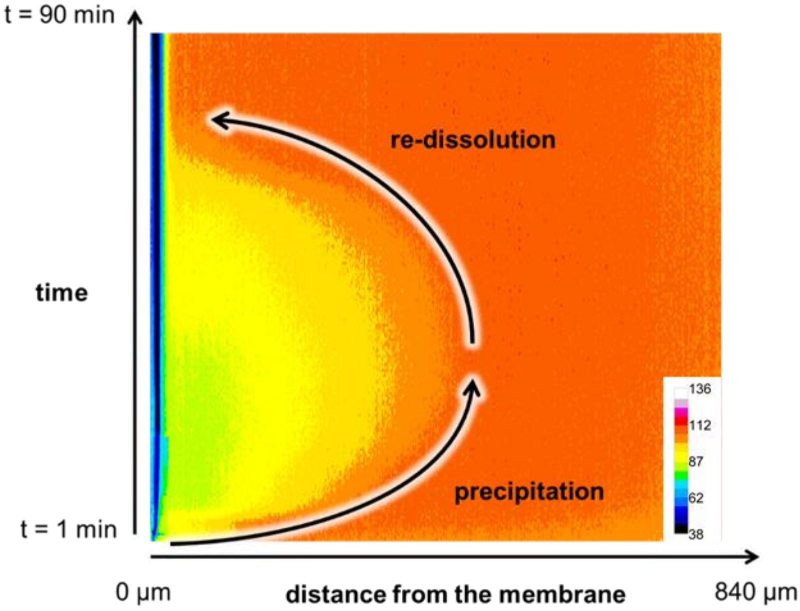

Figure 6.6 Contour map of the intensity profiles along the line shown in fig. 7.3.3 in false colors.

The whole precipitation-redissolution process is summarized in figure 6.6. In particular all the transmission profiles T(x) (where x is the position along the diffusion line shown in figure 6.2, taking the membrane as 0 point and the SS toward MS as the direction) acquired at different times t were merged in a single array of data to give transmittance as a function of both position and time, T(x,t). This data array is represented as contour plot in the false color figure 6.6, where green and yellow regions represent a decrease of transmittance with respect to the MS (orange) and hence the formation of precipitate.

In order to better characterize this diffusive process, we analyzed the diffusion plots in a more quantitative way in order to estimate the diffusion coefficients of the diffusing species. In particular, using the Fick's law in the case of 1D diffusion into a homogenous medium from a reservoir at concentration c_0 we expect the diffusion profile to evolve in time according to the following equation:

$$\mathrm{c} = c_0 (1 - erf\,\frac{x}{2\sqrt{Dt}}),$$

where c is the concentration of the tracer at a distance x from the surface, t is time of the diffusion, and D is the diffusion coefficient.

Hence, if we define $x_{\frac{1}{2}}(t)$ as the distance at which $\mathrm{c} = \frac{c_0}{2}$, we obtain the following simple equation:

$$x_{\frac{1}{2}}(\mathrm{t}) = 0.954\sqrt{Dt}.$$

This was the fitting curve I used for the values below:

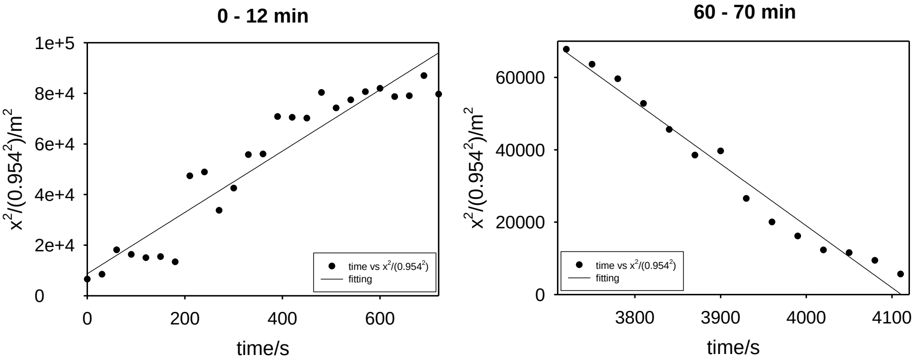

Figure 6.7 Fitting of the first 12 minutes of the collected film on the left, and of the minutes between the 60th and the 70th minute on the right.

The diffusion coefficient D derived from the two fitting are quite similar: 1.2 10^{-10} m^2/s for the first 12 minutes and $1.7 \cdot 10^{-10}$ m^2/s for the second graph, which are coherent to each other. In the literature it can be found that the diffusion coefficient for OH^- ions in water is 5.270 10^{-9} m^2/s, that is 50 times higher than the one I found: this means that the process is controlled not just by the diffusion but also by **the precipitation of the hydroxides**.

6.4 Experiment 2: Investigation of the mechanism of growth of micro-tubes in quasi 2D silica garden with fluorescent probes

6.4.1 Introduction

In this experiment we used optical (transmission) and fluorescence microscopy to investigate possible **pH changes** in the MS and SS **during and after the formation of hollow tubes**. As mentioned, in fact, although one of the most interesting feature of silica garden is the growth of the self-assembling membrane in the form of tubes, the actual **mechanism of propagation** (and in particular the modality of interaction of the MS and SS in the process) of these tubes is still debated. The actual **permeability** properties of these tubular membranes also need further investigation. Considered that MS and SS present as an important characteristic property a very different pH (**MS is acidic while SS is alkaline**), we propose here the **use of a fluorescent pH probe** as a general method for analyzing the evolution of the local chemical properties of the two solutions. We would like to stress that **all the most important chemical reactions** involved in the formation of silica garden such as **precipitation of metal** silicates, hydroxides, etc., and **formation of silica** have an effect on pH and are **pH dependent**. Solubility of metals themselves and hence **local metal ion concentrations are pH dependent**. Hence local **pH analysis gives indirect information about several local chemical parameters**.

It is known that, during the tubular membrane growth, the **MS** contained inside the tubes is ejected out into the external **SS,** causing the continuous growth of the tube at the interface. Nevertheless, the actual dynamic of this jet propagation is not well established and the processes occurring in the **MS jet** need clarification. Here we propose the use of optical and fluorescence microscopy to investigate the **physical-chemical evolution of the jet during tube growth**. For doing this we labelled the solution with pH sensitive fluorescent probe.

Despite the apparent simplicity, this approach was very challenging: in **very concentrated metal solutions the response of fluorescent pH probes is strongly altered**. In particular, many metal ions that form silica gardens like Fe(III), Cu(II), Co(II) and Cr(III) are well known **quenchers of the fluorescence.** These metals typically form in water solution **colored complexes** with absorption bands corresponding to low energy electronic transitions. Hence these complexes are **potential acceptors in energy transfer processes** involving the pH probe as energy donor. Moreover, the same complexes, because of their **redox potentials**, can be easily either reduced or oxidized by the excited pH probe, quenching the fluorescence via **electron transfer processes**.

These quenching processes are very efficient when the pH probe, for its chemical feature, can bind the metal ions forming quenched complexes (**static quenching**). Static quenching is effective even at very low concentrations of metal ions and it can be avoided by **properly selecting the pH probe (and the metal ion)**. To avoid additional problems in fluorescence detection due to the **optical filtering** effect of intensely colored metal ions **we focused on Mn(II)** which gives pale pink saturated solution (about 6.0 M) Even more importantly we will show that **Mn(II) forms very reproducible tubular silica gardens** in the experimental conditions necessary for optical imaging. After testing several pH probes, we found out that **HPTS does not bind to Mn(II)**, so we adopted this probe for our experiments. As important additional features HPTS presents an ON/OFF response to protonation (when excited at 460 nm) and a pK_a of 7.4, hence it is suitable to detect pH increase in the MS responding with an enhancement of the fluorescence.

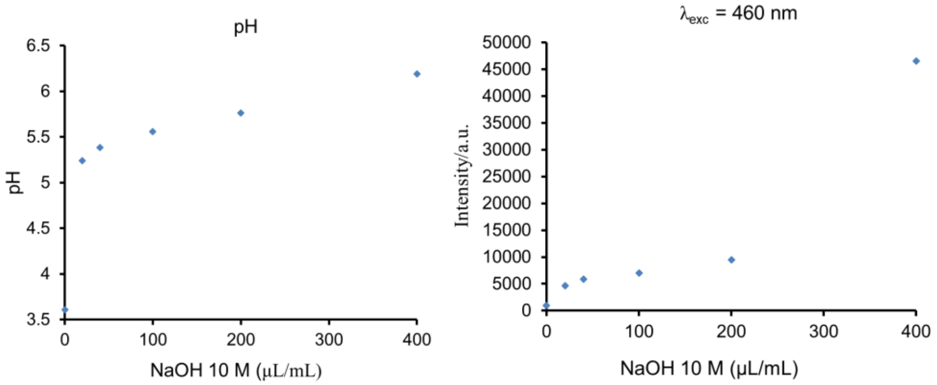

Figure 6.8 Left: pH of 1 mL of saturated $MnCl_2$ solutions (about 6.0 M) upon addition of different amount of NaOH 10 M. Right: fluorescence intensity of HPTS in the $MnCl_2$ saturated solution (about 6.0 M), collected by wide field fluorescence microscopy at 460 nm excitation measured during the NaOH addition.

Nevertheless, at concentration as high as 6.0 M of Mn(II), quenching processes, different from static quenching, are expected to occur. Free metal ions in fact can diffuse and collide with the excited HPTS molecules causing its **dynamic quenching**. The efficiency of the dynamic quenching depends on a quenching constant (limited by the diffusion rate) and on the excited state lifetime of the fluorophore (6.0 ns for HPTS), according to the Stern-Volmer equation. In particular, the use of a probe with a quite short excited state lifetime (as HPTS) allows to reduce the effect of dynamic quenching. Preliminary experiments showed that indeed **HPTS fluorescence is extremely weak in saturated $MnCl_2$ solutions**. Nevertheless, this weak fluorescence is due at least in part to the **pH of the solution**, which is about 3.6, but also to **dynamic quenching**. We hence wondered if we could **discriminate the effect of the pH and the Mn(II)** concentration on the fluorescence of HPTS. For this reason, we added NaOH to the solution to increase the pH and measured the fluorescence response of HPTS as a function of pH (measured with a pH meter). The plot of pH as a function of the added volume of 10 M NaOH solution (to 1 mL of $MnCl_2$ solution) is shown in figure 6.8 (left).

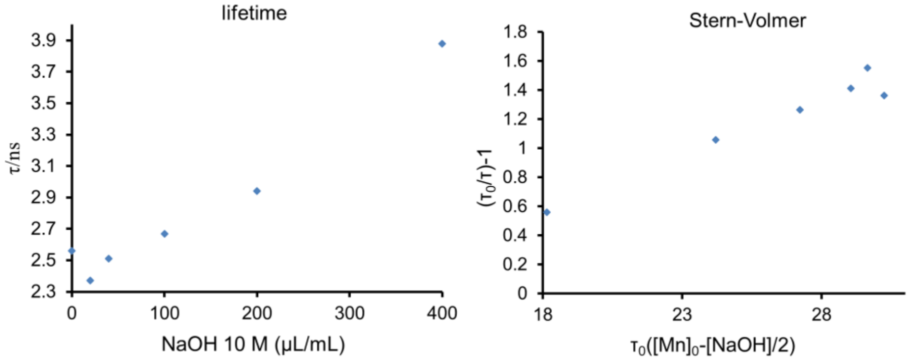

Figure 6.9 Excited state lifetimes of 1 mL of HPTS in the saturated $MnCl_2$ solutions (about 6.0 M) upon addition of different amount of NaOH 10 M, on the left. On the right, the lifetime values processed in a Stern-Volmer plot.

As expected, because of the well-known speciation behavior of Mn(II), addition of NaOH led to the precipitation of manganese hydroxide and, after a first pH jump from 3.6 to 5.3 (for an addition of 0.020 mL of NaOH corresponding to a final concentration of 0.2 M), very small changes in pH could be detected up to the addition of NaOH as a final concentration of 1.7 M. This demonstrates that saturated **Mn(II) solution shows a strong buffering effect on pH**. The fluorescence of HPTS in the Mn(II) solution partially increases upon addition of NaOH 0.2 M (see figure 6.8, right) but it is still very weak. In order to investigate the possible occurrence of a dynamic quenching of HPTS by Mn(II), we measured the excited state lifetime τ of the molecule as a function of the added NaOH. The results are plotted in figure 6.9: **τ is strongly dependent on the pH demonstrating the occurrence of a dynamic quenching**. We would like to stress that this pH dependence of τ in the system is indeed **an indirect dependency**. In fact, **the probe itself has a pH independent lifetime** but its lifetime is **dependent on the Mn(II) concentration**. Addition of NaOH leads to a decrease of the concentration of Mn(II) ions and hence to an increase of τ. According to the Stern-Volmer equation, a linear dependency is expected for $1/\tau$ from the quencher concentration: this was indeed observed in the experiments as shown in figure 6.9 (right).

It is interesting to observe (figure 6.8) that upon addition of NaOH from 1.7 to 3.0 M a small increase of pH is observed from 5.8 to 6.2 but this produces a dramatic enhancement of the fluorescence of HPTS and a relevant increase of τ. **No further changes in fluorescence intensity or τ are observed for further addition of NaOH**.

Considering all these results we can conclude that:

1) the response of the fluorescence of HPTS to pH in Mn(II) saturated solution is complicated by **dynamic quenching with Mn**;
2) despite fluorescence response depends both on pH and Mn(II) concentration, since the concentration of Mn is pH dependent, **we can still use HPTS to detect pH changes in the solution**;
3) HPTS fluorescence is (in saturated Mn(II) solutions) very sensitive to small changes of pH around 6.0, in particular **a dramatic increase of fluorescence is observed when the threshold of pH=6.0 is crossed**.

Hence, finally, **HPTS can be used as a fluorescent probe to map the pH of the Mn(II) solution whether it is either higher or lower than 6.0**.

6.4.2 Formation of micro-tubes in Mn(II) silica gardens

As mentioned, for fluorescence imaging of silica garden we preferred metal ions that formed **un-colored** or weakly colored species (as ions or precipitates) but that, in the meantime, could produce **tubular structures** in the micro-scale suitable for our experimental set-up. Good candidate as non-quenching and non-absorbing species were Ca(II), Ba(II) and Mg(II), but we could not obtain reproducible tubular structures with these metal ions.

After several tests we chose $MnCl_2$ as the best candidate. For the experiments a droplet of saturated metal solution (2 μL) was deposited on the top of a glass coverslip (24x24 mm^2) while the **SS** (50 μL) was dropped on a microscope glass slide (75x25 mm^2). Hence the coverslip

was reversed top-down and placed on the larger glass slide, immerging the smaller MS drop into the larger SS one (the two slides were spaced by a plastic tape 0.1 mm thick). This leads to the formation of a **closed membrane** and the increasing of the internal osmotic pressure leads to local membrane rupture and to the **formation of tubes** that, because of the geometry of the system, could **grow only horizontally**. We followed the growth with time-lapse acquisition using a CCD camera and detecting simultaneously the transmission and fluorescence images or using a confocal laser scanning microscope (CLSM). Here we report and discuss images acquired with this latter setup at the University of Granada.
Some representative images obtained with this set up using a saturated $MnCl_2$ solution as MS are shown in figures 6.10 (left) and 6.11 (left).

The optical transmission images show the growth of tubes that propagate according to almost linear (figure 6.11) or curve trajectories (figure 6.10); the propagation rate is typically about 1 mm/min. We would like to stress that these structures could be obtained in the absence or the presence of HPTS (0.2 mM) demonstrating that the presence of the fluorescence probe has negligible effect on the growth. In figure 6.10 and 6.11 the formation of **individual tubes** is observed.

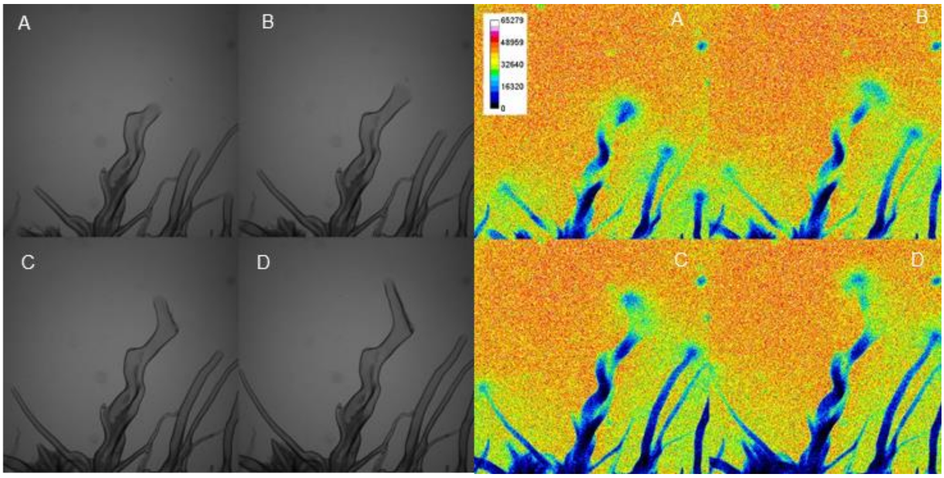

Figure 6.10 Transmission, on the left, and fluorescence (in false colors), on the right, of a growing manganese silica garden at different times (5 seconds delay) in the presence of HPTS 0.2 mM in the SS. Size: 1417x1417 μm^2.

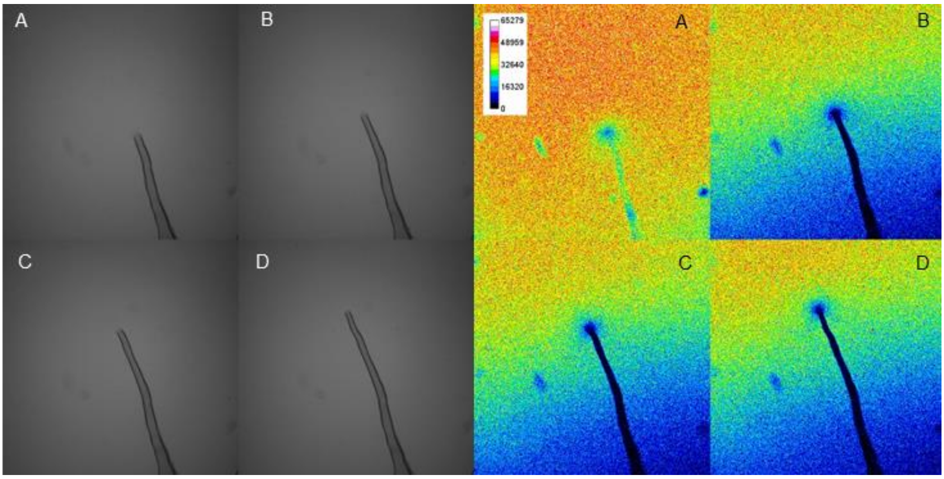

Figure 6.11 Transmission, on the left, and fluorescence (in false colors), on the right, of a growing manganese silica garden at different times (8 seconds delay) in the presence of HPTS 0.2 mM in the SS. Size: 1417x1417 μm^2.

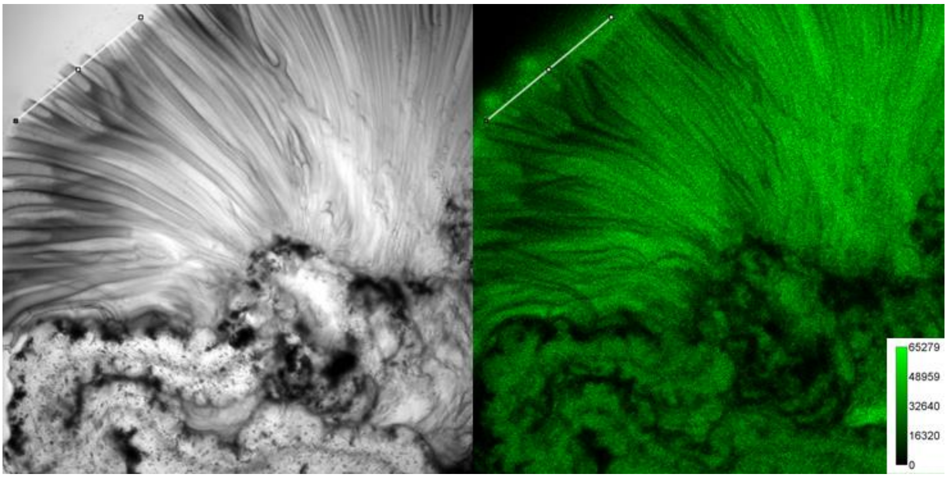

Figure 6.12 Transmission, on the left, and fluorescence, on the right, of a growing manganese silica garden in the presence of HPTS 0.2 mM in the MS. Size: 1417x1417 μm^2.

Nevertheless, in other case or in different parts of the same garden different and more complicate structures could be observed. For example, in figure 6.12 it is possible to observe the growth of a **bundle of tubes** almost parallel to each other. These images are extracted from time-lapse video where further detail can be clearly observed, in particular:

1) the large globular tube on the bottom of figure 6.12 contains a solution with **suspended nano/microparticles (NPs)**. Thanks to the presence of these NPs that behave as optical tracer it is possible to observe (in the video) **that the solution flows inside the tube transporting the NPs**;
2) the **flow** described in point 1 goes in the direction of the growing bundle of tube and it **penetrates the tubes**;
3) the solution contained inside the linear, parallel tubes **is ejected out from the top**;
4) **small particles** (NPs) ejected from the tubes can be clearly spotted on the top of the left image of figure 6.12.

These results demonstrate that:

1) **precipitate is formed inside the tube during their growth**, also in the form of NPs;
2) **a continuous, apparently constant flow of solution** takes place inside the tube;
3) **solution is ejected** outside the tube forming a **JET**.

All **these features are quite general**, and they were observed in several different videos and experiments and they constitute a new piece of information about the dynamic of growth of silica garden. In fact, although some of them were expected according to some proposed model, **they were not observed directly before**.

Even as far as the jet is concerned, its formation was partially justified by buoyancy effect that in our system is completely negligible.

Additional information is given by fluorescence imaging. In particular, being silica garden compartmentalized systems, it is possible distribute selectively the pH probe (HPTS) either in the MS or SS or in both. This has the advantage to **track the two different solutions** and also to visualize their possible mixing.

In figure 6.12 is it possible to compare the transmission and fluorescence images of a Mn(II) silica garden exactly at the same time. In this experiment the fluorescent probe **HPTS had been solubilized in the MS**, hence no fluorescence signal is expected to arise from the SS. The white line tracked in the transmission image of figure 6.12 allows us to localize the position of the ends of the tube at the specific time of the observation; the same line was tracked on the fluorescence image to compare the position of the fluorescence (in green) and of the tubes. By comparing the two images we can clearly conclude that **part of the SS just outside the tube became strongly fluorescent**. This demonstrates that:

1) the MS containing **HPTS is ejected out** of the tubes;
2) in the jet **mixing of the MS and SS occurs** and the **pH in the jet is higher than in the MS** (more in detail pH >6.0).

This latter conclusion was quite unexpected since conventional model for silica garden growth propose an actual separation of the MS and SS because of the **continuous formation of a membrane** at the MS/SS interface.

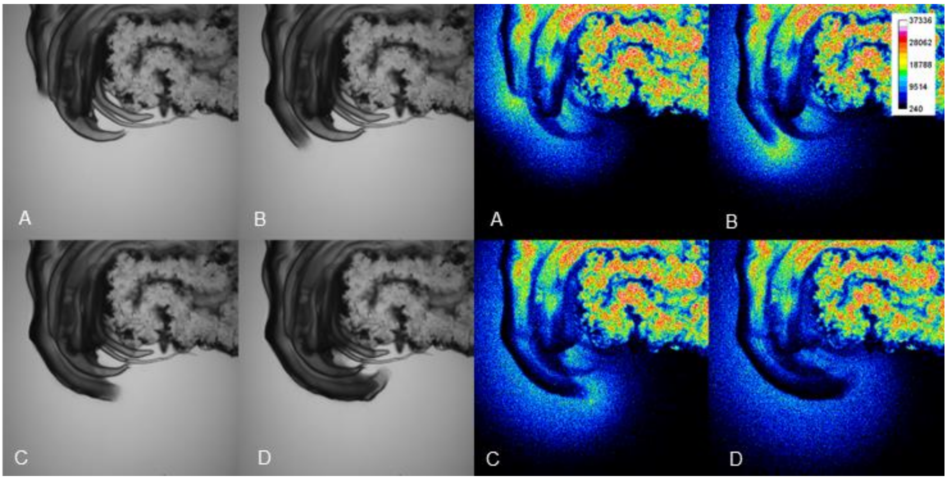

Figure 6.13 Transmission (left), and fluorescence in false colors (right), of a growing manganese silica garden at different times (75 s time interval) with HPTS 0.2 mM in the MS. Images collected by LCFM. Size: 1417x1417 μm^2.

The ejection of the HPTS from the tube is even more evident in the images shown in figure 6.13. On the left the formation of a curved tube can be observed. Fluorescence images in false colors (right) clearly show the presence of bright fluorescence in the SS just outside the tube end. Moreover, this **fluorescent area moves with the tube** and it is **located in the jet**. Interestingly, **when the tube stops growing also fluorescence disappears**, indicating that solution ejection has stopped. The presence of HPTS in the SS can be finally observed as **a fluorescent aura around the tube**.

It is also very interesting noticing that the **final section of the tube is not fluorescent**. This is due to the combination of **acidic pH and high concentration of Mn** in this region. On the contrary, looking at the same tube at a longer distance (about 0.5 mm) from the tip, fluorescence is quite strong in the inner solution. This very interesting behavior can be explained with the **diffusion of OH^- ions through the tube membrane** that was demonstrated and investigated in detail in the previous section for Fe(III) silica garden. **Diffusion through the membrane is not immediate** and some **minutes are needed** after the membrane formation before the **concentration of hydroxide in the tube becomes high enough to cause Mn precipitation and pH increase**. For this reason, switch on of the fluorescence (inside the tubes) is some minutes delayed with respect to the formation of the tubes themselves.

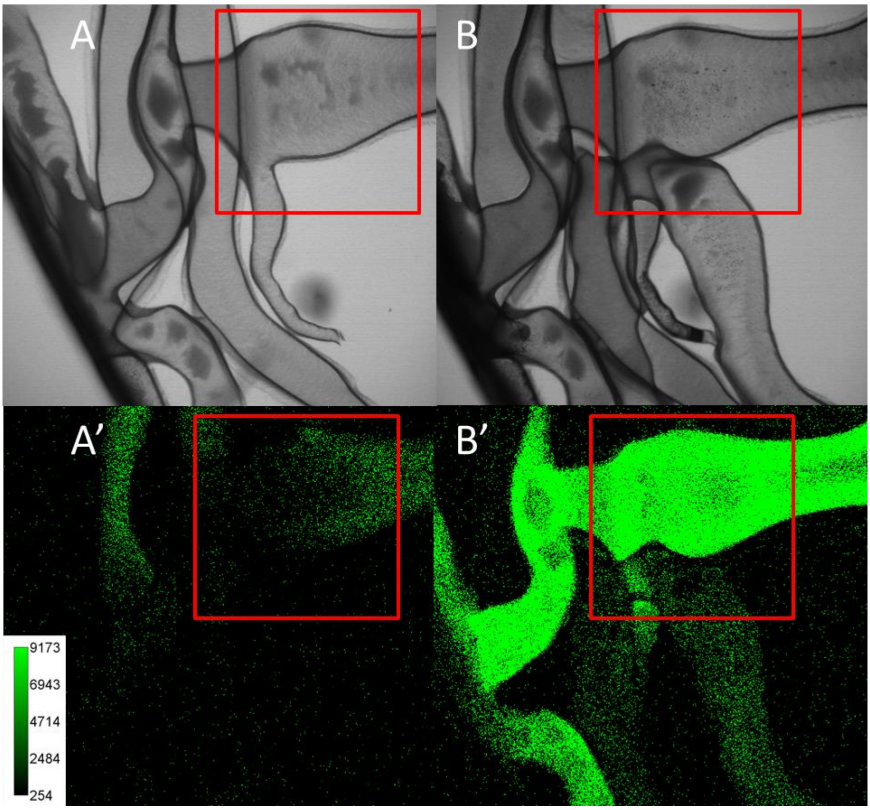

Figure 6.14 Transmission (top) and fluorescence (bottom) images of a Mn(II) silica garden immediately after formation (left, A and A') and 10 minutes later (right, B and B' in the presence of HPTS 0.2 mM in the MS. Images collected by LCFM. Size: 1417x1417 μm^2.

This delayed switch on of the fluorescence due to OH$^-$ diffusion through the membrane can be clearly observed in figure 6.14. where the transmission and the fluorescence of a just formed Mn(II) silica garden is shown. The tube in the red square (A) shows in fluorescence mode (A') a very weak fluorescence demonstrating that the pH in the inner solution is quite acidic and the Mn(II) concentration very high, hence **fluorescence of HPTS is quenched**. After about 10 minutes the formation of **precipitate in form of particles** can be observed inside the tube (image B) while the **fluorescence is dramatically switched on** (figure B'). This confirms that diffusion of OH$^-$ through the membrane causes precipitation of Mn and an increase of the pH.

As mentioned, we also performed fluorescence imaging experiments of silica gardens were the pH probe **HPTS was solubilized in the SS**. The acquired fluorescence images are shown in figure 6.10 and 6.11. The results clearly confirm the conclusions discussed above. In this case the **SS is brightly fluorescent** because of the presence of HPTS in a strongly alkaline environment (the probe is ON). On the other hand, **around the tip** of the growing tubes **a dark region of the SS is detected**. This region **moves with the tube** and clearly correspond to the **jet of metal solution ejected from the tube**. In this case the fluorescence in the jet is much weaker than in the SS but is **more intense than inside the tube**. This result further confirms the conclusion that the two solutions **MS and SS get mixed in the jet**.

6.5 Conclusions

In this section it was described how we performed two different kinds of investigations that gave complementary information about the mechanism of formation and evolution of silica gardens: 1) one on the diffusion through the membrane and 2) another one on the mechanism of growth of micro-tubes in quasi 2D silica garden with fluorescent probes.

About the first point, we decided to use $FeCl_3$ for the investigation of membrane permeation. We noticed the formation of a brown membrane in the region of contact of the metal salt and the sodium silicate solutions, due to the precipitation of iron insoluble hydroxides, such as $Fe(OH)_3$, inside the metal salt solution, led by the diffusion of OH^- ions from the silicate solution through the membrane. After that, the propagation of the darker region occurs inside the iron solution over time. However, after a while, the precipitate formed starts to re-dissolve. This result observed was quite surprisingly, and it could be explained in two ways:1) diffusion of OH^- leads to the formation of soluble iron hydroxides, like $Fe(OH)_4^-$; 2) diffusion of OH^- is stopped and re-dissolution occurs due to the diffusion of the still acidic Fe^{3+} solution (not yet reached by OH^-). Considered that re-dissolution starts form the iron solution side rather than from the membrane, we concluded that indeed the OH^- diffusion through the membrane is strongly slowed down after a while.

Moreover, over time thickening of the membrane is observed, and the formation of several layers on the membrane too. Silica in the solution is solubilized as silicate but SiO_2 precipitates upon acidification of the solution. Hence, we concluded that the thickening of the membrane is due to two main factors: 1) diffusion of OH^- from SS to MS through the membrane causes a local decrease of pH close to the external (SS exposed) side of the membrane; 2) Fe(III) diffuses through the membrane and precipitates as silicate on the external SS exposed side.

We were able also to estimate the diffusion coefficients of the diffusing species using the Fick's law in the case of 1D diffusion into a homogenous medium, and the diffusion coefficient D of OH^- ions derived from the fittings were found to be 50 times lower than the one reported in literature. This means that the process is controlled not just by the diffusion but also by the precipitation of the hydroxides.

In order to explore the second investigation, we needed to properly select the pH probe and the metal ion. To avoid problems in fluorescence detection connected to the optical filtering effect of intensely colored metal ions we focused on Mn(II) which gives pale pink saturated solution. Moreover, we saw that Mn(II) forms very reproducible tubular silica gardens in the experimental conditions necessary for optical imaging.
After testing several pH probes, we found out that HPTS does not bind to Mn(II), so we adopted this probe for our experiments, avoiding static quenching.
However, experiments showed that HPTS fluorescence is extremely weak in saturated $MnCl_2$ solutions. Nevertheless, this weak fluorescence is due at least in part to the strong acidic pH of the solution, but also to dynamic quenching. We hence wondered if we could discriminate the effect of the pH and the Mn(II) concentration on the fluorescence of HPTS, and we tested it adding different amount of NaOH to increase the pH and measure the fluorescence response. We found out that: 1)

saturated Mn(II) solution shows a strong buffering effect on pH, and 2) τ is strongly dependent on the pH demonstrating the occurrence of a dynamic quenching. This pH dependence of τ in the system is however an indirect dependency. In fact, the probe itself has a pH independent lifetime but its lifetime is dependent on the Mn(II) concentration. Hence, we concluded that HPTS was able to be used to detect pH changes in our experiments.
It was also observed that no further changes in fluorescence intensity or τ are observed for addition of NaOH more than 3.0 M as final concentration.

Considering all these results we can conclude that: 1) the response of the fluorescence of HPTS to pH in Mn(II) saturated solution is complicated by dynamic quenching with Mn; 2) despite fluorescence response depends both on pH and Mn(II) concentration, since the concentration of Mn is pH dependent, we can still use HPTS to detect pH changes in the solution; 3) HPTS fluorescence is (in saturated Mn(II) solutions) very sensitive to small changes of pH around 6.0, in particular a dramatic increase of fluorescence is observed when the threshold of pH=6.0 is crossed. Hence, finally, HPTS can be used as a fluorescent probe to map the pH of the Mn(II) solution whether it is either higher or lower than 6.0.

We also investigated the formation of micro-tubes in Mn(II) silica gardens, both in transmission and fluorescence mode, and what we concluded was that: 1) there is the presence of suspended nano/microparticles (NPs) inside the solution and that the solution flows inside the tube transporting the NPs; 2) the continuous, apparently constant flow described in point 1 goes in the direction of the growing bundle of tube and it penetrates the tubes; 3) the solution contained inside the linear, parallel tubes is ejected out from the top forming a jet; 4) small particles (NPs) are ejected from the tubes.

Considering experiments at confocal microscope, where the fluorescent dye was put inside the MS, we observed that part of the SS just outside the tube became strongly fluorescent, that demonstrates that: 1) the MS containing HPTS is ejected out of the tubes; 2) in the jet mixing of the MS and SS occurs and the pH in the jet is higher than in the MS. This latter conclusion was quite unexpected since conventional model for silica garden growth propose an actual separation of the MS and SS because of the continuous formation of a membrane at the MS/SS interface. Moreover, we could affirm that fluorescent area moves with the tube and it is located in the jet, and when the tube stops growing also fluorescence disappears, indicating that solution ejection has stopped.

The presence of HPTS in the SS can be considered as a fluorescent aura around the tube. It was also seen that the final section of the tube is not fluorescent due to the combination of acidic pH and high concentration of Mn in this region. This very interesting behavior can be explained with the diffusion of OH^- ions through the tube membrane, that is not immediate and hence some minutes are needed after the membrane formation before the concentration of hydroxide in the tube becomes high enough to cause Mn precipitation and pH increase.

The results observed inserting HPTS inside the SS confirmed the conclusion reached previously: the two solutions MS and SS get mixed in the jet.

6 References

[1] L. M. Barge, S. S. S. Cardoso, J. H. E. Cartwright, G. J. T. Cooper, L. Cronin, A. De Wit, I. J. Doloboff, B. Escribano, R. E. Goldstein, F. Haudin, D. E. H. Jones, A. L. Mackay, J. Maselko, J. J. Pagano, J. Pantaleone, M. J. Russell, C. I. Sainz-Díaz, O. Steinbock, D. A. Stone, Y. Tanimoto, N. L. Thomas, *Chem Rev* **2015**, *115*, 8652-8703.

[2] J. Kragten, *Atlas of metal-ligand equilibria in aqueus solution*, **1977**.

[3] R. Reddy, R. Banerjee, *Procedia IUTAM* **2015**, *15*, 305-312.

[4] W. L. Noorduin, A. Grinthal, L. Mahadevan, J. Aizenberg, *Science* **2013**, *340*, 832-837.

[5] C. Ritchie, G. J. T. Cooper, Y. F. Song, C. Streb, H. B. Yin, A. D. C. Parenty, D. A. MacLaren, L. Cronin, *Nat Chem* **2009**, *1*, 47-52.

7 Acknowledgements

I thank Professor Marco Montalti, my tutor of this Ph.D. project, and all the members of Photochemistry and Nanoscale Laboratory of the Dipartmento di Chimica “G. Ciamician” of the Università di Bologna.

I thank Professor Juan Manuel García-Ruiz and his “Prometheus” ERC project which I have been a member, and his whole staff of the Laboratorio de Estudios Cristatlograficos (LEC) at the Instituto Andaluz de Ciencias de la Tierra (IACT) member of the Consejo Superior de Investigaciones Cientificas (CSIC) of the Universidad de Granada.

I thank Professors Ángel Orte Gutiérrez and Emilio García Fernández and all the members of the Departamento de Fisicoquìmica of the Faculdad de Farmacia of the Universidad de Granada.

I thank Dr. Raquel Marrero Díaz and the Centro Pfizer of the Junta de Andalucía de Genómica e Investigación Oncológica (GENYO) of the Universidad de Granada.